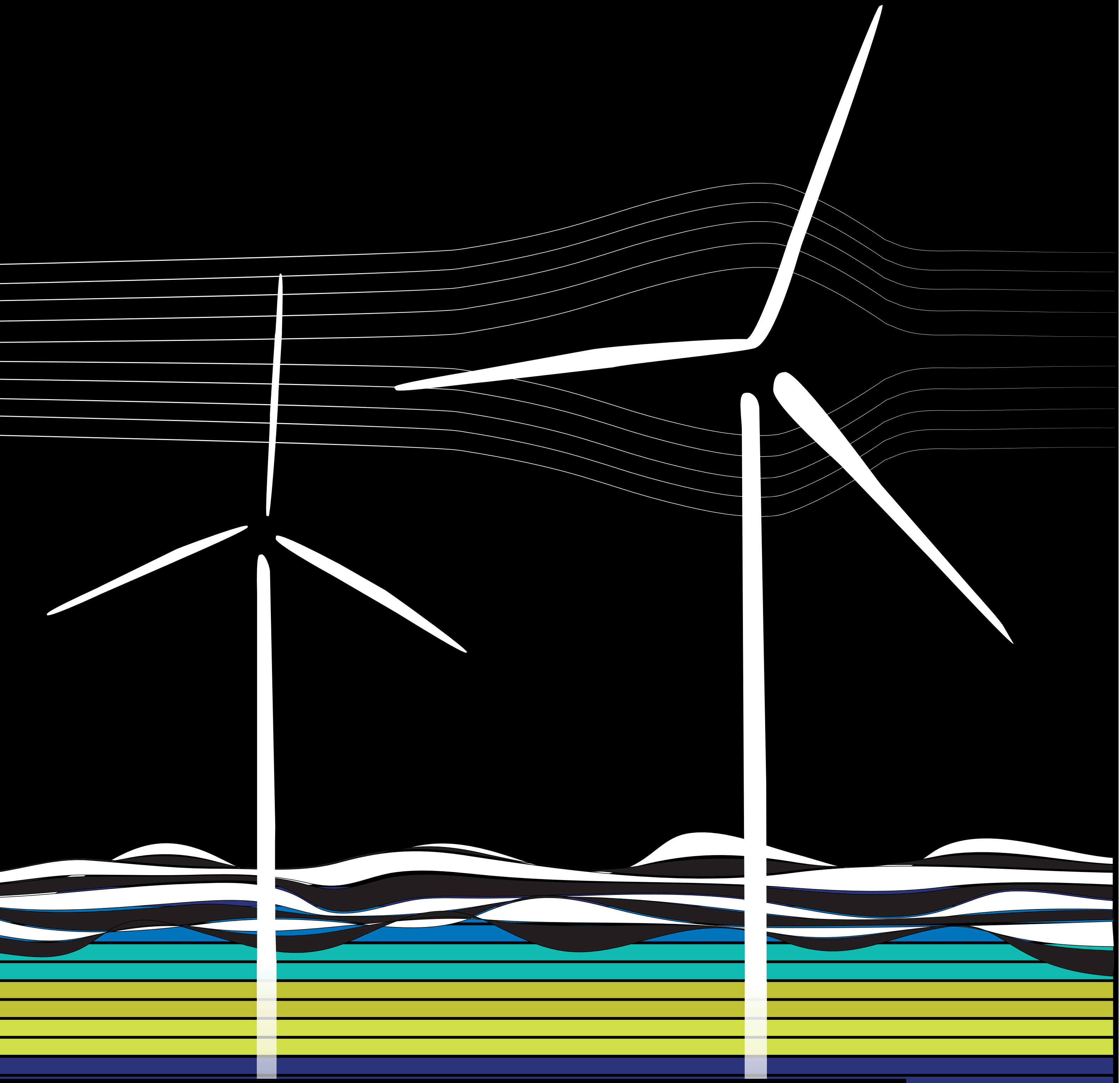

Response of an Offshore Wind Turbine supported by a Non-Local Winkler Foundation

An Efficient 1D Time-Domain Model accounting for the 3D Frequency-Dependent Dynamic Soil Stiffness

Youri Hasper

RESPONSE OF AN OFFSHORE WIND TURBINE SUPPORTED BY A NON-LOCAL WINKLER FOUNDATION

AN EFFICIENT 1D TIME-DOMAIN MODEL ACCOUNTING FOR THE 3D FREQUENCY-DEPENDENT DYNAMIC SOIL STIFFNESS

by

Youri Hasper

in partial fulfillment of the requirements for the degree of

Master of Science
in Offshore & Dredging Engineering

at the Delft University of Technology,
to be defended publicly on Thursday January 31, 2019 at 11:00 AM.

Thesis committee:	Prof. dr. A. Metrikine,	TU Delft, chairman
	Dr. Ir. K. N. van Dalen,	TU Delft, daily supervisor
	Ir. F. Besseling,	Witteveen+Bos, daily supervisor
	Ir. J. S. Hoving,	TU Delft, committee member supervisor
	Dr. W. G. Versteijlen,	Siemens, committee member

This thesis is confidential and cannot be made public until Januari 31, 2021.

An electronic version of this thesis is available at `http://repository.tudelft.nl/`.

Delft
University of
Technology

SUMMARY

Response of an Offshore Wind Turbine supported by a Non-Local Winkler Foundation:
An Efficient 1D Time-Domain Model accounting for the 3D Frequency-Dependent Dynamic Soil Stiffness.

With increasing evidence of human-induced accelerated climate change, the need of sustainable, non-polluting, energy sources becomes evident. Offshore wind generated electricity is currently one of the most promising sources of energy to create a sustainable global energy mix. The offshore wind industry has developed rapidly over the last years. The cumulative installed capacity shows an exponential growth. Monopiles remain the most popular substructure type of all installed substructures in Europe. This thesis focuses on calculation methods to evaluate the response of that foundation type.

The interaction between a monopile and soil is called soil-structure interaction (SSI). In the offshore wind industry, SSI is commonly modelled as a 1D local Winkler foundation with local nonlinear elastic springs to represent the lateral soil stiffness. The stiffness is often based on semi-empirical relations between the lateral displacement of the pile and the soil pressure (p-y method). This approach neglects the interaction effects between different soil layers and there are uncertainties regarding the validity of applying this method to large diameter, rigidly behaving, monopiles.

In this thesis, a 3D linear-elastic (LE) finite element (FE) model is used to compute 1D global (non-local) complex-valued dynamic soil stiffness, which captures the coupled 3D reactions of soil to the pile. The frequency dependence of local and non-local linear-elastic lateral, rotational and coupling dynamic soil stiffness is analyzed for heterogeneous soil stratigraphy. The effect of different boundary conditions in the 3D model formulation to the frequency dependence of dynamic soil stiffness is analysed.

The complex-valued-frequency dependent dynamic soil stiffness kernels are approximated by frequency independent coefficient matrices for added mass, damping and stiffness. The performance of the coefficient matrices in terms of representing the complex-valued dynamic soil stiffness is analysed with cost functions. It was found that the dynamic soil stiffness can be approximated by frequency independent added mass, stiffness and damping coefficient matrices in the frequency range of interest for offshore wind.

A 1D Timoshenko beam model is developed in the frequency-domain and is discretized in space by Euler's central finite difference method. The added mass, stiffness and damping matrices, which represent the non-local Winkler foundation, are incorporated in the equations of motion. The complex-valued SSI response of the 1D model to the dynamic loading is compared with the response of the 3D LE FE model in the frequency domain.

As a last step, a superstructure and turbine are integrated with the monopile SSI model and the total integrated model is transferred to the time domain. Time domain computations are performed for free vibrations, harmonic loading and realistic aero-/hydrodynamic loading scenarios. The transformation into the time domain is important since it allows the user to incorporated nonlinear wave and wind loading and air-turbine interaction effects that are considered to have a major impact on the resulting dynamic system response. The developed time-domain model is computationally very efficient in predicting the time-domain SSI response of an offshore wind turbine for varying loading scenarios. The model can be used for initial design purposes for offshore wind turbines.

PREFACE

I would like to express my appreciation to Professor Metrikine for his guidance along the way of this thesis. I would like to thank my daily supervisors Karel van Dalen and Floris Besseling. Karel van Dalen I would like to thank for his patience, his help in making challenging dynamic phenomenons understandable and for the many interesting conversations during this thesis. I would like to thank Floris Besseling for his support and for his ability to motivate me to strive for understanding, rather than showing me the easiest way. His passion for dynamics was inspiring and reflected in many critical questions during the thesis. I believe his support has has risen this thesis to a higher level. Furthermore, I would like to thank Pim Versteijlen and João de Oliveira Barbosa for developing, and for allowing me to make use of, the non-local method and 3D model that are used in this thesis. All you guys have been both motivational and helpful in times of adversity and in discussing how to outline the thesis.

Equally important, I would like to thank my friends, my family and especially my girlfriend Charley Meyer for your everlasting support during the course of my studies at the TU Delft and especially during the last year. It was not always easy, but you got me through the most challenging year of my life. Thank you.

Youri Hasper
Delft, January 2019

CONTENTS

Summary **iii**

Nomenclature **ix**

List of Figures **xi**

List of Tables **xv**

1 Introduction **1**
- 1.1 General introduction offshore wind 1
  - 1.1.1 Soil-Structure Interaction 2
- 1.2 Research description 3
- 1.3 Research objective and challenges 3
- 1.4 Approach 3

2 Structure-Soil Interaction modelling **5**
- 2.1 Introduction 5
- 2.2 Conventional models and limitations 5
- 2.3 State-of-art SSI modelling 8
  - 2.3.1 3D continuum modelling 8
  - 2.3.2 Hybrid methods 8

3 Matlab based 3D FE model **9**
- 3.1 Introduction 3D model 9
- 3.2 Model set-up 9
  - 3.2.1 Calculation of the response of a pile embedded in soil 9
  - 3.2.2 Calculation of the complex-valued dynamic stiffness 10
- 3.3 Soil continuum 11
  - 3.3.1 Dimensions, mesh size and boundary conditions of soil medium 11
  - 3.3.2 Viscous damping. 13
  - 3.3.3 Stratigraphy 14
- 3.4 SSI response 14

4 Dynamic soil stiffness **17**
- 4.1 Matrices and non-locality 17
- 4.2 Frequency-independent mass, damping and stiffness framework. 19
- 4.3 Frequency dependency of dynamic soil stiffness 19
  - 4.3.1 Model results 20
  - 4.3.2 Resonance effects associated with 3D model setup 24
  - 4.3.3 frequency dependence of non-local imaginary parts of the lateral dynamic soil stiffness . 25
  - 4.3.4 Conclusions and discussion 27
- 4.4 Foundation impedance 27
- 4.5 Evaluation of results and comparison with 3D model results 28
  - 4.5.1 Evaluation importance added mass 33

5 1D approximation of pile-soil system **37**
- 5.1 Introduction and reason for 1D 37
- 5.2 Model description 1D Monopile model 37
  - 5.2.1 Space discretization 38
  - 5.2.2 Boundary Conditions 39
- 5.3 Frequency domain pile-soil 41
  - 5.3.1 Concluding remarks 45

5.4 Time domain pile-soil. 47
5.4.1 Free vibrations pile-soil 48

6 1D approximation of superstructure - pile - soil system 51
6.1 Superstructure/turbine modelling 51
6.2 Dynamic loading on OWT. 53
6.2.1 Types of loads 53
6.2.2 Hydrodynamic loading. 53
6.2.3 Aerodynamic loading 56
6.3 Freq domain total OWT 58
6.4 Time domain total OWT 59
6.4.1 Free vibrations OWT 59
6.4.2 Harmonically forced vibrations – OWT. 61
6.4.3 Forced vibrations – OWT 63

7 Conclusions & Recommendations 67
7.1 Conclusions. 67
7.2 Limitations 68
7.3 Recommendations 69

A Soil stratigraphy 71

B Fit between 3D stiffness and approximated coefficients 73
B.1 Fit between elements 73

C Misfit 3D–1D SSI response 77
C.1 General equations 77
C.2 Cases 77
C.3 Results – Tables 78
C.4 Results – Figures 78

D Matrices 85
D.1 Matrices soil-pile system 85

E Code thrust coefficient calculation 87

Bibliography 89

NOMENCLATURE

$\mathbf{0}_n$	Zero matrix of n by n
A	Cross sectional area of the pile
A	Static or cyclic loading factor (section ...)
β	Pitch angle of the blades
C	Damping matrix
C_s	Shear wave velocity
C_p	Pressure wave velocity
$C_{u,\phi}^{total}$	Misfit of the sum of the real and imaginary displacements and rotations
$C_{u,\phi}^{real}$	Misfit of the sum real-valued displacements and rotations
$C_{u,\phi}^{imag}$	Misfit of the sum of the complex-valued displacements and rotations
C_D	Hydrodynamic drag coefficient
C_M	Hydrodynamic inertia coefficient
C_p	Power coefficient
C_t	Thrust coefficient
D_0	Pile diameter
d	Water depth
δ	Logarithmic decrement
Δf	Half-power bandwidth
E_p	Young's modulus of steel
E_s	Young's modulus of soil
η	Material damping ratio
F	Horizontal force
F_0	Amplitude of the force
f	Frequency
f_n	Fundamental natural frequency
f_n^h	Soil layer resonance (or equivalently, cut-off) frequency
G	Shear modulus
G^*	Complex-valued shear modulus
g	Gravitational constant
H	Soil layer thickness
h	Discretization length
I	Second moment of area of the pile cross section
$\mathbf{I}_n$	Identity matrix of n by n
$i\&j$	Discretization points
K	Stiffness matrix
$K_{dyn}^{ii,jj}$	Complex-valued dynamic stiffness matrix, $ii = u,\phi$ & $jj = u,\phi$
k	Wavenumber
KC	Keulegan Carpenter number
κ	Timoshenko shearing coefficient
L_a	Pile length in air
L_s	Pile embedded length
L_w	Submerged pile length
L/D	Length over diameter ratio
λ	Wave length
M	Mass matrix
m	Overturning moment
$m(z,u,\phi)$	Distributed overturning moment
n	Number of nodes used for discretization
ν	Poisson's ratio
ω	Angular frequency
p	Lateral soil pressure on beam ($p-y$ method)
$\phi(z,t)$	Lateral pile rotation (depth and time dependent)
ψ	Angle of internal friction
ψ	Phase angle (refch:explanation wakes)
Q	Amplification factor
$q(z,u,\phi)$	Distributed load
R	Radius of the pile
ρ_a	Mass density of air
ρ	Mass density of the pile
ρ_s	Mass density of the soil
ρ_w	Mass density of water
T	Aerodynamic thrust
t	Time
T_0	mean wave period
$u(z,t)$	Lateral pile displacement (depth and time dependent)
$u_c(z)$	current velocity (depth dependent)
u_m	Maximum water flow velocity
u_{wind}	Wind velocity
y	Lateral displacement ($p-y$ method)
x	Horizontal axis
ξ	Damping ratio
z	Vertical axis (depth)
ζ_a	Wave amplitude

LIST OF FIGURES

1.1 WindEurope (2018) - cumulative and annual offshore wind installations (MW) [1] 1
1.2 Estimate of capital cost breakdown for an offshore wind farm [2] 2

2.1 $p - y$ curve method 6
2.2 Rigid versus flexible pile response when subjected to lateral loading. A static force of 1N and moment of 45 Nm are applied to the pile head. The rigid pile has an L/D of 2 and the flexible pile has an L/D of 20. To compare the shapes, the rigid displacements and rotations are respectively multiplied by a factor 60 and 80. 7

3.1 Visual representation of 3D model for calculation of SSI response. Explanation about the two cases is given in section 3.3.1 10
3.2 Visual representation of 3D model for calculation of dynamic stiffness. The Explanation about the two cases is given in section 3.3.1 11
3.3 Varying Young's Modulus 13
3.4 Different soil configurations 14
3.5 Normalized real and imaginary lateral displacement and rotation for the three different soil stratigraphies. The force and moment are respectively 1 N and 45 N/m and are applied to the top of the soil-pile system. The excitation frequencies increase from 0 Hz (blue) to 7.5 Hz (red) for BC HS1. Re(u(f)) and Re(ϕ(f)) are normalized by the absolute static Re(u(f=0)) and Re(ϕ(f=0.5)). Im(u(f)) and Im(ϕ(f)) are normalized by absolute Re(u(f=0)) and Re(ϕ(f=0.5)). 15
3.6 Pile head displacement as a function of excitation frequency. An dynamic force of 1N and moment of 45Nm is applied to the three SSI cases. 15

4.1 Real and imaginary dynamic lateral and rotational dynamic stiffness matrices are plotted on a linear and logarithmic scale. The matrices are derived for an excitation frequency of 0.3 Hz. BC HS1 and heterogeneous soil S1 are applied. 18
4.2 Real and imaginary dynamic coupling stiffness matrices are plotted on a linear and logarithmic scale. The matrices are derived for an xcitation frequency of 0.3 Hz. BC HS1 and heterogeneous soil S1 are applied. 18
4.3 Normalized absolute magnitude of row i of local an non-local (off-diagonals) of real dynamic stiffness matrices. Note that $K_{LL} = K_{dyn}^{u,u}$, $K_{RR} = K_{dyn}^{\phi,\phi}$ and $K_{LR} = K_{dyn}^{u,\phi}$ 19
4.4 Ideal frequency dependency of real and imaginary pars of dynamic stiffness 20
4.5 Typical wind and wave spectra, rotational speed (1P) and blade passing (3P) frequency bands for six commercial turbines and measured natural frequencies of OWTs [3]. 20
4.6 Frequency dependence of dynamic soil stiffness for BC HS1 and soil S1. The magnitudes of nodes on the diagonals are plotted against excitation frequency. Figure 4.6a presents the real and imaginary dynamic stiffness matrices. Figure 4.6b presents the normalized real parts of K_{dyn} in the top figures and the real parts of the dynamic stiffness subtracted with the static stiffness at f=0 Hz in the bottom graphs. 22
4.7 Frequency dependence of dynamic soil stiffness for BC HS2, with bedrock at 100m depth, and soil S1. The magnitudes of nodes on the diagonals are plotted against excitation frequency. Figure 4.7a presents the real and imaginary dynamic stiffness matrices. Figure 4.7b presents the normalized real parts of K_{dyn} in the top figures and the real parts of the dynamic stiffness subtracted with the static stiffness at f=0 Hz in the bottom graphs. 23
4.8 Total real part of dynamic stiffness of lowest diagonal node ($K_{41,41}^{u,u}$) for BCs HS1 and HS2 with bedrocks at different depths, 24
4.9 Dynamic stiffness of diagonal $K_{dyn}^{u,u}$ at bottom of cavity for a soil depth of 200m and different material damping ratio's (0% and 2%) 25

4.10 Envelopment of imaginary lateral dynamic stiffness matrices against increasing excitation frequencies. BC HS1 is presented in 4.10a and BC HS2, bedrock at 200m, in figure 4.10b. Note that the label on the x-/ and y-axis should be node [-]. 26
4.11 A single coluimn of the imaginary-valued lateral dynamic stiffness matrix for increasing frequencies. Soil stratigraphy S1 is applied. Figure a) and b) show this respectively for BC HS1 and BC HS2 (200m). 26
4.12 Phase angle between the real and imaginary lateral displacement matrices 27
4.13 For BC HS1, the fits between diagonals of frequency-dependent parts of the dynamic stiffness matrices and approximations with polynomial coefficients. The black lines represent the real dynamic stiffness and the red dotted lines represent the approximated dynamic stiffness using approximated coefficients. 29
4.14 For BC HS2: bedrock at 50m. Fits between diagonals of the frequency-dependent parts of the dynamic stiffness matrices and approximations with polynomial coefficients. The black lines represent the real dynamic stiffness and the red dotted lines represent the approximated dynamic stiffness using approximated coefficients. 29
4.15 BC HS1. Visual representation of misfits for mass and damping matrices. The left column shows the summed magnitude over frequency for the elements in the dynamic stiffness matrices. The middle column presents the contribution of local misfit to the total misfit (eq: (4.10)–(4.11)). In the last column the local ratio is presented as calculated by eq. (4.10)–(4.11) 32
4.16 BC HS2, bedrock at 50m. Visual representation of misfits for mass and damping matrices. The left column shows the summed magnitude over frequency for the elements in the dynamic stiffness matrices. The middle column presents the contribution of local misfit to the total misfit (eq: (4.10)–(4.11)). In the last column the local ratio is presented as calculated by eq. (4.10)–(4.11) 33
4.17 Frequencies for which the forces associated with the diagonals of the mass becomes larger than 10% of the static stiffness. $f_{sig}^{u,u}$, $f_{sig}^{u,\phi}$ and $f_{sig}^{\phi,\phi}$ present the frequencies for which respectively $M^{u,u}$, $M^{u,\phi}$ and $M^{\phi,\phi}$ become significant. $f = \omega/(2\pi)$. 34
4.18 Diagonals of the lateral added mass, stiffness and damping coefficient matrices. 34
4.19 Frequencies for which the forces associated of the elements in the added mass matrices become significant. The results for BC HS1 and BC HS2 (bedrock at 50m) are shown in subfigures a) and b) 35

5.1 Discretized monopile as a beam with n elements 39
5.2 Dynamic frequency response of pile-soil system for the frequencies of 0.3 and 0.9 Hz. R1, R2, R3 and R4 are shown as $1D_{1th}$, $1D_{2nd}$, $1D_{3th}$ and $1D_{direct}$, respectively 42
5.3 subfigures (a) – (b) show the misfits of R1–R4 for respectively HS1, HS2$_{50m}$, HS2$_{100m}$ and HS2$_{200m}$. The black line represents the 5% error limit 45
5.4 Comparison case R2 and R1 for boundary conditions HS1 and HS2 (50, 100 & 200m). 45
5.5 (a) The top figure presents the displacement of pile head for case HS1, no bedrock. The corresponding frequency magnitude spectrum is shown in the bottom figure. The blue line shows the displacement of the monopile head when soil mass is included. The orange line shows the displacement when soil mass is excluded. Figure (b) presents the half-power bandwidth method for pile head response with soil mass. 49
5.6 Damped free motion starting from rest at an initial displacement x_0 49
5.7 Damping ratio of monopile embedded in soil for case HS1 according to the method of logarithmic decrement 50

6.1 Schematic representation of the complete offshore wind turbine model that is subjected to dynamic loading. 52
6.2 Assembled OWT mass, damping and stiffness matrices. The green colour indicates elements with value zero. Positive values are indicated in blue and negative values in yellow. The diagonals in figure a) and c) are positive sign definite. 52
6.3 full offshore wind turbine head displacement over frequency. The resonance frequency is 0.273 Hz. 53
6.4 Modified Pierson-Moskowitz wave spectrum for $H_s = 2$m and $T_0 = 9$s 53
6.5 particle orbits according to the Airy Wave Theory [4]. 54
6.6 Regions of applicability of wave theories [5]. 55

6.7 Time series of mean wind speed at hub height and corresponding single-sided amplitude spectrum 57
6.8 Relation between the power coefficient ($C_p[-]$) and thrust coefficient ($C_t[-]$) as a function of the tip speed ratio (λ). 57
6.9 Aerodynamic power and thrust as a function of time 58
6.10 Frequency response results for OWT structure when subjected to 530 kN loading at the top of the tower at the frequencies 0, 0.1, 0.2, 0.3 and 0.4 Hz. 58
6.11 Initial displacement (left figure) and rotation (right figure) profile for the OWT at a static excitation of of 530 [kN] applied at the top of the OWT. 59
6.12 Free vibrations for full OWT structure for case R1 and R2. The pile head displacement over time is shown in the three figures, from which the most right figure shows a single peak in high detail. The initial displacement and rotation profile is shown in figure 6.11 and the velocities are set to zero. The initial conditions are applied to R1 and R2. 59
6.13 Single sided amplitude spectrum. 60
6.14 Damping ratio's as derived using the method of logarithmic decrement for case R1 and R2 . . . 60
6.15 Effect of material damping ratio, soil stiffness and natural frequency to OWT damping ratio related to the soil. The stiffness and damping matrix are calculated for BC HS1. 61
6.16 OWT head response for a realistic step load ($F(t) = F_0$ for: $t > 0$) in the top left hand side figure and harmonic loads of $F(t) = F_0 \sin(\omega t)$ in the other figures. $F_0 = 526.8[kN]$. The excitation frequencies are indicated above each figure. The mass starts at the equilibrium ($u(0) = 0$ and $\dot{u}(0) = 0$). The time series is 150 seconds. The structure starts at rest in $t = 0$ (i.e. initial conditions are set to zero). 62
6.17 Comparison OWT head displacement and SDOF approximation for realistic step load ($F(t) = F_0$ for: $t > 0$) and harmonic loads of $F(t) = F_0 \sin(\omega t)$. The excitation frequency is indicated above each figure. The mass starts at the equilibrium ($u(0) = 0$ and $\dot{u}(0) = 0$). The time series is 150 seconds. 63
6.18 Time-domain results for OWT when subjected to different loading scenarios over a time series of 300 seconds. From (a) to (d) the left figures show the OWT head displacement over time for C1, C2, C3 and C4, respectively. The right hand size figures show the corresponding single sided amplitude spectra. The spectrum is derived translating the OWT head response to the frequency domain by means of Fast Fourier Transform (FFT). The spectra are normalized with the sampling number. The natural frequency of the OWT is indicated with the vertical black line at 0.27 Hz 65

B.1 For case HS1 and diameter of 3 meter. Visual representation of misfits for mass and damping matrices. The left column shows the summed magnitude over frequency for the elements in the dynamic stiffness matrices. The middle column presents the contribution of local misfit to the total misfit (eq: (4.10)–(4.11)). In the last column the local ratio is presented as calculated by eq. (4.10)–(4.11) 74
B.2 For case HS1 and diameter of 7 meter. Visual representation of misfits for mass and damping matrices. The left column shows the summed magnitude over frequency for the elements in the dynamic stiffness matrices. The middle column presents the contribution of local misfit to the total misfit (eq: (4.10)–(4.11)). In the last column the local ratio is presented as calculated by eq. (4.10)–(4.11) 75

C.1 Case HS1: Misfits between 3D and 1D for real & imaginary parts and contributions of displacements & rotations over frequency 80
C.2 Case HS2, bedrock at 50m: Misfits between 3D and 1D for real & imaginary parts and contributions of displacements & rotations over frequency 81
C.3 Case HS2, bedrock at 100m: Misfits between 3D and 1D for real & imaginary parts and contributions of displacements & rotations over frequency 82
C.4 Case HS2, bedrock at 200m: Misfits between 3D and 1D for real & imaginary parts and contributions of displacements & rotations over frequency 83

LIST OF TABLES

3.1 Model parameters 10

4.1 Total misfits for the mass and damping matrices as calculated by taking the sum over all local misfits. 30
4.2 Total misfits for the mass and damping matrices as calculated by taking the sum over all local misfits for different L/D's. L/D=4 is reference case. 31

5.1 Case HS1: Real and imaginary misfits between 3D response and approximated response for the frequencies 0.3 and 0.9 Hz. 43
5.2 Case HS2, bedrock at 50m: Real and imaginary misfits between 3D response and approximated response for the frequencies 0.3 and 0.9 Hz. 43

6.1 Used properties of upwind 3-bladed NREL 5-MW wind turbine [41] 51

A.1 Soil stratigraphies 71

C.1 Case HS1: Real and imaginary misfits between 3D response and approximated response for the frequencies 0 – 0.3 – 0.6 – 0.9 Hz 78
C.2 Case HS1: Real and imaginary misfits between 3D response and approximated response for the frequencies 1.5 – 2.0 – 2.5 – 3.0 Hz 78
C.3 Case HS2, bedrock at 50m: Real and imaginary misfits between 3D response and approximated response for the frequencies 0 – 0.3 – 0.6 – 0.9 Hz 78
C.4 Case HS2, bedrock at 50m: Real and imaginary misfits between 3D response and approximated response for the frequencies 1.5 – 2.0 – 2.5 – 2.8 Hz 78
C.5 Case HS2, bedrock at 100m: Real and imaginary misfits between 3D response and approximated response for the frequencies 0 – 0.3 – 0.6 – 0.9 Hz 79
C.6 Case HS2, bedrock at 100m: Real and imaginary misfits between 3D response and approximated response for the frequencies 1.5 – 2.0 – 2.5 – 2.8 Hz 79
C.7 Case HS2, bedrock at 200m: Real and imaginary misfits between 3D response and approximated response for the frequencies 0 – 0.3 – 0.6 – 0.9 Hz 79
C.8 Case HS2, bedrock at 200m: Real and imaginary misfits between 3D response and approximated response for the frequencies 1.5 – 2.0 – 2.5 – 2.8 Hz 79

1

INTRODUCTION

1.1. GENERAL INTRODUCTION OFFSHORE WIND

With increasing evidence of accelerated climate change, the need of sustainable, non-polluting, energy sources become evident. The agreement in the 2015 Paris UN Climate Change conference[6] sends a clear signal to investors, businesses and policy-makers that a global transition to sustainable energy is necessary and resources have to shift away from polluting fossil fuels. Offshore wind energy shows promising to contribute to this transition.

The offshore wind industry has developed rapidly over the last 27 years, since the installation of the first offshore wind farm in 1991 in Vindeby, Denmark. Figure 1.1 shows the annual and cumulative installed capacity of offshore wind in Europe. According to Europe Wind (2018) the capacity reached 15,780 MW by the end of 2017 in Europe . There are now 92 offshore wind farms in 11 European countries containing 4,149 wind grid-connected turbines, including sites with partial grid connection. Most of these turbines are situated in the North Sea. The growth line shows an exponential increase of installed capacity. From the cumulative installed capacity, monopiles remain the most popular substructure type with 81.7% of all installed substructures in Europe [1].

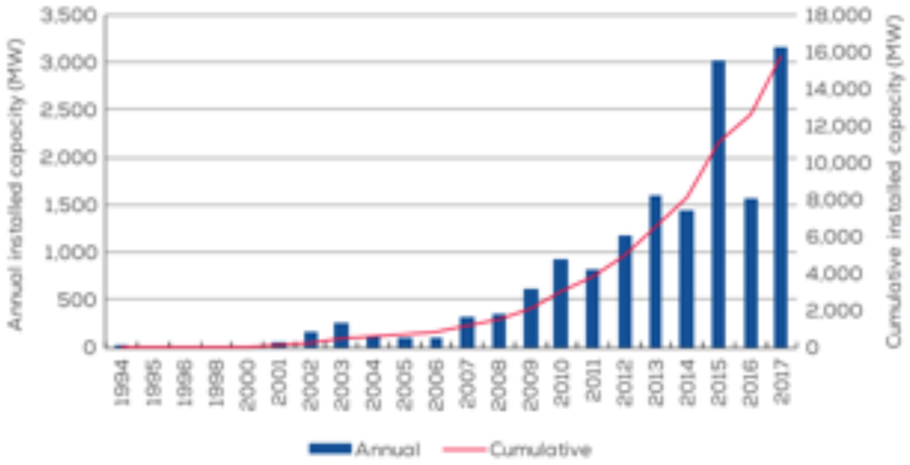

Figure 1.1: WindEurope (2018) - cumulative and annual offshore wind installations (MW) [1]

Considering the wide use of monopile substructures, this thesis focuses on that foundation type. There are many uncertainties in correctly modelling the soil-structure interaction between a rigidly behaving monopile and the soil.

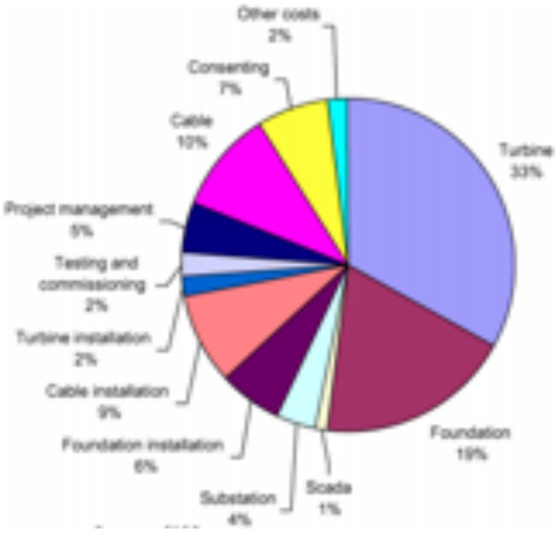

Figure 1.2: Estimate of capital cost breakdown for an offshore wind farm [2]

In order for offshore wind-generated energy to become more competitive with conventional energy, the costs requisites to reduce. The costs of monopile support structures typically constitute more than 20% of the total capital cost of an offshore wind farm (see figure 1.2 and other [7][8]) , opportunities are sought to reduce the cost of support structures.

1.1.1. SOIL-STRUCTURE INTERACTION

Different authors [9][10][7] have shown that the measured fundamental natural frequencies of installed offshore wind turbines are often higher than predicted during the design stage. This means that the structural response is expected to be stiffer than anticipated. Offshore wind turbines are therefore likely to be overdimensioned, indicating a waste of steel and redundant resulting costs. A possible explanation for this discrepancy is found in the modelling of soil-structure interaction (SSI).

If a pile is exposed to dynamic loads, such as, and not limited to, waves, wind and current, these loads will cause a structural response that interacts with the soil medium surrounding the pile. This interaction phenomena is called soil-structure interaction, or SSI. SSI attempts to combine the response of a structure and soil medium. In the offshore wind industry, SSI is commonly modelled as a local Winkler foundation with local nonlinear elastic springs to represent the soil lateral stiffness. The stiffness is often derived in accordance with the $p-y$ method. This method takes into account the semi-empirical relations between lateral displacement y of the pile and the soil pressure (p). This method is adopted by the API [11] and DNV [5] design codes. The empirical relations are developed during field tests with slender piles. However, with increasing dimensions of offshore wind turbines, questions arise about the validity of this method. An important difference between rigid and flexible soil-structure interaction is that large diameter, rigidly behaving, monopiles tend to experience a more global (non-local) reaction of the soil, where flexible piles experience a local reaction of the soil. The non-local effect is not captured in the method adopted by the most commonly used design codes.

Versteijlen [7] developed a state-of-art method to capture complex valued non-local dynamic stiffness from a 3D finite elements model in an approximated 1D beam model on a non-local Winkler foundation. The technique mimics the complex 3D dynamic response of a vast range of soil-pile systems with a computationally efficient 1D model. Herein global stiffness matrices are extracted from a 3D soil continuum and placed in a 1D model. An important contribution of this work is that it captures the dynamic stiffness of the global (non-local) soil continuum. The method is validated according to real size experiments in the frequency domain. The method shows promising in modelling soil-structure interaction in the frequency domain. This thesis studies the frequency dependency and damping of the non-local model formulation and, subsequently, translates the method to the time domain where time varying (non-linear) loading can be included.

1.2. RESEARCH DESCRIPTION

A new method is explored in this thesis to perform one-dimensional (1D) time-domain computations of the response of offshore wind turbines to wave, current and wind loading. The non-local method that of Versteijlen [7] is used to extract the frequency-dependent complex-valued dynamic soil stiffness from a three-dimensional (3D) linear-elastic (LE) Finite Elements (FE) model. The frequency dependence of the dynamic soil stiffness is analysed. Frequency-independent added mass, stiffness and damping coefficient matrices are derived that accurately represent the 3D soil continuum response in and around the monopile. These are included in 1D frequency-time-domain Timoshenko beam models on a non-local Winkler foundation. The performance of these models in representing the SSI response of an offshore wind turbine is measured in both the frequency and time domain.

1.3. RESEARCH OBJECTIVE AND CHALLENGES

The objective of this research is to develop a method to perform time-domain computations of OWTs wherein 3D dynamic stiffness kernels of the soil are incorporated. Sub-objectives are:

- Assess the frequency dependency of the dynamic stiffness for different types of soil configurations.
- Evaluate the range of applicability and the limitations of the non local model.
- Approximate the 3D dynamic stiffness with frequency independent coefficient matrices, to set the boundary conditions for this simplification and to evaluate their importance for OWTs.
- Study the performance of the non-local formulation with focus on the frequency dependence of the model.
- Evaluate if the 3D dynamic stiffness can be assumed to be frequency independent.
- Perform 1D time-domain computations for offshore wind turbines when subjected to aerodynamic and hydrodynamic loading and incorporate 3D dynamic stiffness.

1.4. APPROACH

The used approach to develop the 1D model of an offshore wind turbine of a non-local winkler foundation with aerodynamic and hydrodynamic loading is listed below:

- Literature research to examine which methods are commonly applied to calculate the SSI response of laterally loaded piles embedded in soil.
- Assess the frequency dependency of dynamic soil stiffness for different boundary conditions in heterogeneous soil stratigraphy.
- Derive frequency-independent added mass, damping and stiffness coefficient matrices that represent the 3D dynamic soil stiffness, as calculated by a 3D finite elements model.
- Develop a 1D Timoshenko beam model on a non-local Winkler foundation.
- Frequency-domain analysis to validate the performance of the 1D model to represent the 3D SSI response.
- Include aerodynamic and hydrodynamic loading scenarios.
- Perform time-domain analysis with a 1D model of an offshore wind turbine.

2

STRUCTURE-SOIL INTERACTION MODELLING

2.1. INTRODUCTION

When external forces, such as waves, wind, earthquakes and current, act on a structure that is in direct contact with soil, the structural displacement and the displacement of the ground are dependent on each other. The interaction effect between the response of the structure influencing the motion of the soil, and visa verse, is called soil-structure interaction (SSI). In case of an OWT, hydrodynamic and aerodynamic forces act on the structure and the soil keeps the structure in place. Piles resist lateral loads by means of shear, bending and soil resistance. The total resistance depends on properties of the pile and soil, i.e. the pile stiffness, pile strength, soil type, soil stiffness, soil strength and the applied boundary conditions at the pile ends (fixed, hinged or free) [12]. The soil generates damping through energy radiation and dissipation. Energy dissipation is mainly caused by material damping in the soil [13]. Propagation of progressive waves cause energy radiation [14]. However, authors have pointed out that the effect of energy radiation at vibration frequencies below 1 Hertz (Hz) is negligible [13].

2.2. CONVENTIONAL MODELS AND LIMITATIONS

This section explains the current foundation design methodology of soil-structure interaction for offshore wind applications. A brief explanation of the method is given, followed by the limitations when applied to large diameter rigidly behaving OWT monopiles.

Laterally loaded offshore wind turbine monopiles are usually designed based on the Winkler approach, considering a beam supported by local nonlinear elastic springs that represent the soil lateral stiffness [15]. The Winkler approach takes into account the semi-empirical relations between the lateral displacement (y) of the pile and the soil pressure (p) acting on the pile wall at specific depths and, consequently, soil layers along the pile. In the $p-y$ curve method, the pile is modelled as a beam and the soil is represented by a series of discrete, uncoupled, nonlinear elastic springs at nonal points along the pile [13]. This $p-y$ method describes the nonlinear relation between the local pile deflection and local lateral soil resistance and is a linear function of depth below the mudline. Figure 2.1 shows this method. The method was developed for various soil types. In the API and DNV design codes [11][5], this method is the recommended approach for lateral pile design [16]. The method was originally developed for onshore applications with significantly smaller pile diameters and is based on a very limited number of tests. The method is adopted by the oil and gas industry and as widely applied in offshore applications[17]. Nowadays it is clear that these methods for designing offshore wind turbine monopile geometrics may not be appropriate [18][10].

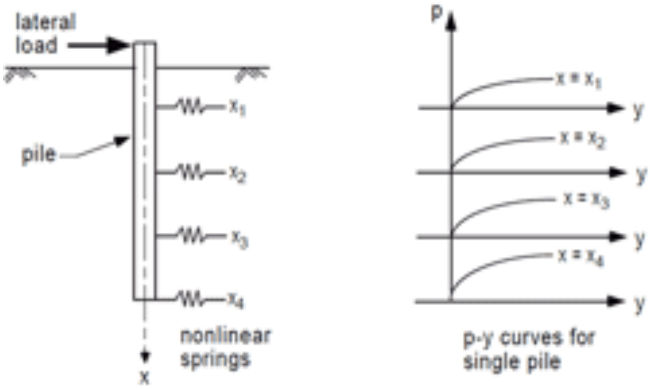

Figure 2.1: $p-y$ curve method

In the API and DNV design codes, the currently adopted formulation to describe SSI in sand consists of four equations [19]:

$$p(y,z) = AP_u tanh\left(\frac{kzy}{AP_{ult}}\right) \tag{2.1}$$

Where p_{ult} is the ultimate lateral resistance at depth z below the seabed in [kN/m], y is the lateral deflection in [m], A is a factor to account for static or cyclic loading conditions. $A = (3-0.8z/D) \geq 0.9$ for static loading and $A = 0.9$ for cyclic loading. k represents the initial coefficient of subgrade reaction. It depends on the angle of internal friction and the relative density of the cohesionless soil [20]. It can be calculated by equation (2.2):

$$k = (0.008085\psi^{2.45} - 26.09)10^3 \qquad \text{for } 29^\circ \leq \psi \leq 45^\circ \tag{2.2}$$

Where ψ is the angle of internal friction in degrees.

The ultimate lateral resistance p_u is determined by equation (2.3) [21]:

$$p_{ult}(z) = min\begin{cases} (C_1 z + C_2 D_p)\gamma z & \text{shallow depths} \\ (C_3 D_p \gamma z) & \text{deep depths} \end{cases} \tag{2.3}$$

Where γ is the effective soil weight in [KN/m^3]. D_p is the average diameter of the pile from seabed to depth in [m]. With $C_1 = 0.115 \cdot 10^{0.0405\psi}$, $C_2 = 0.571 \cdot 10^{0.022\psi}$ and $C_3 = 0.646 \cdot 10^{0.0555\psi}$.

Note that the formulations above are developed to determine the load-deflection ($p-y$) curves for sand. For other soil stratigraphies,such as clay or rock, other formulations are included in the API codes.

With the fundamental design curves that are incorporated in the $p-y$ curve method being calibrated on data obtained by measurements with piles up to 1.2 meters, there are serious doubts about the method's empirical validity upon extrapolation for piles up to 5 meters in diameter [22]. Flexible and rigid piles behave differently when laterally loaded. Typically, offshore piles for the oil and gas industry are classified as flexible piles with high slenderness ratios (high length over depth (L/D) ratio). Failure is generally defined by the realization of bending resistance of the pile, with relatively low yielding of the surrounding soil. Any vertical shear resistance offered by the soil to the pile rotation is considered insignificant [23]. On the other side, monopiles used in the offshore wind industry, can be considered as more rigid (low L/D ratio) and experience both bending and rotational failure mechanisms [22]. The larger surface area experiences a significant vertical shear resistance, and related moment, offered by the soil to the pile rotation [23]. Rigid pile also experience large shearing forces due to displacements of the pile tip i.e. toe-kick. The toe-kick can be seen at the bottom in the left subfigure of figure 2.2. This phenomena is not captured by the $p-y$ method. Rigid, large diameter, piles experience a more global (non-local) reaction of the soil, where flexible piles experience a local reaction of the soil.

Another limitation of the $p-y$ method is that the formulation is based on piles installed in homogeneous soil. In practice however, the piles are often installed in strongly layered stratification. The effect of layered soil and the interaction between different layers is not taken into account in the $p-y$ method.

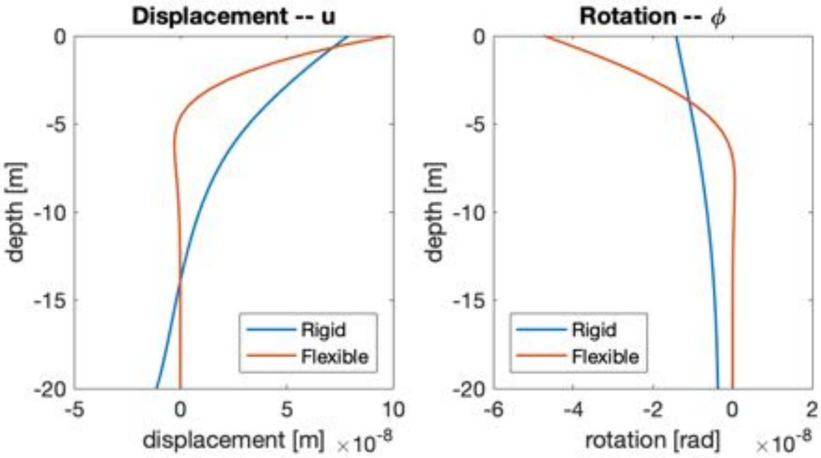

Figure 2.2: Rigid versus flexible pile response when subjected to lateral loading. A static force of 1N and moment of 45 Nm are applied to the pile head. The rigid pile has an L/D of 2 and the flexible pile has an L/D of 20. To compare the shapes, the rigid displacements and rotations are respectively multiplied by a factor 60 and 80.

Jia [9] notes that in the extrapolation process from small diameter piles to large pile diameters, the $p-y$ curves generally strongly overestimate the stiffness under significant lateral loading, while strongly underestimating the stiffness under small magnitude of loading. Byrne *et al.* [10] showns in his research that $p-y$ curves under-predict the SSI stiffness in clay and over-predict stiffness in sand for long slender piles. This work also shows that the soil stiffness is under-predicted for short and rigidly behaving piles in both sand an clay. Hübler *et al.* [24] recognize big differences between numerical and empirical results for dynamic loading conditions. This is caused by $p-y$ methods originally being developed for static loads and not for dynamic loads. Different $p-y$ methods are examined and the conclusion is that none of them are suitable for dynamic loading conditions of offshore wind farms. Furthermore, Hübler *et al.* [24] and Kallehave *et al.* [25] compared the natural frequencies of installed OWTs and the predictions by the API $p-y$ curves and conclude that, on average, the $p-y$ method under-estimates the natural frequencies by 10%. Both over-estimation or under-estimation of foundation stiffness is undesirable because it can lead to under-/ or over-dimensioning of OWTs.

The under-estimation of both small strain stiffness and the natural frequency of rigidly behaving monopiles is also confirmed by full-scale field measurements performed in the work of Versteijlen [7]. The results demonstrate that the currently used $p-y$ curves method strongly under-estimates the small strain stiffness of the lateral response of monopiles embedded in soil. The $p-y$ curve method under-estimates the stiffness of full-scale measurements with 140%.

Despite the limitations and uncertainties about applying this method to large diameter monopiles, this method has some large advantages. It captures the nonlinearity of a soil medium and the contact phenomena (gap and slippage) between the pile and the surrounding soil, which is difficult to model [9]. It is a strait forward method that can easily be implement in computationally efficient 1D models. The method suffices for flexible piles and has successfully been used for many years.

Many authors have recognized the limitations of the $p-y$ curves that are adopted by the API codes and have attempted to make improvements. Some methods show improvements in fits between 3D finite element models and models based on improved $p-y$ curves. However, Hübler *et al.* [24], Bouzid [20] and Jia [9] conclude that non of the currently available $p-y$ curve methods show satisfying results in predicting the SSI response of rigidly behaving, large diameter, piles.
The conclusion is that the currently applied $p-y$ curve methods show many limitations in describing the SSI of large diameter offshore wind turbines. The uncertainties of SSI modelling based on $p-y$ curves provide an incentive in this work to look into alternative, less empirical, modelling techniques.

2.3. STATE-OF-ART SSI MODELLING

This section emphasizes on state-of-art modelling techniques for soil-structure interaction. A literature review is performed to identify improved modelling techniques and address their performance, advantages and limitations in capturing SSI for large diameter, rigidly behaving, monopiles.

2.3.1. 3D CONTINUUM MODELLING

Three-dimensional (3D) continuum models may be the most accurate and flexible modelling method to capture SSI. Many authors recommend this approach to calculate the response of large diameter piles, given the uncertainties of the most widely applied $p-y$ method [10] [26]. 3D finite elements models can capture the reaction mechanisms between the soil-pile system and non-local behaviour. It can also capture rotational stiffness and pile tip shearing effects [7]. However, due to the complexity of these types of models, high computational power is needed and computations are often time consuming [27]. In addition, phenomena such as gap forming, scour, liquefaction and cyclic loading effects can be challenging to model [27]. Versteijlen [7] states that currently about 120,000 10-min time-domain simulations are preformed for average offshore wind turbine design cases. Given the large computational time, full 3D time-domain simulations might not be appropriate for offshore wind turbine design.

2.3.2. HYBRID METHODS

The design of offshore wind turbines requires many time-domain simulations. These simulations need to be both fast and accurate. Currently, authors developing computationally efficient 1D models to predict soil-structure interaction wherein accurate 3D soil reactions can be incorporated. Impressive steps are made in the work of Versteijlen [7]. A method is developed to calculate global stiffness kernels for the lateral and rotational. These global stiffness kernels automatically incorporate distributed lateral and rotational springs along the pile or similar discrete springs at the pile tip. The method was shown to yield accurate fits of static and dynamic response for a very large range of SSI systems in terms of relative pile stiffness. The stiffness kernels were incorporated in an efficient 1D frequency-domain model to calculate the SSI response. In this thesis, the global stiffness kernels are approximated as frequency-independent added mass, stiffness and damping coefficient matrices. The transformation into the time domain is important since it allows the user to incorporated nonlinear wave and wind loading and air-turbine interaction effects that are considered to have a major impact on the resulting dynamic system response.

3

MATLAB BASED 3D FE MODEL

3.1. INTRODUCTION 3D MODEL

To assess the complex soil-structure interaction and to determine complex valued non-local dynamic soil stiffness of a soil continuum, a Matlab based 3D Finite Elements (FE) model is developed by Barbosa [28]. In this model, a linear-elastic 3D soil continuum is modelled with a pile or a cavity. In reality the soil reacts in a nonlinear manner when loaded. Pile installation effects, gap-separation and hardening/softening of the soil for cyclic loading are neglected in this thesis. The validation in the work of Versteijlen [7] has shown that the assumption of linear-elastic soil reactions is acceptable in the small strain (small displacements) regime. The 3D system is decomposed into a set of 2D problems. The pile and soil are independently characterized and modeled with solid finite elements [29]. The model allows for different pile dimensions and types of soil stratigraphy, such as homogeneous and heterogeneous layered soil. An advantage of a 3D model is that conceptually it should be the most accurate method to assess the dynamic response of a pile embedded in soil. Another advantage is that this method does not rely on empirical models that are developed for piles with predefined dimensions. A disadvantage of 3D FE models is the high computational time, hence the later transformation to a more computationally efficient single degree of freedom system (SDOF). The model will be used to evaluate the fit between 3D and 1D frequency-domain computations and to extract frequency-independent dynamic soil stiffness coefficients matrices that can be incorporated in a 1D model formulation.

3.2. MODEL SET-UP

The model is developed for two calculations:

1. Frequency-domain calculation of non-local complex-valued dynamic soil stiffness
2. Frequency-domain calculation of the complex-valued response of a pile embedded in a soil stratigraphy

The properties and geometry of the soil continuum are the same for both calculations, because the 1D model should match the 3D formulation if the results are to be compared. Section 3.3.1 describes how the soil is discretized and which boundary conditions are applied to the domain.

3.2.1. CALCULATION OF THE RESPONSE OF A PILE EMBEDDED IN SOIL

The 3D model calculates the complex-valued response of a pile embedded in a 3D linear-elastic soil continuum. The pile and soil are independently characterized with solid finite elements. The pile is vertical, uniform, linearly elastic and of circular cross-section. The properties and geometry of the pile can easily be changed between different computations. The pile properties that are used in this thesis are listed in table 3.1. The embedded part of the pile is 20m and a mass-less tower of 10m above seabed is included to avoid numerical issues at the seabed. These additional 10 meters cause that a moment is automatically induced when the pile response is calculated. The diameter of the monopile is 5m and has a wall thickness of 0.05m. A force of 1N and moment of 45Nm are applied at the pile head to calculate the response in terms of complex-valued displacement and rotation. The extra moment caused by the mass-less tower is subtracted from the loading scenario. By making use of symmetry over the vertical axis, only half of the soil-cavity configuration is used in the computations. This considerably reduses the computational time needed for the calculation. Figure 3.1 gives a schematic representation of the 3D model used for structure-soil interaction.

Table 3.1: Model parameters

Pile properties			
Embedded length	L_s	20	m
Tower length	L_0	10	m
Outer diameter	D_0	5	m
Wall thickness	T	0.05	m
Pipe material density	ρ_p	7850	kg/m^3
Young's Modulus	E_p	210E9	N/m^2
Poisson's ratio	ν_p	0.3	-
Discretization length	dh	0.5	m
Excitation force	F	1	N
Overturning moment	m	45	Nm

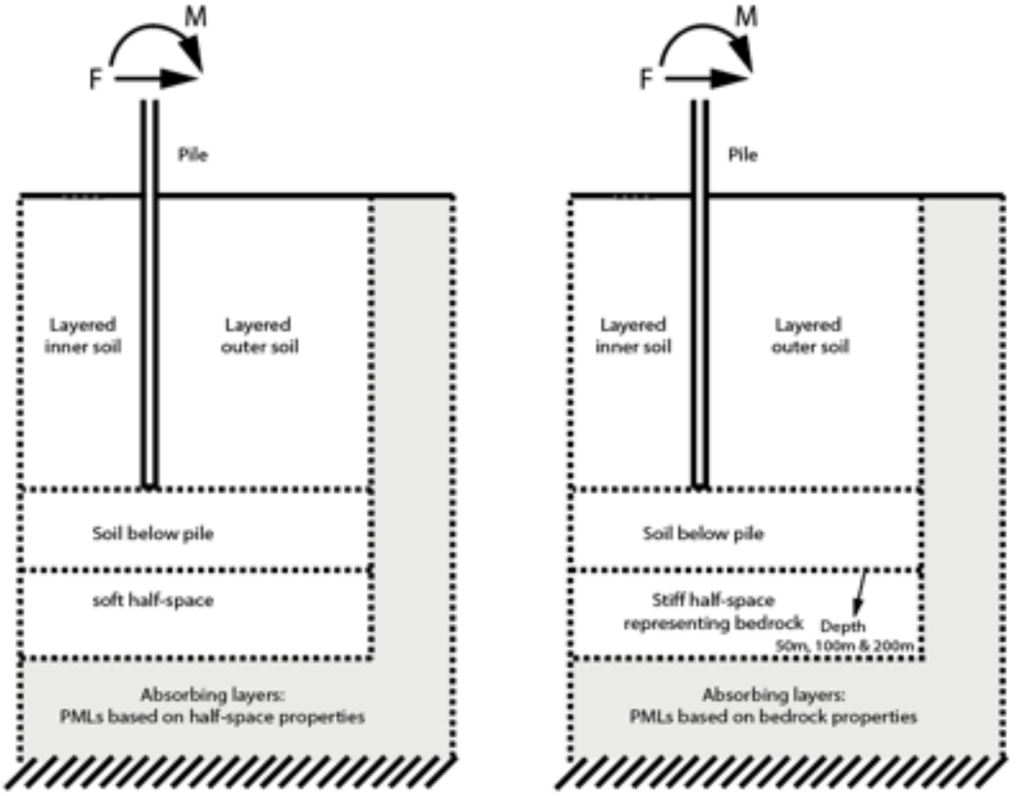
M
F
Pile
Layered inner soil
Layered outer soil
Soil below pile
soft half-space
Absorbing layers: PMLs based on half-space properties
M
F
Pile
Layered inner soil
Layered outer soil
Soil below pile
Stiff half-space representing bedrock
Depth 50m, 100m & 200m
Absorbing layers: PMLs based on bedrock properties

(a) 3D model infinite depth with horizontal and vertical PMLs. The properties of the PMLs are based on the half-space.

(b) 3D model with stiff vertical half-space, representing bedrock. The properties of the PMLs are based on the bedrock

Figure 3.1: Visual representation of 3D model for calculation of SSI response. Explanation about the two cases is given in section 3.3.1

3.2.2. CALCULATION OF THE COMPLEX-VALUED DYNAMIC STIFFNESS

In order to calculate dynamic stiffness kernels of the soil only, the area of the pile is now modelled as a cavity with soil in and around it. The cavity is given the same geometry as the pile. The length of the cavity is 20m from the seabed to the bottom. The diameter of the cavity is 5m with a cavity thickness of 0.05m. The dimensions are chosen to match the dimensions of the monopile that will be included in a later stage. Figure 3.2

gives a visual representation of the model. Again, computational time is saved by making use of symmetry over the vertical axis. Consequently, only half of the soil-cavity configuration is used in the computations. The dynamic stiffness kernels of the soil layers are derived, based on dynamic excitations of rings of nodes around the cavity surface. The boundary condition applied at the cavity surface is created so that the cavity is free of stress. The dynamic excitations are used to calculate the soil reaction at the location of the ring of nodes (local) and at all the surrounding (non-local) vertically spaced nodes. For every ring of nodes is a column vector filled with the soil reaction of all the vertically spaced layers, resulting in matrices that capture the non-local soil reactions. Flexibility matrices transform these to complex-valued dynamic stiffness kernels, in which the non-local behaviour of the soil is captured. The model generates four complex-valued dynamic stiffness matrices i.e. lateral stiffness ($\tilde{K}^{u,u}_{dyn}$), rotational stiffness ($\tilde{K}^{\phi,\phi}_{dyn}$) and two coupling stiffness matrices ($\tilde{K}^{u,\phi}_{dyn}$ & $\tilde{K}^{\phi,u}_{dyn}$). The lateral stiffness is calculated by applying a lateral force to the ring in the x-direction, resulting in a horizontal translation. The nodal horizontal translations at that ring and all vertically spaced rings are collected. The stiffness is calculated by taking the inverse of the translations. In a similar way, the rotational stiffness is calculated by applying a distributed moment at the ring and then collecting the rotations. The coupling stiffness matrices are derived by calculating the lateral translations caused by a distributed moment (rotation), and vice versa. The type of matrix is indicated with the superscript indices u and ϕ. i and j indicate the row and column in the matrices. The first index in the superscript of $K^{u,\phi}_{dyn}$ indicates the soil reaction to the second index. For example, $K^{u,\phi}_{dyn}$ is the matrix the captures the lateral soil reaction due to a rotation of the ring of nodes caused by a distributed moment. $\tilde{K}^{u,u}_{dyn}$ and $\tilde{K}^{\phi,\phi}_{dyn}$ are symmetric over the diagonal ($i, j = j, i$). $\tilde{K}^{u,\phi}_{dyn}$ and $\tilde{K}^{\phi,u}_{dyn}$ are transposed symmetric to each other ($\tilde{K}^{u,\phi}_{dyn_{i,j}} = \tilde{K}^{\phi,u}_{dyn_{j,i}}$). For more detailed explanation about the 3D model, advised is to refer to the dissertation of Versteijlen [7].

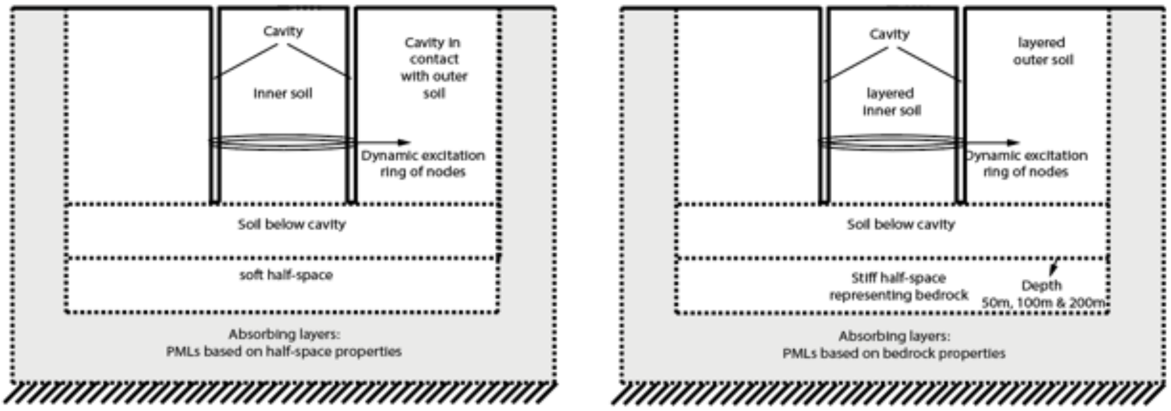
Cavity
Cavity in contact with outer soil
Inner soil
Dynamic excitation ring of nodes
Soil below cavity
soft half-space
Absorbing layers: PMLs based on half-space properties
Cavity
layered outer soil
layered inner soil
Dynamic excitation ring of nodes
Soil below cavity
Stiff half-space representing bedrock
Depth 50m, 100m & 200m
Absorbing layers: PMLs based on bedrock properties

(a) 3D model with boundary condition HS1. PMLs are based on properties of the half-space.

(b) 3D model with boundary condition HS2. PMLs are based on properties of the bedrock.

Figure 3.2: Visual representation of 3D model for calculation of dynamic stiffness. The Explanation about the two cases is given in section 3.3.1

3.3. SOIL CONTINUUM

3.3.1. DIMENSIONS, MESH SIZE AND BOUNDARY CONDITIONS OF SOIL MEDIUM

As the name "finite elements" suggests, a finite element model models the pile in a finite soil domain. One of the main challenges is to determine the correct dimensions, mesh size and boundary conditions for the model. Two types of waves are generated by the dynamic excitation of a ring of nodes; propagating and evanescent waves. The domain, mesh size and boundary conditions must be chosen so that reflections of these waves will not affect the results of the computations in a non-physical way. Evanescent waves could be damped out by material and geometric damping of the domain and should be prevented to reach the boundary of the model [30]. The domain being to small could lead to standing waves, interfering with the computation results. For propagating waves it is inevitable that they reach the boundary of the domain. Only if the domain becomes unreasonably large, they will damp out sufficiently. Therefore, boundary conditions need to be applied to prevent reflections with acceptable model dimensions. In reality the monopile is embedded in a soil medium with infinite dimensions in horizontal directions, because in reality there are no physical boundaries. Therefore, the 3D FE model should minimize horizontal reflections. In vertical direction there can be a stiff layer, working as a rigid boundary at a certain depth. In the vertical direction two typical sets of boundary conditions are applied in the 3D modelling.

- Boundary condition HS1: A half-space with Perfectly Matched Layers to absorb propagating waves (figure 3.1a & 3.2a)
- Boundary condition HS2: A stiff half-space (representing a rock layer (or equivalently, a rigid layer)) starting at a finite depth followed by Perfectly Matched Layers (figure 3.1b & 3.2b)

Different boundary conditions are required for a better understanding of the frequency dependence of dynamic soil stiffness and to get more certainty about the validity of the model. The actual soil conditions can well be represented by one of the two sets of BCs in most cases. BC HS1 is realistic in areas where there is no presence of a rock layer, as is the case in Dutch coastal areas. BC HS2 is realistic if there is a rock layer present in the seabed, for example in areas near volcanic activities.

A commonly used method to absorb propagating waves in discrete finite models is Perfectly Matched Layers, or PMLs [28]. The idea of this technique is that the outgoing waves enter a layer, where they are transformed into decaying evanescent waves to minimize the reflections at the boundary[31]. The method introduces an absorbing layer with uniform thickness that forces the waves to decay exponentially. The solution to the wave equation is changed from equation (3.1) to (3.2):

$$u(x,z,t) = u_x(z)e^{i(k_x x-\omega t)} \tag{3.1}$$

$$u(x,z,t) = u_x(z)e^{i(k_x x-\omega t)}e^{-A_x k_x \frac{x^p}{L^p}} \tag{3.2}$$

Note that this method is not developed for evanescent waves with complex-valued wavenumbers. PMLs are not effective in absorbing these types of waves [32][33]. An example of a wave with a complex-valued wavenumber and PMLs is presented in equation (3.3)[31].

$$u(x,z,t) = u_x(z)e^{-i\omega t}e^{-k_x x}e^{-A_x k_x \frac{x^p}{L^p}} \tag{3.3}$$

The decay of the evanescent wave will continue in the PML. However, a propagating part is added to the wave. This can cause reflections. Since evanescent waves decay automatically, a method to prevent these reflections is choosing the domain in such a way that the amplitudes of the evanescent waves are negligible at the start of the PML and the reflections from the PMLs do not influence the results. The PMLs are based on the properties of the half-space in the soil continuum. The dimensions of the PMLs are set in such a way that 10 wavelengths (equation (3.4)) fit in a PML and that 10 nodes describe a wave. For more information about PMLs, the reader is advised to review the work of Barbosa [28].

Equation (3.4) is used to determine the horizontal dimensions of the domain before the PMLs are introduced. It shows the relation between the wavelength, shear wave velocity and excitation frequency.

$$\lambda_h = \frac{\sqrt{G_h/\rho_h}}{f} = \frac{C_{s,h}}{f} \qquad [m] \tag{3.4}$$

Where λ $[m]$ is the wavelength of the half-space, G_h $[N/m^2]$ is the shear modulus of the half-space, $\rho_{s,h}$ $[kg/m^3]$ is the density of the half-space and f $[Hz]$ is the dynamic excitation frequency. The shear modulus is calculated by $G = \frac{E}{2(1+\nu)}$ $[N/m^2]$, with E = Young's Modulus $[N/m^2]$ and ν = Poisson's Ratio [-].

As presented in equation (3.4), the wavelength is dependent on the excitation frequency. For example, for a shear wave velocity of 350 m/s and a dynamic excitation frequency of 0.05 Hz, the resulting wavelength will be 700 meters. The dimensions of the 3D model should be sufficiently large, to make sure that standing waves do not interfere with the results of the computations. Jones [34] shows that the minimum depth of the soil layer over the homogeneous half-space should be 5 wavelengths (5λ) in order to get convergent results. Experimentally this is confirmed, resulting in a minimum soil domain radius of 3,500 meters. In this thesis, the domain is increased to fit 10 wavelengths for higher accuracy. The model will be excited for increasing dynamic loading frequencies. Therefore, dynamically changing soil dimensions are applied using the following relations:

$$Dim = 10\lambda \qquad [m] \tag{3.5}$$

$$Maxdx = \frac{\lambda}{10} \qquad [m] \tag{3.6}$$

The mesh size is gradually increased, away from the modelled cavity, to reduce computational time. The maximum mesh size ($Maxdx$) is chosen in such a way that at least 10 nodes describe a wave.

As mentioned before, two types of boundary conditions (BCs) are applied in the vertical direction. The first boundary condition (BC HS1) consists of a (soft) half-space with PMLs after 10 wavelengths. The half-space is given the same properties as the bottom soil layer, as defined in section 4.3.1. The second boundary condition (BC HS2) is consists of a stiff half-space, representing bedrock (or, equivalently, a rigid layer) and PMLs after 10 wavelengths. The effect of stiff half-space to the dynamic stiffness is assessed for three depths – 50m, 100m and 200m. These depths indicate the depth below seabed at which the stiff half-space starts. In both cases, the soil surrounding the cavity and an buffer layer of 20m is vertically discretized in steps of 0.5m. To save computational effort, the soil below the buffer layer is discretized by increasing mesh sizes with a maximum length of $Maxdx$. Furthermore, 20 PMLs are added with an uniform discretization length of $Maxdx$. The discretization of a part of the soil medium is presented in figure 3.3.

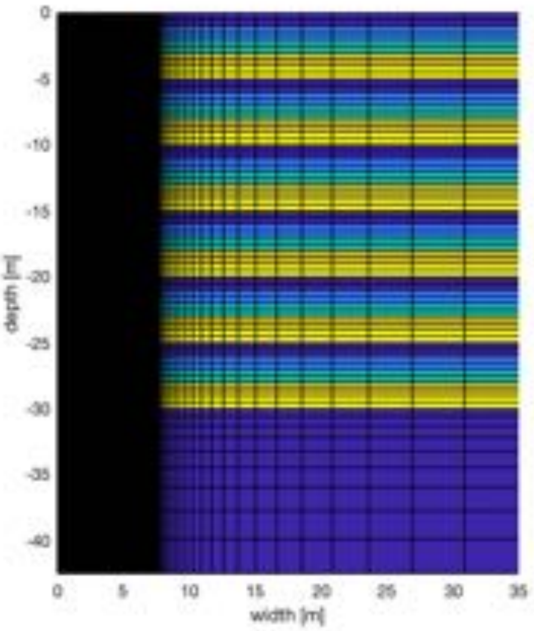

Figure 3.3: Varying Young's Modulus

3.3.2. VISCOUS DAMPING

The performance of the 1D model to represent the 3D response of the pile-soil configuration will be measured in section 5.3. Consequently, the damping mechanism between the two models need to be matched. Viscous dampers will be included in the 1D model formulation. Consequently, there should not be any damping in the model at an excitation frequency of 0 Hz. The damping mechanisms between the models are matched by adding a frequency-dependent term (ω) to the complex-valued shear modulus. The shear modulus in the 3D model is thereby made viscous. The modification is shown in equations (3.7) and (3.8).

$$G^* = G(1+2i\eta) \tag{3.7}$$

$$G^* = G(1+i\omega\eta) \tag{3.8}$$

where, G^* = complex-valued shear modulus, ω = angular frequency [rad/s], η = soil material damping ratio = 2%.

3.3.3. STRATIGRAPHY

In this research, two types of soil stratigraphies are developed to assess the frequency dependence of complex-valued dynamic soil stiffness: S1 (realistic heterogeneous stratigraphy) and S2 (homogeneous stratigraphy). The main focus of this thesis is soil stratigraphy S1. Figure 3.4 shows the soil configurations as a function of depth [m] for the two soil stratigraphies and an additional third stratigraphy consisting of two layers (2-layers) is added. The latter has the same properties as S2, but the first layers are made softer. Note that the half-space may have different properties than shown in this figure. The Poisson's ratio is kept constant between the cases. For BC HS1, the half-space is given the same Young's Modulus and density as the values at depth -40m in figure 3.4. For BC HS2, the half-space is made stiffer by setting the density to 2700 kg/m^3 and Young's Modulus to 4.6E10 Pa, representing rock. Additionally, the material damping ratio is increased from 2% to 10%. A table presenting the values of soil properties for different layers is presented in appendix A.

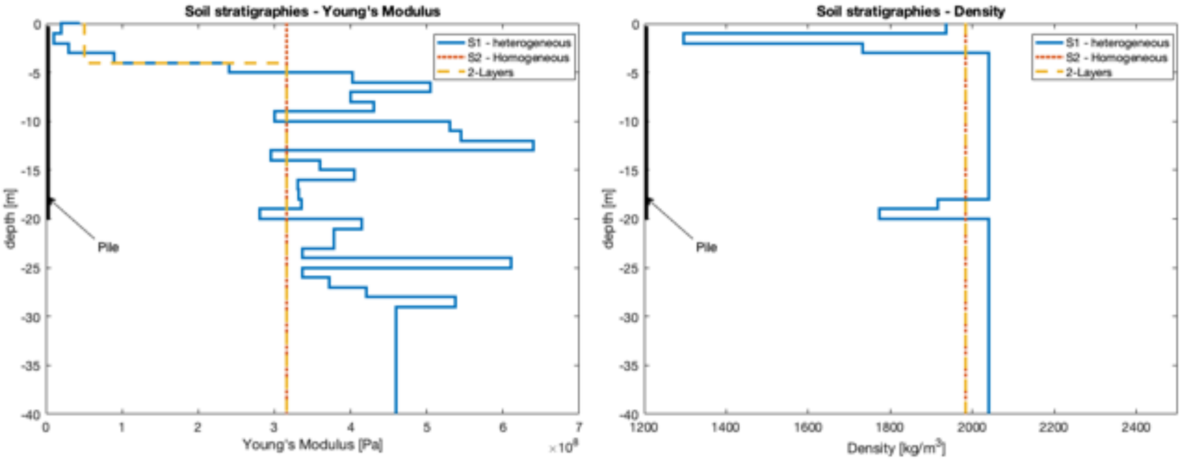

(a) Varying Young's Modulus

(b) Varying soil density

Figure 3.4: Different soil configurations

3.4. SSI RESPONSE

The SSI response of a monopile embedded in the three types of soil stratigraphies, as presented in figure 3.4, is calculated for excitation frequencies of 0 to 7.5 Hz, or, equivalently, 0 to 47.1 rad/s. The 3D SSI response is computed by the 3D model for increasing dynamic excitation frequencies. The vertical boundary condition of the soil continuum applied during the computations is BC HS1. The pile characteristics is kept constant between the computations. A dynamic force of 1N and a moment of 45Nm are applied 10m above the seabed on a mass-less fictive tower.

Figure 3.5 illustrates the effect of excitation frequency on the resulting normalized real and imaginary 3D global pile deflections (both lateral displacement and rotation) in soil as a function of depth from seabed to the pile tip. This is shown for the three stratigraphies (presented in figure 3.4). The normalized response is shown for excitation frequencies from 0 Hz to 7.5 Hz. The figures illustrate that an equal average in Young's Modulus does not yield comparable results (S1–S2). The SSI response in soil S2 exhibits less frequency-dependent behaviour than SSI in soil S1, hence the smaller change of normalized displacements and rotation. It is expected that the higher sensitivity to loading frequency of S1 is caused by the relatively soft soil layers near the seabed. To validate this hypothesis, figure 3.5c is added. The stratigraphy of two layers is given the same soil properties as S2, but with softer layers (comparable to S1) near seabed. The softer layers yield an increase in frequency dependence and leads to a response that is nearly identical to the SSI response in stratigraphy S1 (figure 3.5a). The stiffness of the upper layers of the soil profile has a dominant influence on the SSI response of the pile. This is also confirmed by figure 3.6. This figure presents the SSI pile head displacements as a function of excitation frequency for the different soil stratigraphies. The normalized imaginary displacements and rotations are larger than the normalized real-valued response. This justifies the conclusion that the imaginary part of the SSI response is more sensitive to the frequency of excitation (higher frequency dependence) than the real response. The 3D SSI response for different excitation frequencies is used to validate the performance of the 1D model in terms of representing the 3D SSI response 5.3.

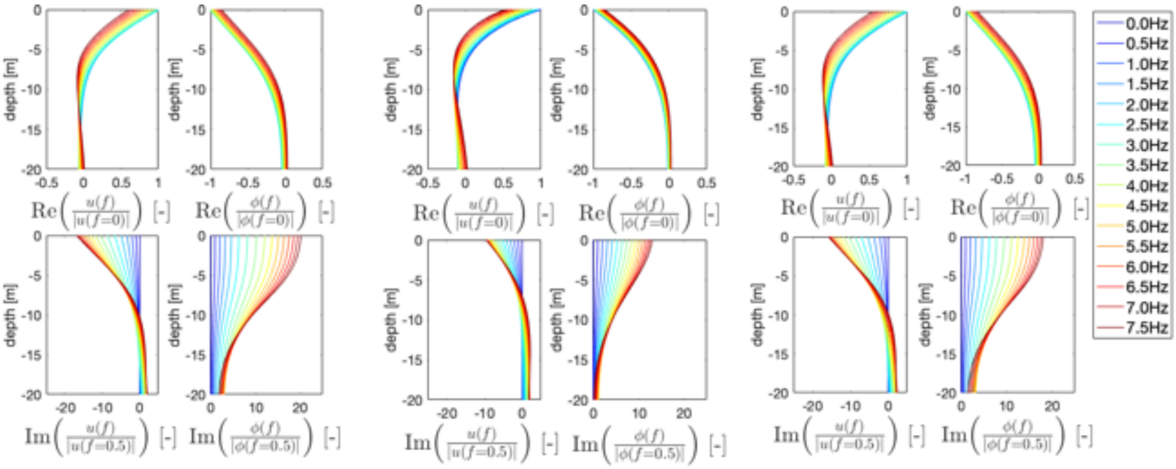

(a) S1 - Heterogeneous stratigraphy (b) S2 - Homogeneous stratigraphy (c) 2-layers stratigraphy

Figure 3.5: Normalized real and imaginary lateral displacement and rotation for the three different soil stratigraphies. The force and moment are respectively 1 N and 45 N/m and are applied to the top of the soil-pile system. The excitation frequencies increase from 0 Hz (blue) to 7.5 Hz (red) for BC HS1. Re(u(f)) and Re(ϕ(f)) are normalized by the absolute static Re(u(f=0)) and Re(ϕ(f=0.5)). Im(u(f)) and Im(ϕ(f)) are normalized by absolute Re(u(f=0)) and Re(ϕ(f=0.5)).

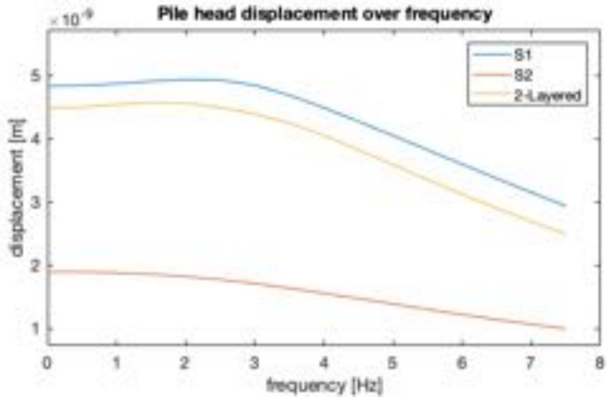

Figure 3.6: Pile head displacement as a function of excitation frequency. An dynamic force of 1N and moment of 45Nm is applied to the three SSI cases.

4

DYNAMIC SOIL STIFFNESS

This chapter focuses on dynamic soil stiffness. Section 4.1 presents the complex-valued dynamic stiffness matrices, as calculated by the 3D model, are presented. It also addresses non-local behaviour of the soil. Section 4.2 presents the frequency-independent added mass, damping and stiffness framework that is applied in this thesis. In section 4.3.1, the frequency-dependent behaviour of dynamic soil stiffness is analyzed. Section 4.4 explains how the frequency-dependent dynamic stiffness is approximated by frequency-independent impedance functions (coefficient matrices) and analyses the performance of these functions. Finally, section 4.5.1 evaluates the importance of added mass.

4.1. MATRICES AND NON-LOCALITY

This section presents the real and imaginary dynamic soil stiffness matrices and addresses non-locality. Please note that there is no pile present. The main focus is on soil stratigraphy S1, representing a realistic soil profile. A distinction can be made between the local and non-local contribution to the global dynamic stiffness. It is expected that the largest contribution to the global dynamic stiffness comes from the local nodes – the resulting stiffness of the soil layer at the location of the dynamically excited ring of nodes – and nearby surrounding non-local nodes. The real and imaginary dynamic stiffness matrices are presented in figures 4.1 and 4.2 for BC HS1 and soil stratigraphy S1. This is shown for an excitation frequency of 0.3 Hz, which is a typical vibration frequency for offshore wind turbines. The real and imaginary parts of the dynamic stiffness are presented separately. The matrices are presented against a linear and a logarithmic increasing colour scale. The results are shown on a logarithmic scales to address the non-local behaviour of the dynamic soil stiffness. The absolute values of real and imaginary elements of the matrices are computed to present the data on a logarithmic scale.

A general remark on all matrices is that the real and imaginary parts of the dynamic stiffness show large correlation in shapes. The following relation is observed in order to relate the magnitudes between the matrices:

- $\mathrm{Re}(K_{dyn}^{u,u}) \approx 25 \cdot \mathrm{Im}(K_{dyn}^{u,u})$
- $\mathrm{Re}(K_{dyn}^{\phi,\phi}) \approx 24 \cdot \mathrm{Im}(K_{dyn}^{\phi,\phi})$
- $\mathrm{Re}(K_{dyn}^{u,\phi}, K_{dyn}^{\phi,u}) \approx 33 \cdot \mathrm{Im}(K_{dyn}^{u,\phi}, K_{dyn}^{\phi,u})$

Figure 4.1 presents the matrices $K_{dyn}^{u,u}$ and $K_{dyn}^{\phi,\phi}$. The matrices are symmetric over the diagonal and, as expected, the largest stiffness is concentrated around the diagonals. It is challenging to present the matrices in a way that show the development of when becoming more non-local. Much detail is lost when the values in the matrices are presented on a linear colour scale (left-hand-side figures). Therefore, the matrices are also presented on a logarithmic colour scale in the right-hand-side figures. Note that most of the non-local elements of the matrices have negative values and the diagonals (local element) have positive values. Approximately, the stiffness decreases smoothly by a factor 10 for every meter distance from the location where the ring of nodes was excited. In the bottom right plot of figure 4.1a, the imaginary part of the non-local lateral stiffness shows some minimums before the edges of the matrix. The non-local elements change sign (become positive) after that minimum. When a stiff half-space starts at 50m depth, all non-local elements remain negative

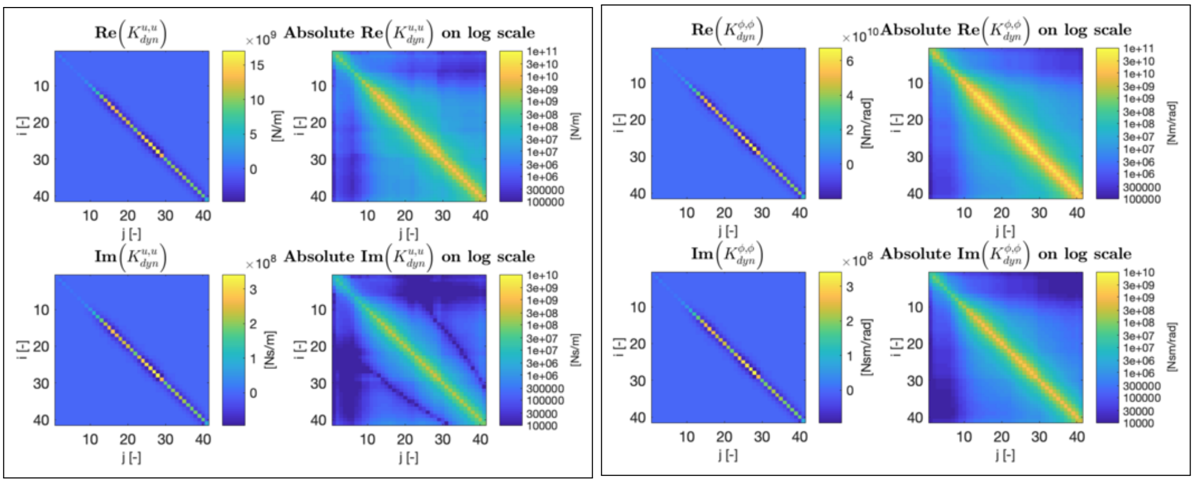

(a) Real and imaginary $K^{u,u}_{dyn}$

(b) Real and imaginary $K^{\phi,\phi}_{dyn}$

Figure 4.1: Real and imaginary dynamic lateral and rotational dynamic stiffness matrices are plotted on a linear and logarithmic scale. The matrices are derived for an excitation frequency of 0.3 Hz. BC HS1 and heterogeneous soil S1 are applied.

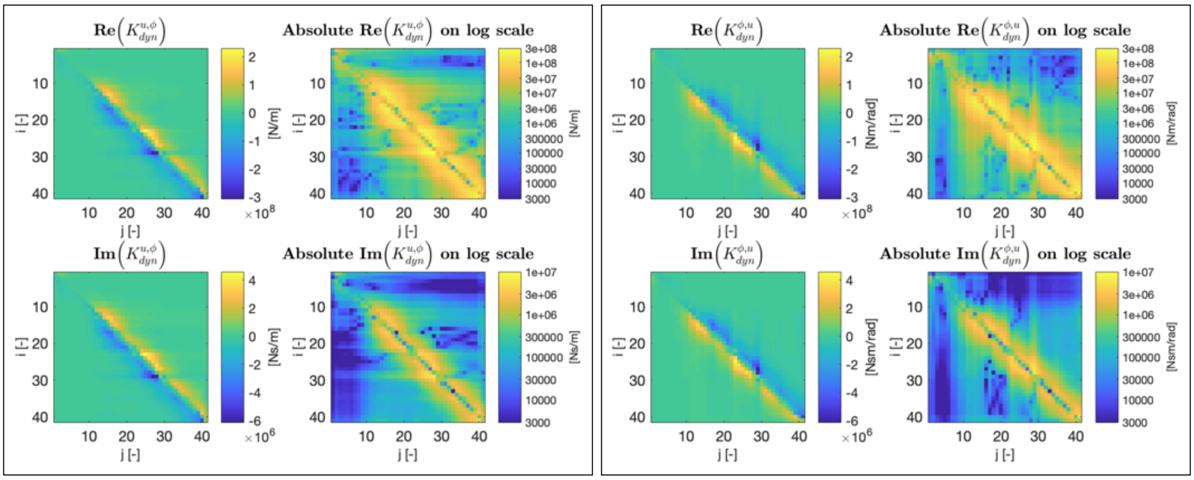

(a) Real and imaginary $K^{u,\phi}_{dyn}$

(b) Real and imaginary $K^{\phi,u}_{dyn}$

Figure 4.2: Real and imaginary dynamic coupling stiffness matrices are plotted on a linear and logarithmic scale. The matrices are derived for an xcitation frequency of 0.3 Hz. BC HS1 and heterogeneous soil S1 are applied.

and the magnitudes decrease smoothly away from the diagonal towards the edges of the matrices. An explanation of this phenomena is given in section 4.3.3

Figure 4.2 presents the matrices $K^{u,\phi}_{dyn}$ and $K^{\phi,u}_{dyn}$. The largest values in the matrices are concentrated in the near diagonal nodes and the decay of magnitude over distance is less smooth than in the coupling matrices. $K^{u,\phi}_{dyn}$ and $K^{\phi,u}_{dyn}$ have the following interrelation:

$$K^{u,\phi}_{dyn_{i,j}}) = K^{\phi,u}_{dyn_{j,i}}$$

Figure 4.3 shows the absolute magnitude of diagonals (local) and off-diagonals (non-local) of a couple of rows in the real parts $K^{u,u}_{dyn}$,$K^{\phi,\phi}_{dyn}$ and $K^{u,\phi}_{dyn}$ for an excitation frequency of 0.3 Hz. Hereby, the off-diagonal terms in the matrices are normalized with the diagonals. In the left and middle figure, the highest bar is the local stiffness. The stiffness of the surrounding soil layers is shown as bars to the left and right in steps of 0.5m. The degree of non-locality is slightly higher for $K^{\phi,\phi}$ than for $K^{u,u}$ as is shown by the horizontal line. For the lateral and rotational stiffness matrices ($K^{u,u}$ & $K^{\phi,\phi}$) the contribution to the global stiffness decays rapidly as the non-local stiffness is approximately 6% of the local stiffness at 1.5m from the excited node. For the coupling matrices ($K_{dyn}^{u,\phi}$ & $K_{dyn}^{\phi,u}$) near diagonal (non-local) contribution to the global stiffness is higher than the local stiffness. This justifies the conclusion that non-local dynamic stiffness is important to take into account. The imaginary parts of the dynamic stiffness matrices show the same non-local behaviour as the real parts.

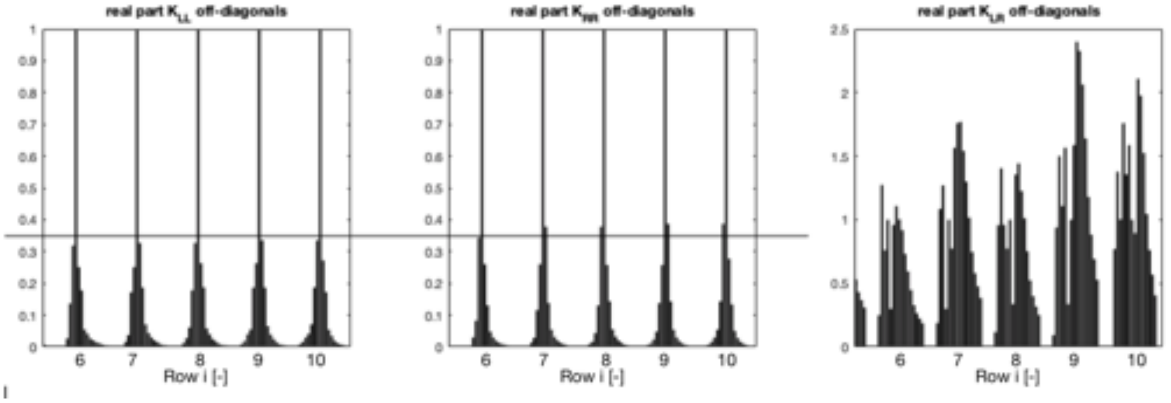

Figure 4.3: Normalized absolute magnitude of row i of local an non-local (off-diagonals) of real dynamic stiffness matrices. Note that $K_{LL} = K_{dyn}^{u,u}$, $K_{RR} = K_{dyn}^{\phi,\phi}$ and $K_{LR} = K_{dyn}^{u,\phi}$

4.2. FREQUENCY-INDEPENDENT MASS, DAMPING AND STIFFNESS FRAMEWORK

The 3D model is developed for calculations in the frequency domain. Consequenctly, the derived soil stiffness is frequency dependent. The extend of this frequency dependency will be addressed in section 4.3. A method is developed in this thesis to translate frequency-dependent complex-valued dynamic soil stiffness of multi-layered heterogeneous soil (S1) to frequency-independent mass, damping and stiffness coefficient matrices. These are required to match the 1D model time-domain formulation. For each element in the complex-valued dynamic stiffness matrices, the complex-valued dynamic stiffness will be approached as frequency-independent spring-mass-dashpot coefficients (K, M & C). In the frequency domain, the dynamic stiffness of each element will be approximated with an impedance function in the form: $-\omega^2 M + i\omega C + K$. This will be elaborated in more detail in section 4.4. If required, higher order terms can be added to the function as a third order viscous damping term and a fourth order stiffness term.

Figure 4.4 gives a visual representation of the ideal frequency-dependent behaviour of the imaginary and real parts of the dynamic stiffness elements to be used in this thesis method. Hereby, M represents the added mass soil mass, K represents the static soil stiffness and C represents the viscous damping of the soil. Please note that there is only a real and imaginary part of the dynamic stiffness in reality. In this work, however, an attempt is made to use polynomial fits to separate the real-valued dynamic stiffness into static (initial) K and added mass M coefficients. This assumption is only valid if the combination of K and $-\omega^2 M$ can accurately represent the real-valued dynamic stiffness over the frequency range of interest. The importance of the mass for engineering practices is discussed in section 4.3.1. Ideally the viscous damping is linear dependent on the excitation frequency and the added mass is a quadratic function of the excitation frequency. The imaginary part of the dynamic stiffness is approximated as ωC. The validity of this assumption is assessed in in section 4.5.

4.3. FREQUENCY DEPENDENCY OF DYNAMIC SOIL STIFFNESS

This section elaborates on the frequency dependency of dynamic soil stiffness for different soil configurations and the two soil vertical boundary conditions of the soil continuum (HS1 and HS2). More details about these boundary conditions is presented in section 3.3.1. It is important to understand how the soil behaves when excited at different loading frequencies, since hydrodynamic and aerodynamic forces will excite the structure at a wide range of frequencies. Figure 4.5 shows typical power spectral densities for wind and waves at offshore sites where OWTs operate. Besides wind and waves, the figure shows the turbine's rotational frequency range (1P) and the blade passing frequency (3P) for multiple operational wind turbines [3]. The peak frequencies of loading of the wind turbines lay close to the loading frequency of turbulent wind and waves. For offshore wind applications the developed 1D model should be able to accurately represent the 3D response

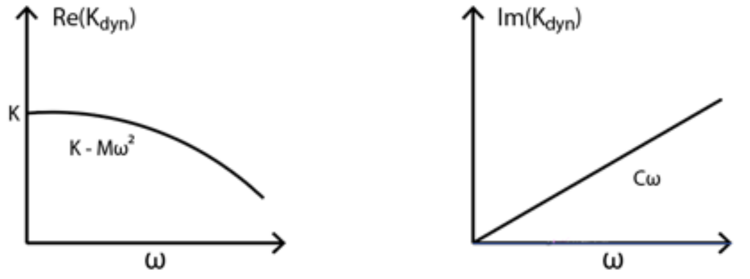

(a) Ideal frequency dependency real dynamic stiffness

(b) Ideal frequency dependency imaginary dynamic stiffness

Figure 4.4: Ideal frequency dependency of real and imaginary pars of dynamic stiffness

of the soil-structure system for frequencies in the operational range around 0.3 Hz. it is also interesting to find out if the method holds for other engineering practices that operate in a higher frequency regime. Consequently, it is important to understand the frequency dependence of dynamic soil stiffness for frequencies above 0.3 Hz.

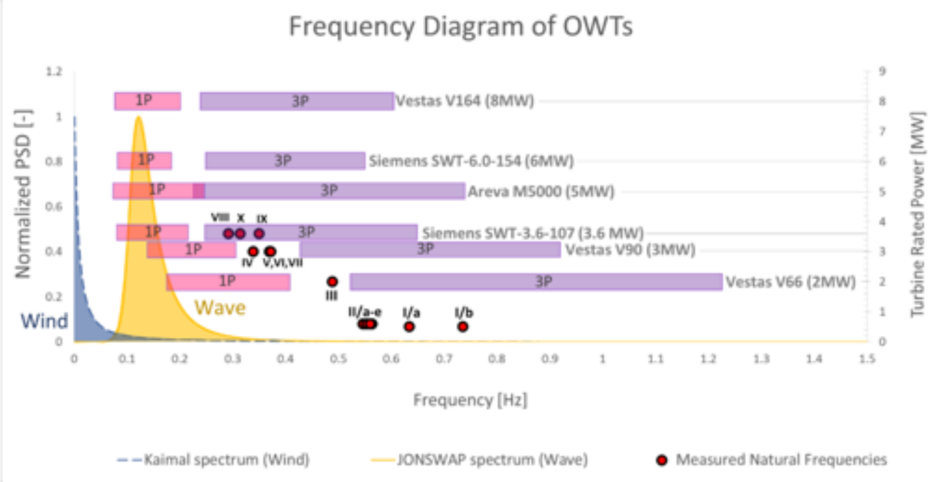

Figure 4.5: Typical wind and wave spectra, rotational speed (1P) and blade passing (3P) frequency bands for six commercial turbines and measured natural frequencies of OWTs [3].

4.3.1. MODEL RESULTS

The 3D model derives four complex-valued dynamic stiffness matrices for each excitation frequency. Herein, the magnitude of the force and the moment of the dynamic excitation are kept constant. The real and imaginary parts of the complex-valued matrices are separated and stored in cell structures (a Matlab object). Each element in the cell contains an array with the magnitudes of the real, or imaginary, dynamic stiffness and excitation frequencies. These arrays can be plotted against frequency to, visually, assess how the dynamic stiffness of different elements is influenced by the excitation frequency. In case of a pile discretization of 41 nodes, the frequency dependency can be assessed for each of the 1,681 elements per matrix.

The performance of representing the dynamic stiffness as frequency-independent mass, damping and stiffness coefficients, depends heavily on the frequency-dependent behaviour of the dynamic soil stiffness. This frequency dependence will mainly be assessed for the diagonals of the various dynamic stiffness matrices, as the diagonals yield the largest contribution to the global stiffness.

Figures 4.6a and 4.6b show the frequency dependence the diagonals of the real and imaginary parts of the dynamic stiffness matrices $K^{u,u}_{dyn}$, $K^{u,\phi}_{dyn}$ & $K^{\phi,\phi}_{dyn}$ from left to right, respectively. This is shown for BC HS1 and heterogeneous soil (S1). The plots are developed by extracting dynamic stiffness from the 3D model for increasing frequencies and by plotting the dynamic stiffness against these frequencies. In each graph 10 lines are shown representing the diagonals (1,1) ... (41,41) in steps of 2 meters along the cavity. The indices (1,1) indicate the diagonal element at the seabed and (41,41) is the diagonal element at the tip of the cavity. Figure 4.6a shows real and imaginary parts of the diagonal elements of the dynamic stiffness against frequency. Figure 4.6b shows the real parts of the dynamic stiffness when the stiffness is normalized by, and subtracted with, the static (initial) stiffness in the top and bottom figures, respectively. The imaginary part of the dynamic stiffness appears to be strongly linear dependent on the excitation frequency, where the real parts seem frequency independent for increasing frequencies. The latter is shown in the second subfigure as, for the lateral and rotational stiffness matrices, the deviation from the static stiffness is smaller than 0.1% for the diagonals. However, the diagonals of the coupling matrices show a higher frequency dependence, with deviations exceeding 30% at an excitation frequency of 1Hz. The last subfigure shows the real part of the dynamic stiffness subtracted with the static stiffness. Visually the graphs show smooth parabolic dependence on the excitation frequency.

The real and imaginary parts of the dynamic stiffness of soil S1 and boundary condition HS2 (bedrock at 100m depth) are presented in figures 4.7a and 4.7b. The figures are computed in the same way as figure 4.6. The effect BC HS2, compared to HS1, on the dynamic stiffness is outlined below:

- There are regions of strong increase in the real part of the dynamic stiffness.
- The real part of the dynamic stiffness is more frequency dependent.
- There are regions of strong increase at 0.75Hz in the real part of the dynamic stiffness (figure 4.7b).

The regions of strong increase in the frequency-dependent part of the real dynamic stiffness appears to be most pronounced at the bottom of the cavity (node 41,41). The question is of these dips are physical or numerical errors related to the 3D model formulation. To answer this question, the frequency-dependent behaviour at the tip of the cavity is analysed in more detail in section 4.3.2 for varying depths of bedrock (BC HS2) and for BC HS1.

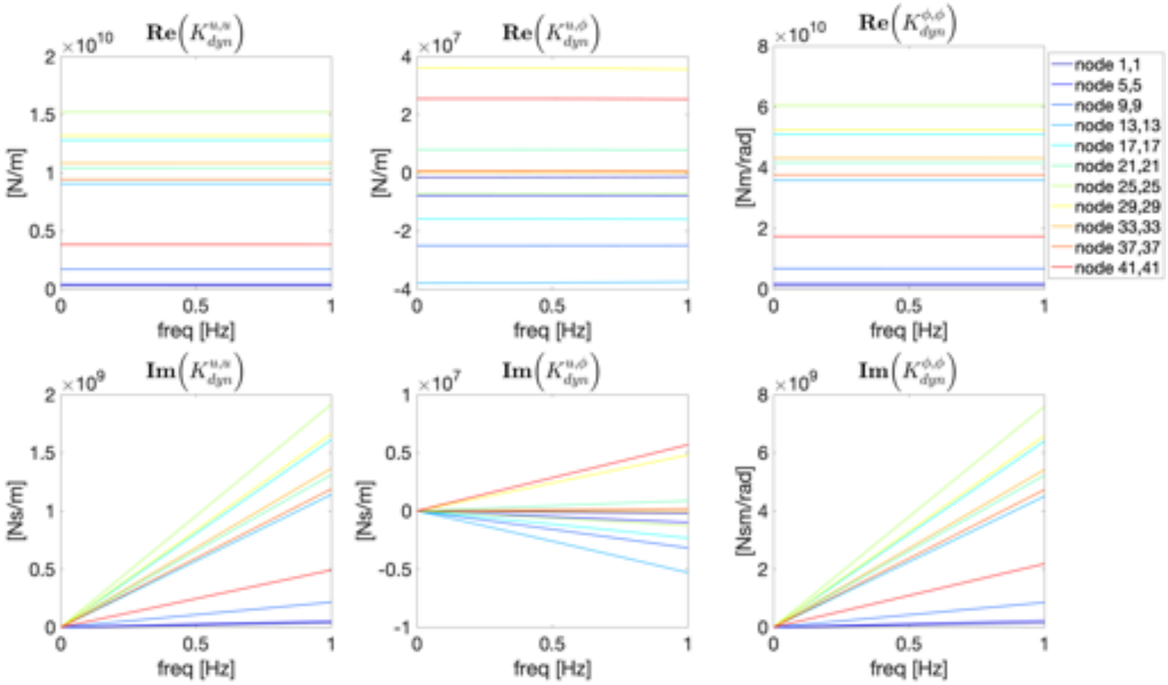

(a) Total real and imaginary parts of the dynamic stiffness over frequency

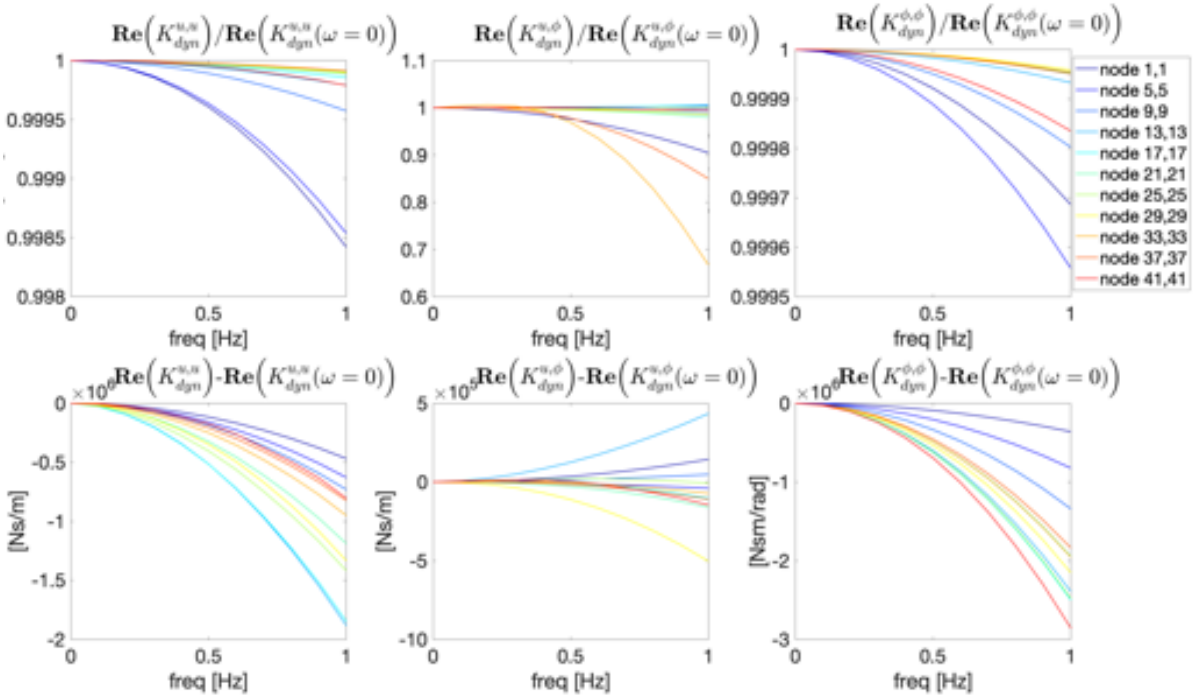

(b) Normalized real parts of the dynamic stiffness over frequency in the top figures and real parts of dynamic stiffness subtracted by static stiffness in the bottom figures.

Figure 4.6: Frequency dependence of dynamic soil stiffness for BC HS1 and soil S1. The magnitudes of nodes on the diagonals are plotted against excitation frequency. Figure 4.6a presents the real and imaginary dynamic stiffness matrices. Figure 4.6b presents the normalized real parts of K_{dyn} in the top figures and the real parts of the dynamic stiffness subtracted with the static stiffness at f=0 Hz in the bottom graphs.

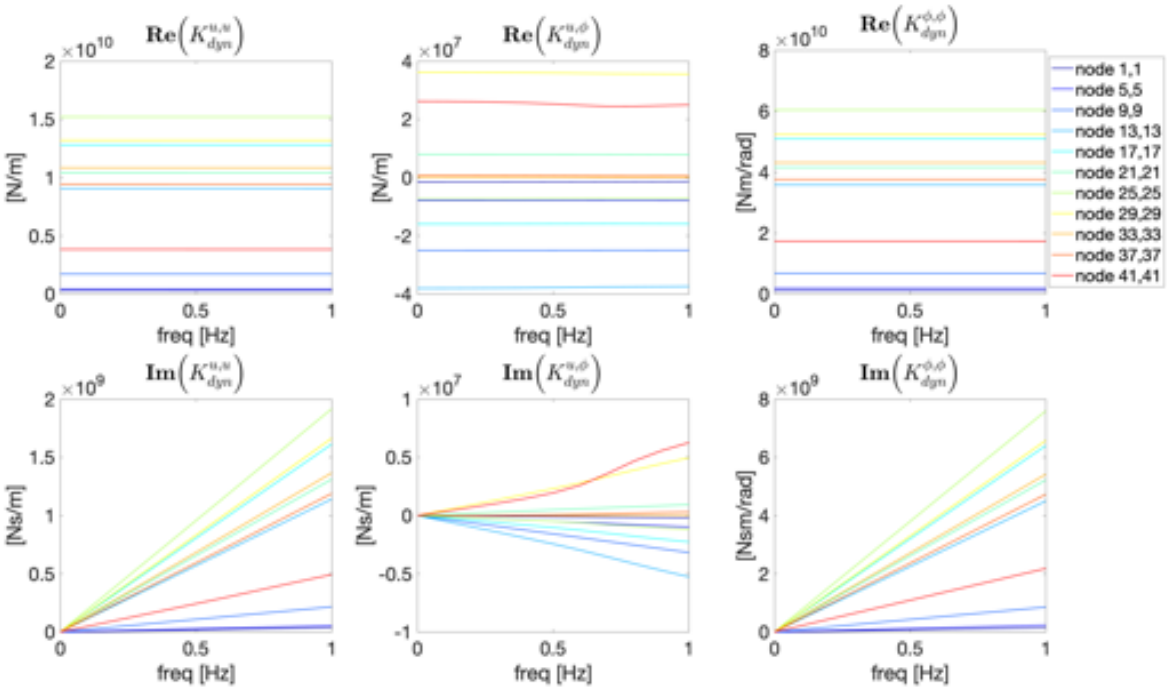

(a) Total real and imaginary parts of the dynamic stiffness over frequency

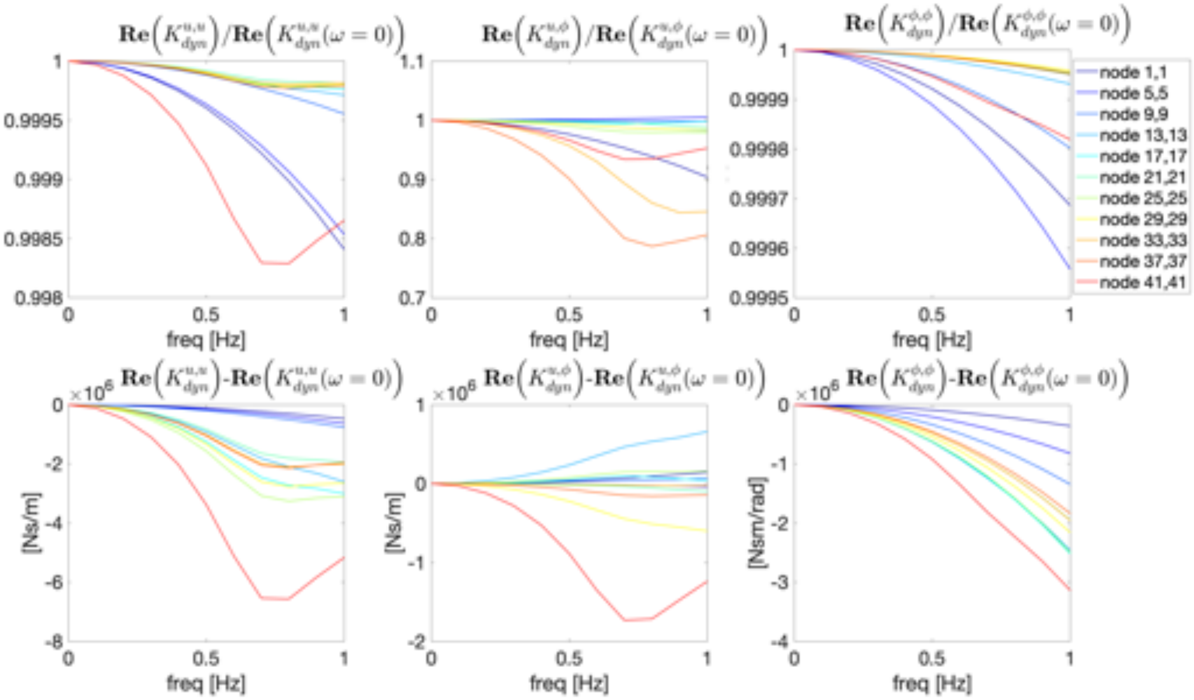

(b) Normalized real parts of the dynamic stiffness over frequency in the top figures and real parts of dynamic stiffness subtracted by static stiffness in the bottom figures.

Figure 4.7: Frequency dependence of dynamic soil stiffness for BC HS2, with bedrock at 100m depth, and soil S1. The magnitudes of nodes on the diagonals are plotted against excitation frequency. Figure 4.7a presents the real and imaginary dynamic stiffness matrices. Figure 4.7b presents the normalized real parts of K_{dyn} in the top figures and the real parts of the dynamic stiffness subtracted with the static stiffness at f=0 Hz in the bottom graphs.

4.3.2. RESONANCE EFFECTS ASSOCIATED WITH 3D MODEL SETUP

Figure 4.8 presents the total real part of the dynamic stiffness of the lower most diagonal node of $K^{u,u}_{dyn}(41,41)$ for BCs HS1 and HS2, with a bedrock at 50m, 100m and 200m and soil S1. The blue line represents in the real part of the dynamic stiffness for BC HS1. The red, yellow and purple lines represent the total real part of the dynamic stiffness for BC HS2 (bedrock at 50m, 100m and 200m). The bottom diagonal node is presented as regions of strong increase are most pronounced at that location in the matrix. The regions of increase are also present in higher soil layers with a similar frequency dependence but with lower magnitudes. This indicates that it is a characteristic for the total system.

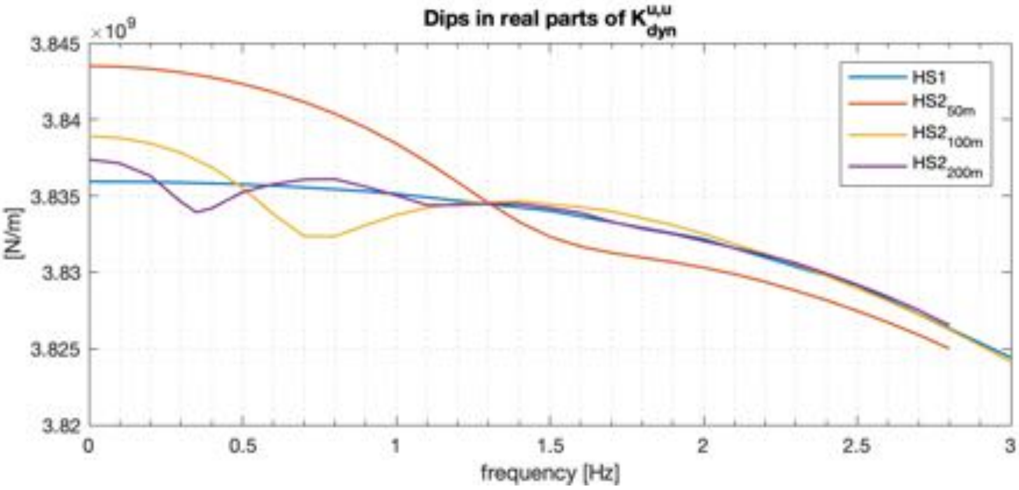

Figure 4.8: Total real part of dynamic stiffness of lowest diagonal node ($K^{u,u}_{41,41}$) for BCs HS1 and HS2 with bedrocks at different depths,

In deriving the figure above, all model input is kept constant with exception of the depth at which the stiff half-space begins. In case of BC HS1, there is no stiff half-space and the waves are damped in horizontal and vertical directions, hence the smooth descending regions of strong increase. As mentioned in section 3.3.1, horizontal reflections of waves are prevented for both BCs HS1 and HS2 in the 3D model. The depth of the rigid layer is the only parameter that varies. The regions of strong increase in the real part of the dynamic stiffness are necessarily caused by this depth. To provide judgment on these numerical results, literature is consulted in search of similar results and to find an analytic explanation of these effects. It is expected that the regions of strong increase are caused by global resonances and a result of waves reflecting on the bedrock.

In the work of Gazetas et al. [35] and Novak et al. [14], the interaction between soil and an elastic horizontally vibrating pile is theoretically examined. Herein the soil is modelled as a linear, viscoelastic layer, overlaying rigid bedrock. Both researches identify similar dips in the frequency-dependent behaviour of dynamic stiffness in soil overlaying a rigid layer at some depth. "The dip occurs at the fundamental frequency, f_n, of the soil stratum for vertical shear wave propagation" [35]. Analytic expressions that explain the dips in dynamic stiffness are found in the work of Hamdan [30] for both homogeneous and heterogeneous soil layers. For an homogeneous soil layer of depth H and shear wave velocity C_s, the value of f_n can be calculated by equation (4.1). In case of heterogeneous soil stratigraphy(S1), the effective shear wave velocity can be calculated by taking the sum of the shear wave velocity over all vertically-spaced soil layers $j = 1,2,3,...,m$ (eq. (4.2)) and substitution in equation (4.1).

$$f^h_n = (2n-1)\frac{C_s}{4H}, \qquad n = 1,2,3,... \tag{4.1}$$

$$C_{s,sum} = \sum_{j=1}^{m} \frac{C_{s,j} d_j}{H}, \qquad j = 1,2,3,...,m \tag{4.2}$$

These equations are successfully able to predict the dips in figure 4.8. This proves that the dips are a result of the model setup rather than numerical errors. For example, at a depth of 200m and S1 soil conditions, the first and second resonance frequencies are 0.365 Hz and 1.10 Hz. Figure 4.9 presents the real-valued and complex-valued lateral dynamic stiffness of the bottom diagonal element for two cases; absence of material damping and for a soil damping ratio of 2%. The predicted resonance frequencies match the dips in the figure. The sharp increase of stiffness after the resonance frequency is accompanied by an increase in damping. In absence of material damping, the increases are clearly visible in figure 4.9. In absence of material damping and below the first resonance frequency, which is also the cut-off frequency for guided wave propagating horizontally, there is no horizontally propagating wave carrying away energy from the loading and thus no radiation (geometric) damping [36]. However, the increases in damping only contribute marginally to the total damping when frequency-dependent material damping is introduced. This is shown by the much steeper orange line.

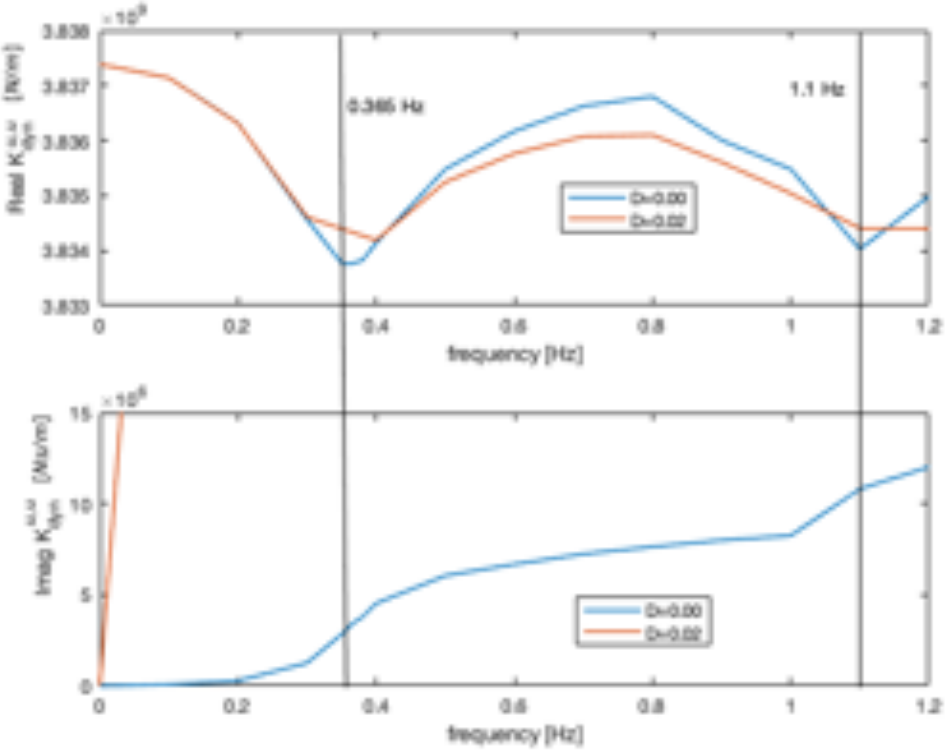

Figure 4.9: Dynamic stiffness of diagonal $K_{dyn}^{u,u}$ at bottom of cavity for a soil depth of 200m and different material damping ratio's (0% and 2%)

4.3.3. FREQUENCY DEPENDENCE OF NON-LOCAL IMAGINARY PARTS OF THE LATERAL DYNAMIC SOIL STIFFNESS

In the bottom right graph of figure 4.1a in section 4.1, two lines are observed that run (almost) parallel to the main diagonal. These lines indicate the minimum values in the imaginary lateral dynamic stiffness matrix, or $\mathrm{Im}(K_{dyn}^{u,u})$. Figure 4.10 shows how the matrix changes for increasing excitation frequencies. The absolute values of the imaginary lateral dynamic stiffness are presented on a logarithmic scale.

That sharp minima are present over the entire frequency range of 0.1 to 0.5 Hz (=0.63 to 3.14 rad/s) for BC HS1 and are observable for frequencies above 0.3 Hz for BC HS2 with bedrock at 200m. The latter is close to cut-off frequency (0.365 Hz) of the system with a bedrock at 200m depth. The minima move towards the main diagonal for increasing frequencies. A function is developed to plot the magnitude of a single column of $Im(K_{dyn}^{u,u})$ on a logarithmic scale. Additionally, a sign function (also referred to as signum function) is added to the equation to get the correct signs. The function is presented below:

$$\mathrm{sgn}\left(\mathrm{Im}\left(K_{dyn_i}^{u,u}(f)\right)\right)\log\left(\left|\mathrm{Im}\left(K_{dyn_i}^{u,u}(f)\right)\right|\right) \tag{4.3}$$

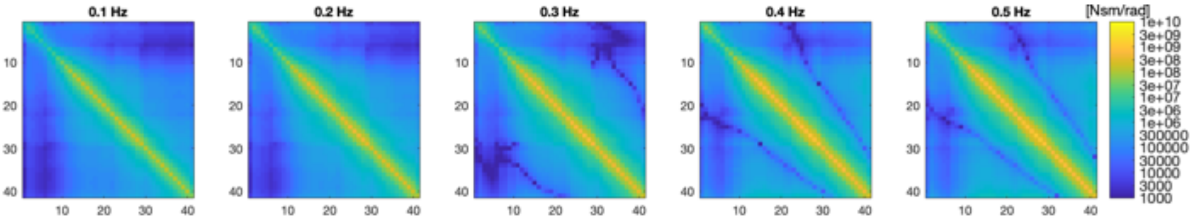

(a) Imaginary parts of lateral dynamic stiffness for BC HS1 and soil S1 for excitation frequencies 0.1–0.5 Hz

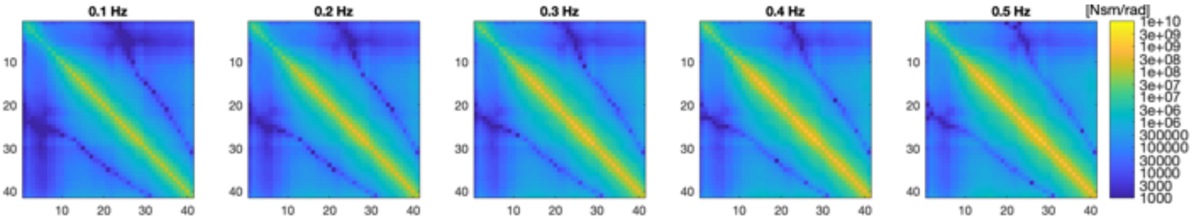

(b) Imaginary parts of lateral dynamic stiffness $\text{Im}(K_{dyn}^{u,u})$ for BC HS2, bedrock at 200m, and soil S1 for the excitation frequencies 0.1–0.5 Hz.

Figure 4.10: Envelopment of imaginary lateral dynamic stiffness matrices against increasing excitation frequencies. BC HS1 is presented in 4.10a and BC HS2, bedrock at 200m, in figure 4.10b. Note that the label on the x-/ and y-axis should be node [-].

Figures 4.11a and 4.11b present the results of equation (4.3) a single column (column 25) of the imaginary lateral dynamic stiffness matrix $\text{Im}(K_{dyn}^{u,u})$ for the frequency range 0.1 to 0.4 Hz (ω= 0.63 to 2.51 rad/s) on a logarithmic scale. The imaginary non-local lateral stiffness experiences a sign change some distance away from the diagonal. This phenomena is present for all considered frequencies when boundary conditions HS1 is applied. For BC HS2, the sign change happens at excitation frequencies above the cut-off frequency. The strong increases in imaginary stiffness, that is likely a result of resonance in the soil layers, cause the negative-valued non-local imaginary stiffness to become positive.

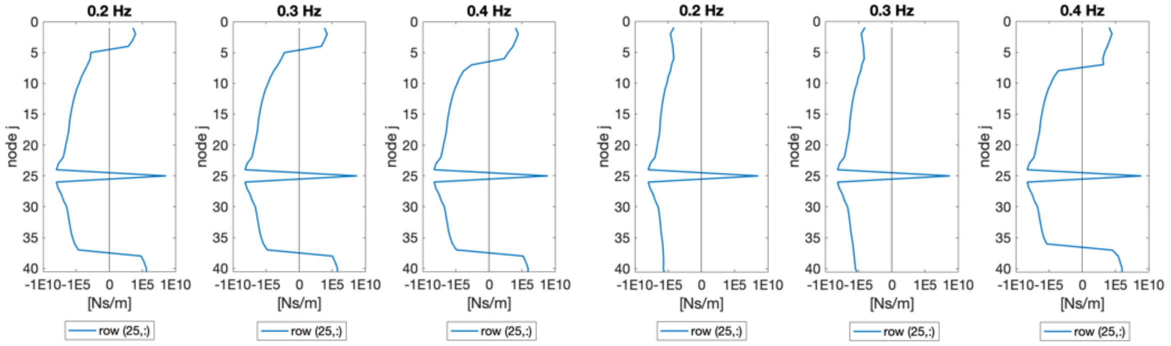

(a) Equation 4.3 is applied to draw the values of column 25 of $\text{Im}(K_{dyn}^{u,u})$ on a logarithmic scale.

(b) Equation 4.3 is applied to draw the values of column 25 of $\text{Im}(K_{dyn}^{u,u})$ on a logarithmic scale.

Figure 4.11: A single coluimn of the imaginary-valued lateral dynamic stiffness matrix for increasing frequencies. Soil stratigraphy S1 is applied. Figure a) and b) show this respectively for BC HS1 and BC HS2 (200m).

The phase angle between the real and imaginary lateral response is calculated by the four-quadrant inverse tangent method (equation (4.4)). The inverse of the matrices is calculated to obtain flexibility matrices (or, equivalently, the matrices that represent the real-valued and imaginary-valued displacements).

$$\psi(i,j) = \text{atan2}\left(\left(\text{Im}\left(K_{dyn}^{u,u}(f)\right)\right)^{-1}, \text{Re}\left(\left(K_{dyn}^{u,u}(f)\right)\right)^{-1}\right) \tag{4.4}$$

Figures 4.12a and 4.12b present the phase between real and imaginary lateral displacements.The real and imaginary displacements are in-phase with each other on, and near, the diagonal. A phase difference is introduced at the non-local elements near the minima lines. After the minima lines, the complex-valued displacements can even be in antiphase with each other; the phase difference is 180 degrees (π radians). The imaginary part of the lateral dynamic stiffness changes sign after significant change in the phase angle. The out-of-phase domain grows for increasing frequencies and is, in case of BC HS2, triggered by the cut-off frequency. The non-local elements in the imaginary-valued flexibility matrix can approach zero or can even become negative. The complex-valued response is then in antiphase. The non-local elements of the imaginary stiffness are less monotonic linear frequency dependent than expected. This indicates that material damping is less radiation damping becomes more important at non-local eleemnt

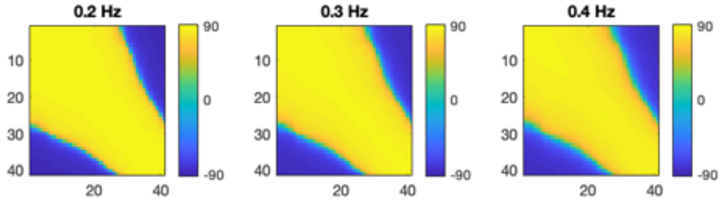

(a) HS1

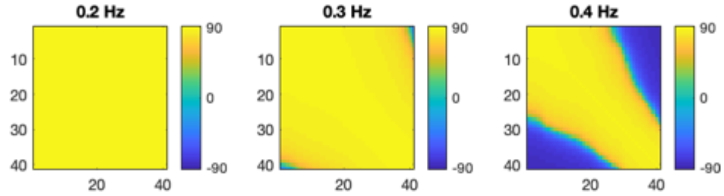

(b) HS2

Figure 4.12: Phase angle between the real and imaginary lateral displacement matrices

4.3.4. CONCLUSIONS AND DISCUSSION

Section 4.3.1 focused on the frequency-dependent behaviour of dynamic soil stiffness in a realistic heterogeneous soil stratigraphy (S1). The diagonals (local elements) and near diagonals (non-local elements) of the dynamic stiffness matrices contribute most to the global dynamic stiffness of the medium. The magnitude of the non-local (off-diagonals) dynamic stiffness decreases rapidly when calculated some distance away from the point of excitation.

For both BCs HS1 and HS2, the imaginary parts of the dynamic stiffness show strong linear dependence on the excitation frequency. The frequency-dependent part of the real dynamic stiffness is very small compared to the initial (static) stiffness ($K_{dyn}(\omega) - K_{dyn}(\omega = 0) << K_{dyn}(\omega = 0)$) in the frequency range 0 to 3 Hz. For case HS1, no bedrock, the real part of total dynamic stiffness shows quadratic frequency dependence on the excitation frequency. For BC HS2, the presence of a bedrock results in small resonances in the real parts of elements in the dynamic stiffness matrices. These resonances are caused by reflections of shear waves on the stiff soil layer. The location of the dips can accurately be predicted by equation (4.1). At the resonance frequencies, the imaginary part of the dynamic stiffness shows slight increases in magnitude.

The remaining question is how important the frequency dependence of the real part is. For the imaginary part of the dynamic stiffness it is obvious that is has to be taken into account in the proceedings of this thesis. In the frequency range of 0 – 0.3 Hz, it is expected that for the real part the following approximation holds: $K_{dyn} \approx K_{static}$. This question will be covered in more detail in section 4.4.

4.4. FOUNDATION IMPEDANCE

This section describes the method of extraction of the frequency-dependent dynamic stiffness into spring-mass-damper coefficients.

If the system is excited with a complex-valued force $F(t) = F_0 e^{i\omega t}$ with amplitude F_0, the equation of motion becomes:

$$m\ddot{x} + c\dot{x} + k = F(t) \tag{4.5}$$

Substituting the particular solution $x(t) = x_0 e^{i\omega t}$ into eq. (4.5) yields:

$$(k-\omega^2 m) + i\omega c = \frac{F(t)}{x(t} = \widetilde{K}_{dyn} \tag{4.6}$$

Where $\widetilde{K}_{dyn}$ is the complex-valued dynamic soil stiffness. As presented in section 4.3.1. the dynamic stiffness can be separated into a real and imaginary component:

$$\widetilde{K}_{dyn} = \mathrm{Re}(K_{dyn}(\omega)) + i\mathrm{Im}(K_{dyn}(\omega)) \tag{4.7}$$

Representing the real and imaginary dynamic stiffness as frequency-dependent stiffness, mass and damping coefficients for each element in the dynamic stiffness matrices yields:

$$-\omega^2 M_{i,j}^{ii,jj} + K_{i,j}^{ii,jj} = Re\left(K_{dyn(i,j)}^{ii,jj}\right) \qquad i,j = 1,2,...,41 \qquad ii,jj = u,\phi \tag{4.8}$$

$$i\omega C_{i,j}^{ii,jj} = Im\left(K_{dyn(i,j)}^{ii,jj}\right) \qquad i,j = 1,2,...,41 \qquad ii,jj = u,\phi \tag{4.9}$$

The combination of the estimated coefficients should be able to correctly capture the dynamic stiffness for the frequency range of interest. The presence of bedrock affects the frequency range for which the equations are able to predict the dynamic stiffness. Since the real part of the dynamic stiffness will be approximated by a static stiffness term and a parabolic frequency-dependent term, this method is only valid for frequencies up to the first resonance dip (see figure 4.8). For BC HS1, the method is applicable for a wider frequency range due to the absence of observable soil resonances.

For each node in the four complex-valued dynamic stiffness matrices, a polynomial fit is performed in Matlab to approximate frequency-independent stiffness, damping and mass coefficients. The real part of the dynamic stiffness is approximated as $K_{i,j} - \omega^2 M_{i,i}$ and the imaginary parts as $C_{i,j}\omega$, with M, K and C being the frequency-independent coefficient matrices.

Some small modifications are applied to reduce the number of polynomials in the $polyfit$ function of Matlab. For every element of the real dynamic stiffness matrix, the real part of the dynamic stiffness will be approximated with a 2^{nd} degree polynomial, resulting in three coefficients; constant, 1st and 2nd degree. However, only the constant and quadratic (2^{nd} degree) are used to approximate the stiffness and mass. The static stiffness (K) is taken as the initial real dynamic stiffness at 0 Hz. The 2nd degree term is found by performing a 1st degree polynomial fit for real $K_{dyn} - K_{st}$ over the angular frequency squared (ω^2). The polynomial fit over angular frequency squared is taken to increase to neglect the first degree term (more weight on the 2nd degree term).The resulting 2nd degree coefficient yields the frequency-independent mass coefficient (M). The frequency-independent damping coefficients are found by taking the tangent of the imaginary dynamic stiffness between 0 and 0.3 Hz. For the offshore wind industry, the common frequency range of interest is 0 – 0.3 Hz. Therefore, the polynomial fits are estimated for that range. 12 filled matrices are created, containing all frequency-independent stiffness, mass and damping coefficients to approximate the complex-valued lateral, rotational and coupling dynamic stiffness matrices.
12 coefficient matrices are thus created:

$$\begin{array}{llllll} M^{u,u}, & C^{u,u} & K^{u,u} & M^{\phi,\phi}, & C^{\phi,\phi} & K^{\phi,\phi} \\ M^{u,\phi}, & C^{u,\phi} & K^{u,\phi} & M^{\phi,u}, & C^{\phi,u} & K^{\phi,u} \end{array}$$

The primary matrices (u,u) and (ϕ,ϕ) are symmetric over the diagonal. The coupling matrices (u,ϕ) and (ϕ,u) are asymmetric. They yield the following relation: $X_{i,j}^{u,\phi} = X_{j,i}^{\phi,u}$ for $X = M, C$ & K.

4.5. EVALUATION OF RESULTS AND COMPARISON WITH 3D MODEL RESULTS

In this section, the performance of the impedance coefficients in representing the complex-valued dynamic stiffness as calculated by the 3D model, is evaluated. Figures 4.13 and 4.14 present the fit between the real and imaginary parts of the dynamic stiffness (black), as calculated by the 3D model, and the approximated frequency-independent mass and damping coefficients (red), as estimated using polynomial fits. This is shown for the diagonals for the frequency range 0 – 0.5 Hz. The lines are to closely spaced to add labels to the individual lines. For the diagonals of the matrices it is found that the coefficients are able to accurately mimic the dynamic soil stiffness. The top three graphs of the sub-figures show the frequency-dependent part of the real dynamic stiffness (static stiffness subtracted). The approximation with BC S2 (bedrock at 50m) shows slightly smaller misfits than for BC HS1 (no bedrock), as some small deviations between the frequency dependent part of the real-valued dynamic stiffness and approximated mass are observed in the top three graphs of figure 4.13. These are however marginal and are not expected to have a significant effect the global system response. Please note that there are no resonances present in figure 4.14. The reason is that the frequency range of 0 to 0.5 Hz is outside of the resonant regime for BC HS2 with a bedrock at 50m. At frequencies above the first soil resonance frequency of 1.5Hz, the approximated mass is no longer capable of representing the frequency-dependent part of the real-valued dynamic stiffness.

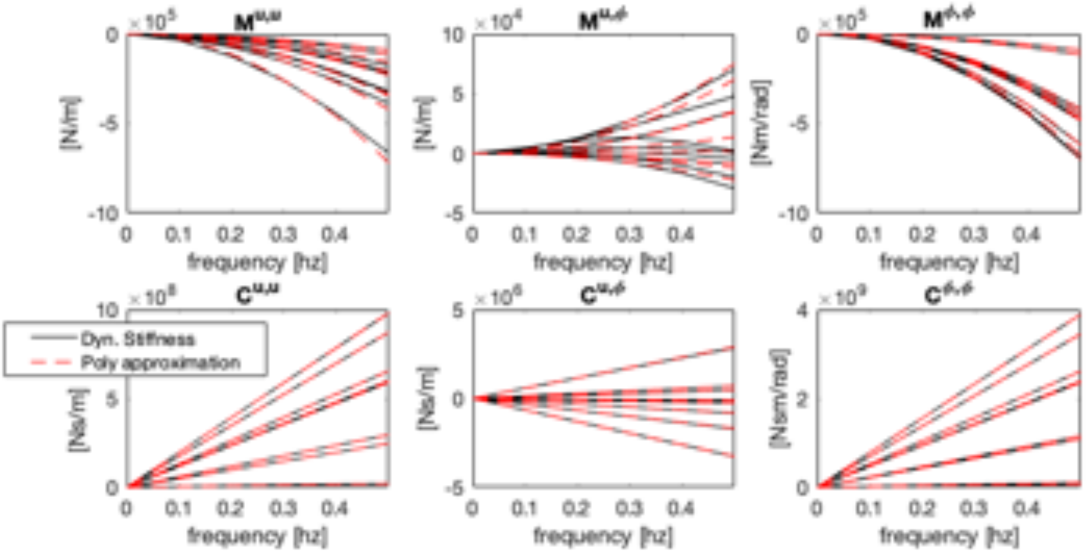

Figure 4.13: For BC HS1, the fits between diagonals of frequency-dependent parts of the dynamic stiffness matrices and approximations with polynomial coefficients. The black lines represent the real dynamic stiffness and the red dotted lines represent the approximated dynamic stiffness using approximated coefficients.

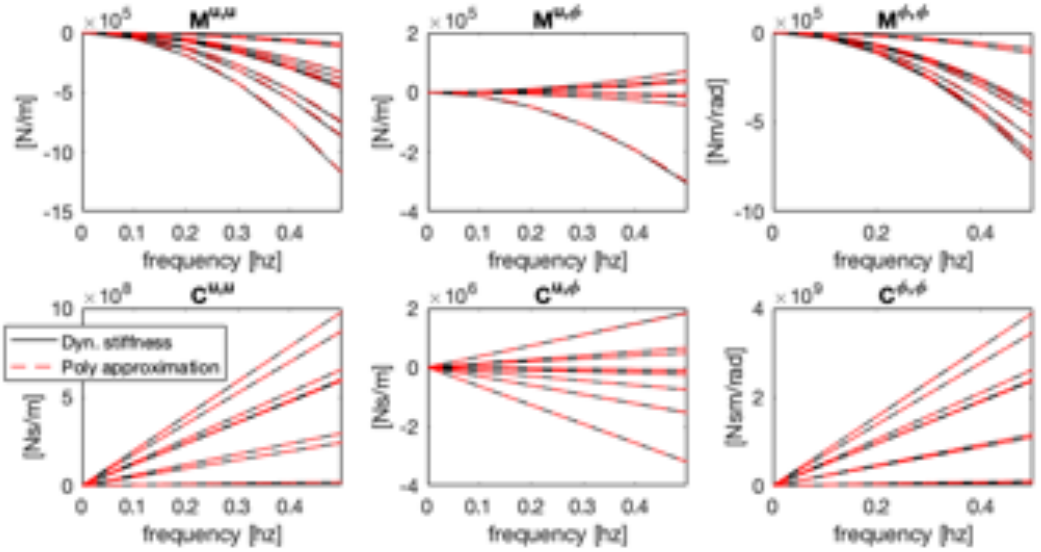

Figure 4.14: For BC HS2: bedrock at 50m. Fits between diagonals of the frequency-dependent parts of the dynamic stiffness matrices and approximations with polynomial coefficients. The black lines represent the real dynamic stiffness and the red dotted lines represent the approximated dynamic stiffness using approximated coefficients.

In total 13,448 polynomial fits are performed to approximate the frequency-dependent components of the dynamic stiffness matrices. For brevity, not all plots of components of the matrices are presented in this thesis.

To measure the performance of the method, and to evaluate the local and non-local misfit between approximated impedance coefficients and the dynamic stiffness on element level, a cost function is developed in the form:

$$\text{Local real misfit} = \sum_{\omega=0}^{\omega=0.5\cdot 2\pi} \frac{\left|\mathrm{Re}\left(K^{ii,jj}_{dyn_{i,j}}(\omega) - K^{ii,jj}_{dyn_{i,j}}(\omega=0)\right) - \left(-\omega^2 M^{ii,jj}_{i,j}\right)\right|}{\left|\mathrm{Re}\left(K^{ii,jj}_{dyn_{i,j}}(\omega)\right) - K^{ii,jj}_{dyn_{i,j}}(\omega=0)\right|} \tag{4.10}$$

$$\text{Local imaginary misfit} = \sum_{\omega=0}^{\omega=0.5\cdot 2\pi} \frac{\left|\mathrm{Im}\left(K^{ii,jj}_{dyn_{i,j}}(\omega)\right) - \left(\omega C^{ii,jj}_{i,j}\right)\right|}{\left|\mathrm{Im}\left(K^{ii,jj}_{dyn_{i,j}}(\omega)\right)\right|} \tag{4.11}$$

for $ii, jj = u, \phi$ and $i, j = 1:41$. K_0 is the static stiffness, i.e. the dynamic stiffness at zero Hertz.

Note that the static stiffness (K) is not analysed because there is a perfect match. The frequency range 0–0.5 Hz (ω=0–3.14[rad/s]) is chosen so that it captures at least the frequency range of interest for offshore wind. The sum of the misfits is taken over the frequency range, resulting in a cost function over a frequency range instead of the misfit for a single frequency. During the computations some elements show high local misfits between the polynomial approximations and the dynamic stiffness. The question is how large the contribution of these misfits is to the total system error. Therefore, besides the local misfit ratio, also the ratio of local misfit over total system misfit is taken into account for each matrix. The latter is the sum of misfits over all elements in a matrix. If the misfit ratio is high, but the absolute magnitude of the misfit is low, the contribution to the total system error can still be low. On the other hand, a small misfit ratio with a large absolute misfit can have a large contribution to the total system error. Therefore, the following relation is also taken into account:

$$Dreal^{ii,jj}_{i,j} = \frac{\sum_{\omega=0}^{\omega=0.5\cdot 2\pi}\left|\mathrm{Re}\left(K^{ii,jj}_{dyn(i,j)}(\omega) - K^{ii,jj}_{0(i,j)}\right) - \left(-\omega^2 M^{ii,jj}_{i,j}\right)\right|}{\sum_{i,j}^{i,j}\sum_{\omega=0}^{\omega=0.5\cdot 2\pi}\left|\mathrm{Re}\left(K^{ii,jj}_{dyn(i,j)}(\omega) - K^{ii,jj}_{0(i,j)}\right) - \left(-\omega^2 M^{ii,jj}_{i,j}\right)\right|} \tag{4.12}$$

$$Dimag^{ii,jj}_{i,j} = \frac{\sum_{\omega=0}^{\omega=0.5\cdot 2\pi}\left|\mathrm{Im}\left(K^{ii,jj}_{dyn(i,j)}(\omega)\right) - \left(\omega C^{ii,jj}_{i,j}\right)\right|}{\sum_{i,j}^{i,j}\sum_{\omega=0}^{\omega=0.5\cdot 2\pi}\left|\mathrm{Im}\left(K^{ii,jj}_{dyn(i,j)}(\omega)\right) - \left(\omega C^{ii,jj}_{i,j}\right)\right|} \tag{4.13}$$

for $ii, jj = u, \phi$ and $i, j = 1:41$.

The results are presented in a condense form in figure 4.15. The left hand side figures present the summed magnitude of the frequency-dependent dynamic stiffness over the aforementioned frequency range. The figures in the middle show the local contribution of the misfit to the total misfit (eq. (4.12) – (4.13)). Finally, the third column presents the local misfit ratio as calculated by equations (4.10) – (4.11). Looking into the right-hand-side figures, the frequency-dependent parts of the dynamic stiffness behave less monotonic than expected. High misfits are measured at off-diagonals and are most profound with outliers exceeding 20% at the boundaries of the lateral and rotational stiffness matrices. For the imaginary parts, the fit between the dynamic stiffness and approximation damping coefficients yields shows accurate results with some outliers. The scaled magnitude of the misfit over the total misfit shows contradictory results with the largest (in magnitude) misfits concentrating in the middle and near the diagonals. This could indicate that high misfits near the boundaries might not present significant problems when looking at the matrix as a whole. A high misfit ratio means that the dynamic stiffness cannot be approximated with a single coefficient multiplied by ω^2 for the frequency-dependent real parts and ω for the imaginary parts. The total misfits for the frequency range 0–0.5 Hz is presented in table 4.1

Table 4.1: Total misfits for the mass and damping matrices as calculated by taking the sum over all local misfits.

Matrix	$M^{u,u}$	$M^{u,\phi}$	$M^{\phi,\phi}$	$C^{u,u}$	$C^{u,\phi}$	$C^{\phi,\phi}$
Misfit HS1	$0.68\cdot 10^{-1}$	0.124	$0.350\cdot 10^{-2}$	$0.115\cdot 10^{-3}$	$0.893\cdot 10^{-3}$	$0.330\cdot 10^{-5}$
Misfit HS2$_{50m}$	$0.66\cdot 10^{-2}$	$0.959\cdot 10^{-2}$	$0.207\cdot 10^{-2}$	$0.298\cdot 10^{-3}$	$0.665\cdot 10^{-3}$	$0.108\cdot 10^{-5}$

The left hand side figures in figure 4.15 could explain the larger misfits near the center of the matrices as the figures show patterns that are comparable with the middle column. Apparently, the contribution of the local misfit to the total misfit is strongly dependent on the magnitude of the frequency-dependent parts of the real and imaginary dynamic stiffness. Another observation is that the local contribution to the total misfit at the top and left parts of the figures in the middle figures is small. An explanation can be found in figure 3.4. This figure presented the soil stratigraphies used in this thesis. For the heterogeneous soil stratigraphy, that is currently adapted, the top layers of the soil are relatively soft, while the middle and bottom layers are relatively stiff. A correlation is bound between the magnitude of misfits and stiff soil layers. This is considered no surprise as a small percentage deviation of a large magnitude can yield a large absolute misfit.

Figure 4.15 indicated where the largest misfits concentrate in the matrices. It is, however, challenging to give convincing conclusions. Even if the local misfit ratio is very high, the effects to the global system response can be minor. Therefore, even if undesired, a large misfit ratio might not cause problems. The largest misfits, in terms of magnitude, accumulate at the stiff soil layers. At these locations, the local misfit ratio is low, meaning an accurate match between the approximated impedance coefficients and the frequency-dependent dynamic stiffness at the most important elements. For BC HS2, the presence of bedrock at 50m, the results are comparable with the results presented in figure 4.15. In terms of $M_{i,j}^{u,u}$ the match between impedance and dynamic stiffness is better for BC HS2 than HS1. This means that the frequency dependence of the real stiffness, in case of the presence of bedrock, is a more monotonic parabolic function of frequency. The latter is at least valid for frequencies below the first soil resonance frequency. This was unexpected as HS1 yields a numerical system without soil resonances. The larger misfits related to BC HS1 are expected to be related to the PML formulation. However, redefining the PMLs is outside of the scope of this research. The results for BC HS2 are presented in figure 4.16.

In addition, the effect diameter on the fit between the estimated coefficients and the 3D model calculated dynamic stiffness is examined for HS1. The procedure is the same as presented above. Only the diameter of the cavity, or ring of nodes, is varied. The diameters that are examined are 3m, 5m (reference) and 7m. The total misfits between the matrices are presented in table 4.2. The matrix figures can be found in appendix B. The misfits between the coefficient matrices and the dynamic stiffness, as calculated by the 3D model, are in the same order of magnitude for larger or smaller diameters. A larger diameter yields slight improvements in misfit between the mass matrices and a slightly lesser fit for the damping matrices. The results are very close to each other. Therefore, can be concluded that the polynomial estimations performance is independent of the diameter of the ring of nodes (cavity).

Table 4.2: Total misfits for the mass and damping matrices as calculated by taking the sum over all local misfits for different L/D's. L/D=4 is reference case.

Matrix	$M^{u,u}$	$M^{u,\phi}$	$M^{\phi,\phi}$	$C^{u,u}$	$C^{u,\phi}$	$C^{\phi,\phi}$
Misfit D=3m	0.071	0.130	$0.330 \cdot 10^{-2}$	$0.720 \cdot 10^{-3}$	$0.260 \cdot 10^{-2}$	$0.118 \cdot 10^{-4}$
Misfit D=5m (reference)	0.068	0.124	$0.350 \cdot 10^{-2}$	$0.115 \cdot 10^{-3}$	$0.893 \cdot 10^{-3}$	$0.330 \cdot 10^{-5}$
Misfit D=7m	0.061	0.123	$0.340 \cdot 10^{-2}$	$0.512 \cdot 10^{-3}$	$0.660 \cdot 10^{-2}$	$0.247 \cdot 10^{-4}$

Appendix B gives more examples of the fit between complex-valued dynamic stiffness and approximated mass and damping on element level. How well the coefficients are able to predict the global soil-structure response will be discussed in section 5.3.

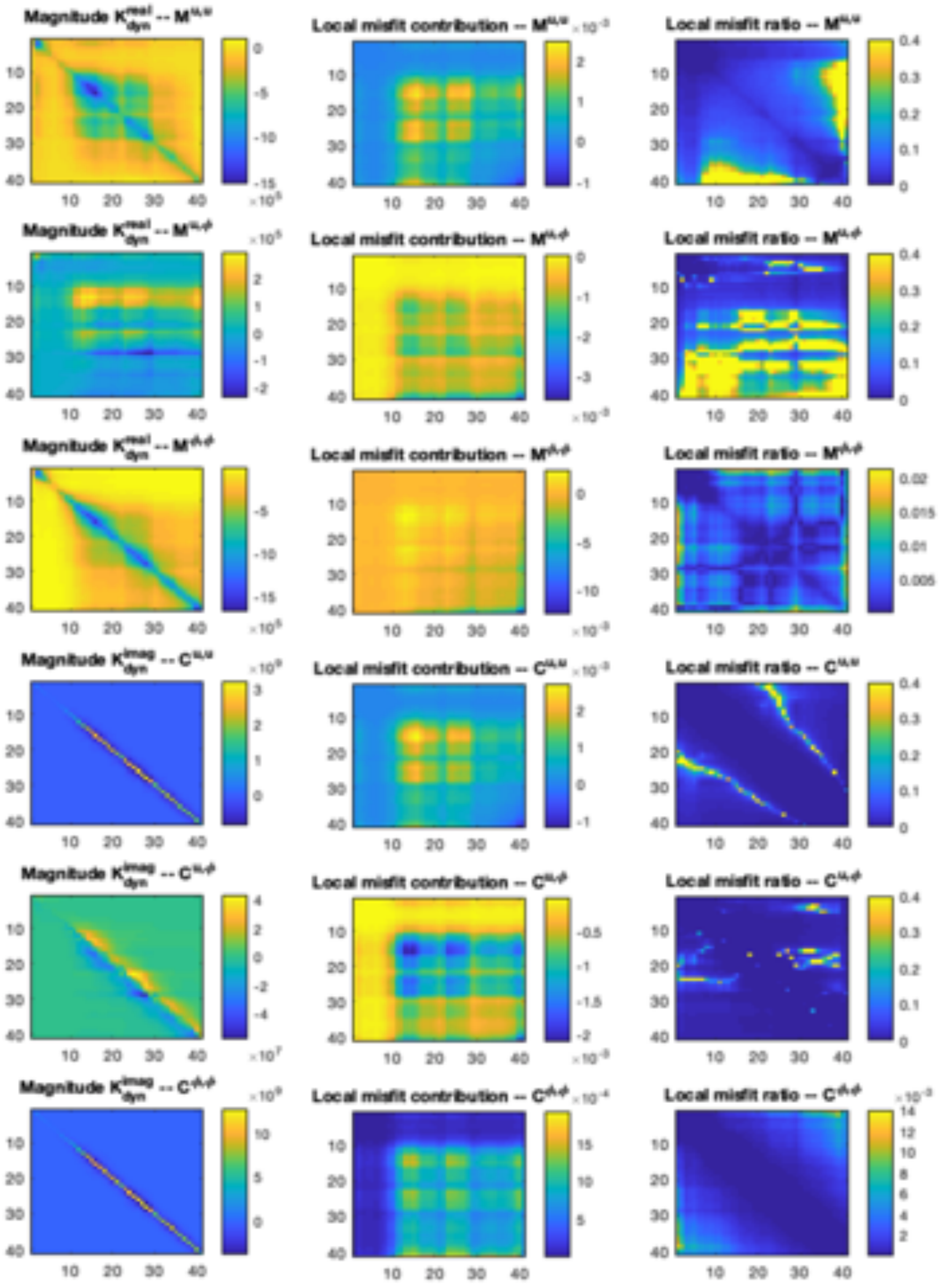

Figure 4.15: BC HS1. Visual representation of misfits for mass and damping matrices. The left column shows the summed magnitude over frequency for the elements in the dynamic stiffness matrices. The middle column presents the contribution of local misfit to the total misfit (eq: (4.10)–(4.11)). In the last column the local ratio is presented as calculated by eq. (4.10)–(4.11)

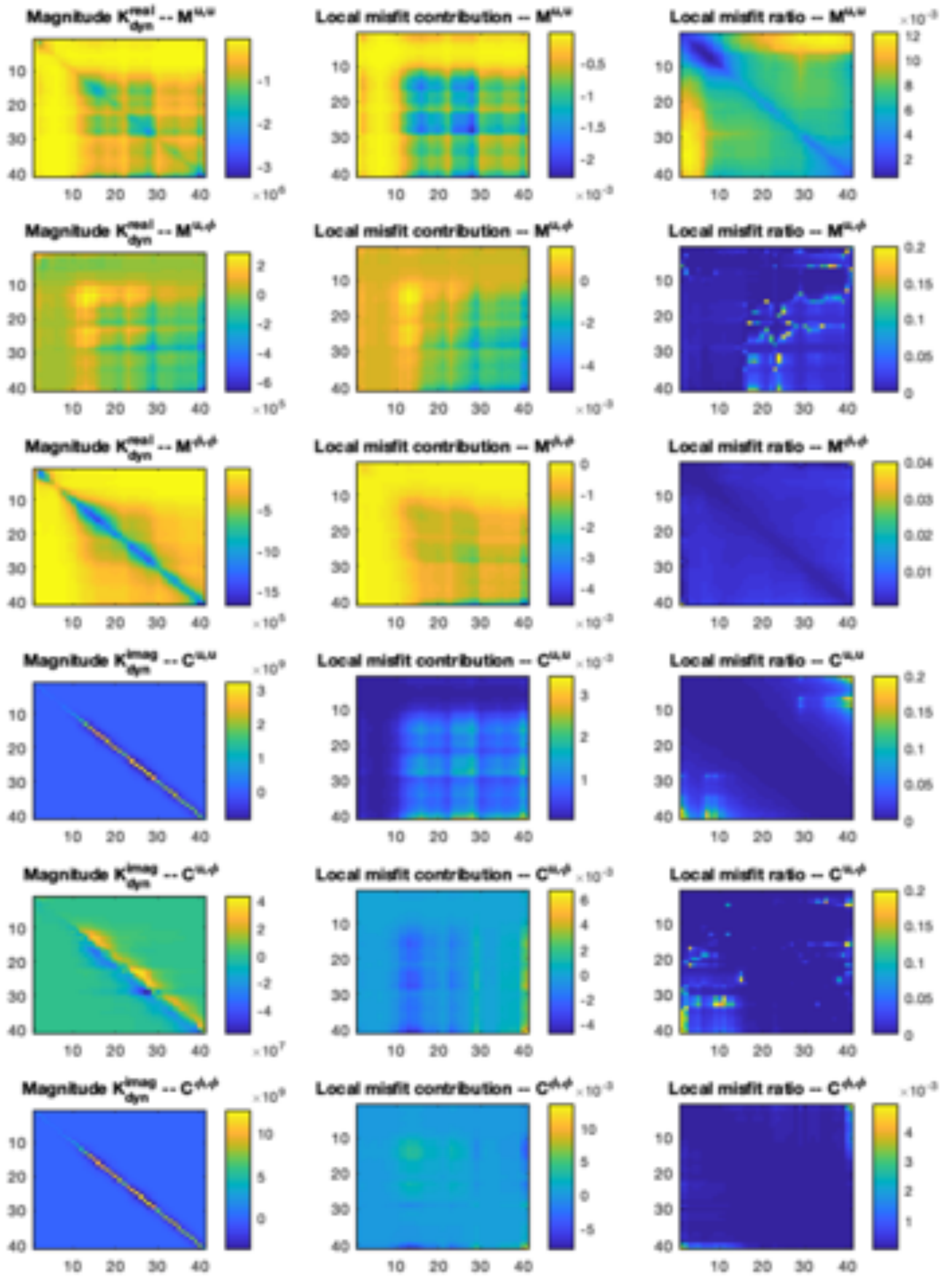

Figure 4.16: BC HS2, bedrock at 50m. Visual representation of misfits for mass and damping matrices. The left column shows the summed magnitude over frequency for the elements in the dynamic stiffness matrices. The middle column presents the contribution of local misfit to the total misfit (eq: (4.10)–(4.11)). In the last column the local ratio is presented as calculated by eq. (4.10)–(4.11)

4.5.1. EVALUATION IMPORTANCE ADDED MASS

Now that more confidence is obtained that the frequency-dependent part of the real dynamic stiffness, as calculated by the 3D model, is accurately captured by means of impedance coefficient matrices, the remaining question is if, and to what extent, this mass is important to take into account in further computations. Compared to the imaginary part of the dynamic stiffness, the real part shows small frequency dependence. This section provides more insight in the frequency range when the approximated mass becomes a significant part of real dynamic stiffness on a local level. The global system frequency response of the pile-soil system will be presented in section 5.3. Herein, more insight will be given in the importance of the approximated soil mass in the global system.

The previous section concluded that the impedance coefficient matrices are very capable in representing the the complex-valued dynamic stiffness. The coefficient matrices are used to assess the importance of added mass to the total real-valued dynamic stiffness. An assumption is made that the forces associated with the mass become significant when its contribution is greater than 10% of the static stiffness. In equation form this yields:

$$f_{sig_{i,j}}^{ii,jj} \geq \sqrt{\frac{0.1K_{i,j}^{ii,jj}}{M_{i,j}^{ii,jj}}} \cdot \frac{1}{2\pi} \qquad i,j = 1,2,...,41 \qquad ii,jj = u,\phi \tag{4.14}$$

wherein, $M_{i,j}^{ii,jj}$ and $K_{i,j}^{ii,jj}$ are the frequency-independent stiffness and mass coefficients. ω is the angular frequency in rad/m. $f_{sig_{i,j}}^{ii,jj}$ is the frequency for which the mass becomes significant in Hertz.

Figure 4.17 shows for which frequencies (in Hertz) the diagonals of the mass matrix become significant for BC HS1 and BC HS2 (bedrock at 50m).

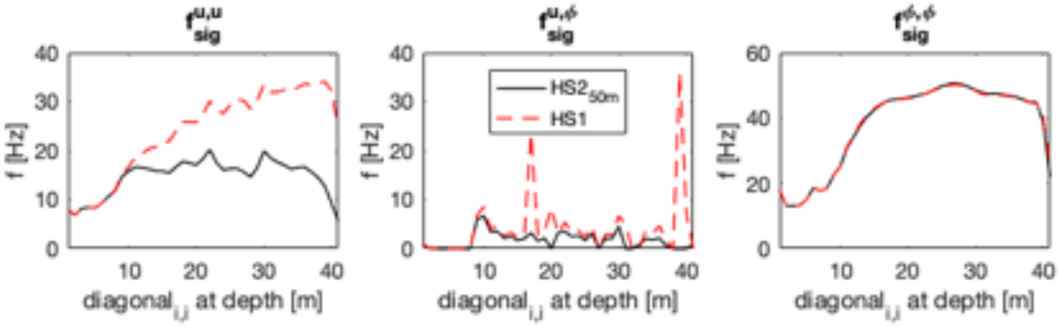

Figure 4.17: Frequencies for which the forces associated with the diagonals of the mass becomes larger than 10% of the static stiffness. $f_{sig}^{u,u}$, $f_{sig}^{u,\phi}$ and $f_{sig}^{\phi,\phi}$ present the frequencies for which respectively $M^{u,u}$, $M^{u,\phi}$ and $M^{\phi,\phi}$ become significant. $f = \omega/(2\pi)$.

The figures illustrate, for the real valued lateral (a) and rotational stiffness matrices (b), the added mass becomes significant at frequencies above 6 Hz. The mass becomes important for frequencies above 1-2 Hz for the coupling matrices. The rotational added mass only becomes significant at frequencies above 20 Hz. It is expected that the coupling stiffness, is less important to the total system response than the lateral and rotational dynamic stiffness as the magnitude of the coefficients is smaller. Large unexpected differences are observed in the left-hand-side and middle figure between the boundary conditions. Since the coupling stiffness and added mass are expected to be less important to the global SSI response, the reason for the difference is only examined for $f_{sig}^{u,u}$. figure 4.18 is created to understand the reason for this difference.

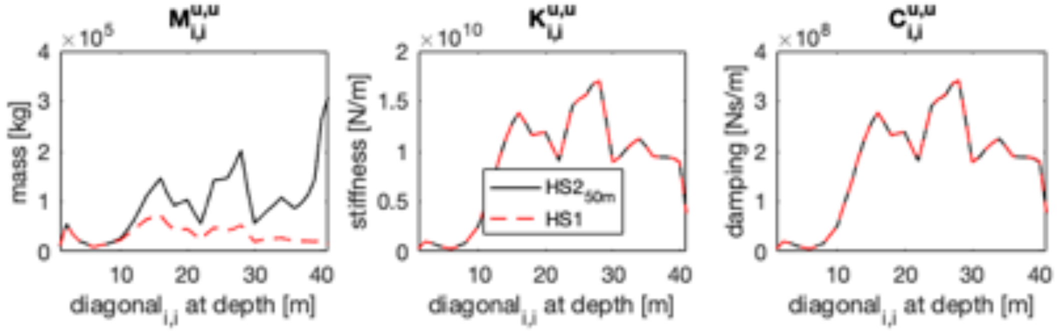

Figure 4.18: Diagonals of the lateral added mass, stiffness and damping coefficient matrices.

The values of the diagonals of the coefficient matrices are presented in the above figure. The diagonals of the stiffness and damping are the same for both boundary conditions. This is, however, not the case for the added mass. The added mass that is calculated by the 3D model for BC HS2 (bedrock at 50m) is significantly larger than for BC HS1. It is expected that the added mass near the diagonal node at the bottom of the cavity (i,j=41,41) should strongly increase. These nodes do not only represent the soil inertia of the soil laterally to the ring of nodes, but also the soil beneath the cavity. Therefore, a significant increase of mass is expected at the bottom nodes. The added mass of the soil for BC HS2 behaves more in line with expectations than the added mass for HS1. Overall, the added mass develops proportional to the stiffness with a significant increase of added mass at the bottom diagonal node. The added mass for BC HS1 develops less proportional to the stiffness and the mass reduces at the bottom node. This justifies the conclusion that the added mass (or, equivalently, the frequency-dependent part of the real-valued lateral dynamic stiffness) is under-estimated by the 3D model for BC HS1. It is expected that this under-estimation is related to errors in the PML formulation. However, since the mass is very small compared to the static stiffness, this error is not expected to have a large effect to the global SSI response.

To complete this section, figures 4.19a and 4.19b present for which frequencies the forces associated with the added mass become significant for all local and non-local elements. The colours are scaled from dark blue to yellow, representing 0 to 3 Hz. The large threshold shift with increasing depth of the left-hand-side subfigure of figure 4.19a is caused by the under-estimation of added mass by the 3D model for BC HS1. For non-local elements, the added mass can become significant for low frequencies. However, it should be noted that the contribution of the off-diagonals to the total real dynamic stiffness is limited. Even tough the frequency dependence of off-diagonals is pronounced for lower frequencies, the contribution of the mass to the total dynamic stiffness is expected to be negligible for the frequency range 0 – 0.3 Hz.

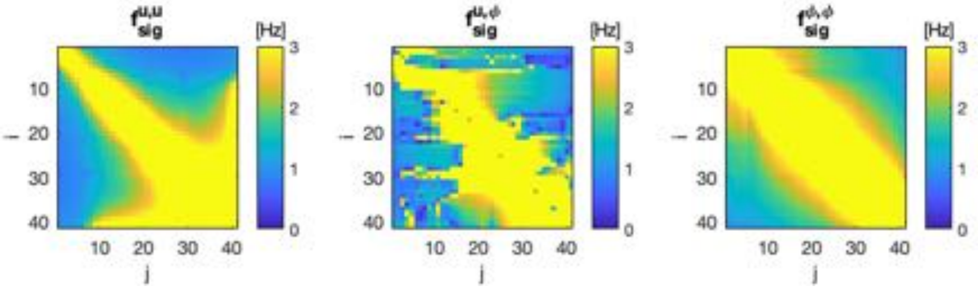

(a) BC HS1

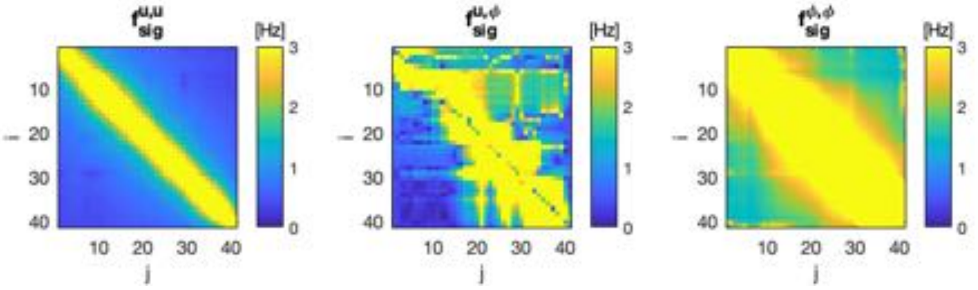

(b) BC HS2 (bedrock at 50m)

Figure 4.19: Frequencies for which the forces associated of the elements in the added mass matrices become significant. The results for BC HS1 and BC HS2 (bedrock at 50m) are shown in subfigures a) and b)

CONCLUDING REMARKS

The real part of the dynamic stiffness experiences small resonance dips above the cut-off frequency when BC HS2 is applied. As the coefficient matrices are derived for frequencies below the first resonance frequency, the coefficients for the mass matrix are less accurate for excitation frequencies above that frequency. The contribution of the mass is slightly higher for low frequencies when comparing BC HS2 to HS1. The previous section concluded that there are possibly some errors in the estimation of the dynamic soil stiffness for BC HS1. These could be related to errors in the PML formulation. However, this is not examined further due to limited available time. In the frequency range below the first soil resonance frequency, the mass does not contribute significantly to the total real dynamic stiffness.

The decision to work with either BC HS1 or HS2 depends on the soil stratigraphy of the specific site. The soil stratigraphy in the Dutch coastal waters consists mainly of sand and there is no rock layer present for at least

150 meters depth [37]. It is recommendable to work with BC HS1 in absence of a rigid soil layer. if the site is located in an area near volcanic activity, it is likely that a stiff soil layer is present. In that case, the depth of this layer should be identified and included in BC HS2.

A final remark is that, even though the mass appears to be negligible for offshore wind application, there are systems where the mass can have a significant contribution to the total stiffness. In case of much stiffer structures, the natural frequency may tough the frequency regime for which the mass of the soil becomes significant. In this thesis, it is not a problem to include the mass in further computations as long as the coefficients of the mass and stiffness are able to correctly represent the real part of the dynamic stiffness.

5

1D APPROXIMATION OF PILE-SOIL SYSTEM

5.1. INTRODUCTION AND REASON FOR 1D

This section describes the 1D Timoshenko beam model on a non-local Winkler foundation. It is explained how the continuous beam is discretized by an Euler's central finite difference scheme and how the general equations are solved in both the frequency and time domain. The 1D approximated SSI response is compared with the 3D SSI response in the frequency domain.

5.2. MODEL DESCRIPTION 1D MONOPILE MODEL

The beam theory applied in this thesis is the Timoshenko beam. An advantage of this beam theory is that it takes into account shear deformation and rotational bending effects, making it suitable for describing the behaviour of rigid, or thick, beams [7]. Euler's Finite Central Differences approach is adopted to discretize the beam in a finite amount of elements in space[38]. The following equations of motion hold in the time domain:

$$-\rho A\frac{d^2u}{dt^2}+GA\kappa\left(\frac{d^2u(z)}{dz^2}-\frac{d\phi(z)}{dz}\right)=-q(z,u,\phi,t) \tag{5.1}$$

$$-\rho I\frac{d^2\phi}{dt^2}+GA\kappa\left(\frac{du(z)}{dz}-\phi\right)+EI\frac{d^2\phi}{dz^2}=-m(z,u,\phi,t) \tag{5.2}$$

When the equations are translated to the frequency domain they will get the following form:

$$\omega^2\rho Au(z)+GA\kappa\left(\frac{d^2u(z)}{dz^2}-\frac{d\phi(z)}{dz}\right)=-q(z,u,\phi) \tag{5.3}$$

$$\omega^2\rho I\phi(z)+GA\kappa\left(\frac{du(z)}{dz}-\phi\right)+EI\frac{d^2\phi}{dz^2}=-m(z,u,\phi) \tag{5.4}$$

In which the dependent variables are translational displacement of the beam $u(z,t)$ and the angular displacement (rotation) $\phi(z,t)$. The other variables are:

- ρ is the material density of the beam in $[kg/m^3]$.
- A is the cross section area in $[m^2]$.
- κ is the Timoshenko shear constant $[-]$.
- G is the shear modulus in $[N/m^2]$.
- $q(z,u,\phi,t)$ is a distributed load in $[N/m]$.
- I is the second moment area in $[m^4]$.

Eq.(5.3) describes the balance of lateral forces, and Eq. (5.4) describes the balance of bending moments. Herein, $q(z,u,\phi)$ is the distributed restoring force and $m(z,u,\phi)$ is the distributed restoring moment. The in section 4.4 estimated complex dynamic soil stiffness is added to the beam equations. The general equations become:

$$\omega^2 \rho A u(z) + GA\kappa\left(\frac{d^2u(z)}{dz^2} - \frac{d\phi(z)}{dz}\right) - \int_0^L \mathring{K}^{u,u}(z,\overline{z})u(\overline{z})d\overline{z} - \int_0^L \mathring{K}^{u,\phi}(z,\overline{z})\phi(\overline{z})d\overline{z} = 0 \tag{5.5}$$

$$\omega^2 \rho I \phi(z) + GA\kappa\left(\frac{du(z)}{dz} - \phi\right) + EI\frac{d^2\phi}{dz^2} - \int_0^L \mathring{K}^{\phi,\phi}(z,\overline{z})\phi(\overline{z})d\overline{z} - \int_0^L \mathring{K}^{\phi,u}(z,\overline{z})u(\overline{z})d\overline{z} = 0 \tag{5.6}$$

In which the integrals represent the complex-valued dynamic soil reaction.

A number of boundary conditions (BC's) for the beam can be described. Both the tip and the head of the beam are free ends i.e. no fixed or hinged ends. Since there are second order derivatives with respect to space in the equation, each Timoshenko equation requires two boundary condition at each beam end. The two boundary conditions at the tip of the pile and at the seabed require that the sum of moments and the sum of forces at the seabed and tip of the pile are both equal to zero (free end). In equation form, in which the z-coordinate describes the length of the monopile, starting from the bottom at z = -L$_s$ towards the pile head at z = 0:

$$GA\kappa\left(\frac{du}{dz} - \phi\right)\Big|_{z=0} = -F \tag{5.7}$$

$$EI\frac{d\phi}{dz}\Big|_{z=0} = M \tag{5.8}$$

$$GA\kappa\left(\frac{du}{dz} - \phi\right)\Big|_{z=-L_s} = 0 \tag{5.9}$$

$$EI\frac{d\phi}{dz}\Big|_{z=-L_s} = 0 \tag{5.10}$$

5.2.1. SPACE DISCRETIZATION

The equation of motion that needs to be solved contains first and second order derivatives with respect to space. Since in a later stage an ordinary differential equation (ODE) solver will be used in Matlab, it is required to use a Taylor Series Expansion (TSE) to describe the first and second order terms with respect to space. These can then be solved using Matlab's ODE solvers in the time domain. For the space derivatives, the Euler's central finite differences method is applied [39]. A first and second order term around u_n can be described using a third order Taylor series expansion:

$$TSE = w_{x_n} + w'_{x_n}(x-x_n) + \frac{1}{2}w''_{x_n}(x-x_n)^2 + O(x-x_n)^3 \tag{5.11}$$

A three-point discretization scheme will be used, meaning that the TSE will be evaluated at three points: $w_{n-1}, \quad w_n, \quad w_{n+1}$. Then, a solution is sought in the shape of:

$$sol = a\cdot w_{n-1} + b\cdot w_n + c\cdot w_{n+1}$$

A set of 3 equations with 3 unknowns is solved to describe the first and second order derivatives, resulting in the following parameters:

$$1^{st}\text{ order: } a = \frac{1}{h^2}, \quad b = \frac{-2}{h^2}, \quad c = \frac{1}{h^2}$$

$$2^{nd}\text{ order: } a = \frac{-1}{2h}, \quad b = 0, \quad c = \frac{1}{2h}$$

Using the above obtained knowledge, a first and second order derivative at a certain location can be described using the node before and after. The solution of the Timoshenko beam on a non-local foundation is discretized in an domain of length L_s and n equally spaced points. The discretization length is $h = \frac{L_s}{n-1}$ meter. The complex-valued dynamic stiffness matrices, as derived in section 4.4 are added to the equations.

These stiffness matrices are derived for the same discretization length as the beam. In equation form this is represented as:

$$\rho A\omega^2 + \frac{GA\kappa}{h^2}(u_{i-1} - 2u_i + u_{i+1}) - \widetilde{K}^{u,u}_{i,j}u_j - \frac{GA\kappa}{2h}(-\phi_{i-1} + \phi_{i+1}) - \widetilde{K}^{u,\phi}_{i,j}\phi_j = 0 \tag{5.12}$$

$$\rho I\omega^2 + \frac{GA\kappa}{2h}(-u_{i-1} + u_{i+1}) - \widetilde{K}^{\phi,u}_{i,j}u_j - GA\kappa\phi_i + \frac{EI}{h^2}(\phi_{i-1} - 2\phi_i + \phi_{i+1}) - \widetilde{K}^{\phi,\phi}_{i,j}\phi_j = 0 \tag{5.13}$$

For $i = 1:1:n$ and $j = 0:1:(n+1)$. $\widetilde{K}^{u,u} = -\omega^2 M^{u,u} + iC^{u,u}\omega + K^{u,u}$, where $\widetilde{K}^{u,\phi}$, $\widetilde{K}^{\phi,u}$ & $\widetilde{K}^{\phi,\phi}$ are assembled in the same manner. The tilde (~) over the stiffness matrices stands for auxiliary matrices, wherin the first and last column is multiplied by $h = 0.5[m]$.

5.2.2. BOUNDARY CONDITIONS

Taking into account the knowledge derived above, the system can be described as a combination of finite elements. The problem that still occurs is that there are extra elements in the equations that have no physical meaning. This is illustrated in figure 5.1, in which the beam is modelled sideways, consisting of n elements from the seabed to the tip of the pile.

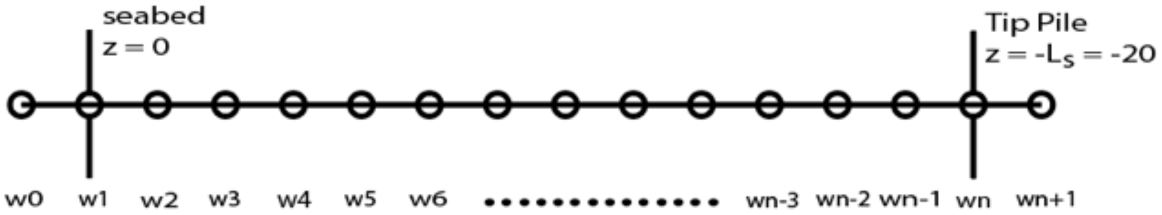

Figure 5.1: Discretized monopile as a beam with n elements

The fictive nodes (often referred to as ghost nodes) that have to be dealt with are w_0 and w_{n+1}. To remove these from the finite differences scheme, the boundary conditions (Eqs. 5.7 – 5.10) derived in section 5.2 are used. The boundary conditions for the first Timoshenko beam equation are solved to isolate the ghost nodes u_0 and ϕ_0:

$$GA\kappa\left(\frac{-u_0 + u_2}{2h} - \phi_1\right) = -F, \qquad u_0 = \frac{2h}{GA\kappa}F - 2h\phi_1 + u2 \tag{5.14}$$

$$EI\left(\frac{-\phi_0 + \phi_2}{2h}\right) = M, \qquad \phi_0 = \frac{-2h}{EI}M + \phi_2 \tag{5.15}$$

$$GA\kappa\left(\frac{-u_{n-1} + u_{n+1}}{2h} - \phi_n\right) = 0, \qquad u_{n+1} = 2h\phi_n + u_{n-1} \tag{5.16}$$

$$EI\left(\frac{-\phi_{n-1} + \phi_{n+1}}{2h}\right) = 0, \qquad \phi_{n+1} = \phi_{n+1} \tag{5.17}$$

Substituting equations (5.14) – (5.17) into equations (5.12) and (5.13) for $i = 1$ and $i = n$ yields:

$$\frac{GA\kappa}{h^2}(-2u_1 + 2u_2) - \widetilde{K}^{u,u}_{1,j}u_j - \frac{2GA\kappa}{h}\phi_1 - \widetilde{K}^{u,\phi}_{1,j}\phi_j = -\frac{2F}{h} + \frac{GA\kappa M}{EI} \qquad \text{for } i = 1 \tag{5.18}$$

$$-\widetilde{K}^{\phi,u}_{1,j}u_j + \frac{EI}{h^2}(-2\phi_1 + 2\phi_2) - \widetilde{K}^{\phi,\phi}_{1,j}\phi_j = F + \frac{2M}{h} \qquad \text{for } i = 1 \tag{5.19}$$

$$\frac{GA\kappa}{h^2}(-2u_{n-1} + 2u_{n+1}) - \widetilde{K}^{u,u}_{n,j}u_j - \frac{2GA\kappa}{h}\phi_n - \widetilde{K}^{u,\phi}_{n,j}\phi_j = 0 \qquad \text{for } i = n \tag{5.20}$$

$$-\widetilde{K}^{\phi,u}_{n,j}u_j + \frac{EI}{h^2}(-2\phi_{n-1} + 2\phi_{n+1}) - \widetilde{K}^{\phi,\phi}_{n,j}\phi_j = 0 \qquad \text{for } i = n \tag{5.21}$$

The ghost nodes ($j = 0$ and $j = n+1$) are now successfully removed from equations. The next step is to develop the matrices. For $i = 1$ and $i = n$ the equations (5.18)–(5.21) are used. The inner domain of the matrices are assembled according to equations (5.12) and (5.13). Equations (5.22) – (5.25) show the resulting matrices of the finite central differences approach for the Timoshenko beam.

$$FDM_{U1}=\frac{GA\kappa}{h^2}\begin{bmatrix}-2&2&0&0&\dots&0&0&0&0\\1&-2&1&0&\dots&0&0&0&0\\0&1&-2&1&\dots&0&0&0&0\\\vdots&\vdots&\vdots&\vdots&\ddots&\vdots&\vdots&\vdots&\vdots\\0&0&0&0&\dots&1&-2&1&0\\0&0&0&0&\dots&0&1&-2&1\\0&0&0&0&\dots&0&0&2&-2\end{bmatrix}\tag{5.22}$$

$$FDM_{\phi 1}=\frac{-GA\kappa}{2h}\begin{bmatrix}4&0&0&0&\dots&0&0&0&0\\-1&0&1&0&\dots&0&0&0&0\\0&-1&0&1&\dots&0&0&0&0\\\vdots&\vdots&\vdots&\vdots&\ddots&\vdots&\vdots&\vdots&\vdots\\0&0&0&0&\dots&-1&0&1&0\\0&0&0&0&\dots&0&-1&0&1\\0&0&0&0&\dots&0&0&0&4\end{bmatrix}\tag{5.23}$$

$$FDM_{u2}=\frac{GA\kappa}{2h}\begin{bmatrix}0&0&0&0&\dots&0&0&0&0\\-1&0&1&0&\dots&0&0&0&0\\0&-1&0&1&\dots&0&0&0&0\\\vdots&\vdots&\vdots&\vdots&\ddots&\vdots&\vdots&\vdots&\vdots\\0&0&0&0&\dots&-1&0&1&0\\0&0&0&0&\dots&0&-1&0&1\\0&0&0&0&\dots&0&0&0&0\end{bmatrix}\tag{5.24}$$

$$FDM_{\phi 2}=\frac{EI}{h^2}\begin{bmatrix}-2&2&0&0&\dots&0&0&0&0\\1&-2&1&0&\dots&0&0&0&0\\0&1&-2&1&\dots&0&0&0&0\\\vdots&\vdots&\vdots&\vdots&\ddots&\vdots&\vdots&\vdots&\vdots\\0&0&0&0&\dots&1&-2&1&0\\0&0&0&0&\dots&0&1&-2&1\\0&0&0&0&\dots&0&0&2&-2\end{bmatrix}-GA\kappa_{i,i}\tag{5.25}$$

Equation (5.26) and (5.27) show the final discretized Timoshenko equations including complex-valued dynamic soil stiffness as it can be used in the frequency-domain computations.

$$-\rho A\omega^2\mathbf{I}_n\begin{bmatrix}u_1\\u_2\\\vdots\\u_{n-1}\\u_n\end{bmatrix}+FDM_{U1}\begin{bmatrix}u_1\\u_2\\\vdots\\u_{n-1}\\u_n\end{bmatrix}-\widetilde{K}^{u,u}_{i,j}\begin{bmatrix}u_1\\u_2\\\vdots\\u_{n-1}\\u_n\end{bmatrix}+FDM_{\phi 1}\begin{bmatrix}\phi_1\\\phi_2\\\vdots\\\phi_{n-1}\\\phi_n\end{bmatrix}-\widetilde{K}^{u,\phi}_{i,j}\begin{bmatrix}\phi_1\\\phi_2\\\vdots\\\phi_{n-1}\\\phi_n\end{bmatrix}=\begin{bmatrix}-\frac{2F}{h}+\frac{GA\kappa M}{EI}\\0\\\vdots\\0\\0\end{bmatrix}=F1\tag{5.26}$$

$$-\rho I\omega^2\mathbf{I}_n\begin{bmatrix}\phi_1\\\phi_2\\\vdots\\\phi_{n-1}\\\phi_n\end{bmatrix}+FDM_{U2}\begin{bmatrix}u_1\\u_2\\\vdots\\u_{n-1}\\u_n\end{bmatrix}-\widetilde{K}^{\phi,u}_{i,j}\begin{bmatrix}u_1\\u_2\\\vdots\\u_{n-1}\\u_n\end{bmatrix}+FDM_{\phi 2}\begin{bmatrix}\phi_1\\\phi_2\\\vdots\\\phi_{n-1}\\\phi_n\end{bmatrix}-\widetilde{K}^{\phi,\phi}_{i,j}\begin{bmatrix}\phi_1\\\phi_2\\\vdots\\\phi_{n-1}\\\phi_n\end{bmatrix}=\begin{bmatrix}F+\frac{2M}{h}\\0\\\vdots\\0\\0\end{bmatrix}=F2\tag{5.27}$$

Herein: $\widetilde{K}^{ii,jj}_{i,j}=-\omega^2M^{ii,jj}_{i,j}+i\omega C^{ii,jj}_{i,j}+K^{ii,jj}_{i,j}$ for $ii=u,\phi\quad,\quad jj=u,\phi\quad,\quad i=1:n$ and $j=1:n$. The tilde stands for the matrices being auxiliary matrices, in which the first and last column are multiplied by the discretization length $h=0.5m$

These equations can be solved by means of collecting the variables that are dependent on u and ϕ, stacking the matrices and vectors vertically on top of each other (eq: 5.28) and solving for $[u;\phi] = B^{-1}F$:

$$\underbrace{\left(\underbrace{\begin{bmatrix} -\rho A\omega^2\mathbf{I}_n + FDM_{U1} & FDM_{\phi 1} \\ FDM_{U2} & -\rho I\omega^2\mathbf{I}_n + FDM_{\phi 2} \end{bmatrix}}_{B_p} - \underbrace{\begin{bmatrix} \widetilde{K}^{u,u}_{i,j} & \widetilde{K}^{u,\phi}_{i,j} \\ \widetilde{K}^{\phi,u}_{i,j} & \widetilde{K}^{\phi,\phi}_{i,j} \end{bmatrix}}_{B_s}\right)}_{B} \begin{bmatrix} u \\ \phi \end{bmatrix} = \begin{bmatrix} F1 \\ F2 \end{bmatrix} \tag{5.28}$$

5.3. FREQUENCY DOMAIN PILE-SOIL

The 1D model should be validated to conclude whether the calculated pile response, with the estimated stiffness, damping and mass coefficient matrices, gives an accurate representation of the 3D pile-soil response as calculated by the FE model. The applied validation method in the dissertation of Versteijlen [7] is taken as a basis. Both the 3D and 1D models are adjusted to match the input of the model. The SSI response of the 1D model with the approximated added mass, damping and stiffness coefficient matrices is compared with the complex-valued 3D SSI response, as is calculated by the 3D model. An accurate match between the 3D and 1D model is desirable since it indicates the performance of the approximated frequency independent mass, damping and stiffness coefficients are in capturing the 3D response. The results will show if, and in what frequency range, the 1D beam with approximated coefficient matrices is able to represent the 3D SSI response. When large deviations between the 3D and 1D model occur, the method will not longer be applicable. Therefore, the error between responses of the 3D pile-soil response and the 1D pile-soil response needs to be calculated. The 3D frequency response is compared with the 1^{st} , 2^{nd} and 3^{th} order 1D approximated impedance functions. Note that the mass, stiffness and damping matrices are the frequency independent approximated coefficient matrices as derived in section 4.4. The 3D response is also compared with the frequency-dependent complex-valued dynamic stiffness matrices as directly extracted from the 3D model. The frequency-domain response is calculated by equation 5.28. The pile properties (B_P) are not varied. The added mass, stiffness and damping of the soil is captured in B_s. The frequency-domain model is computed for four cases:

- $R1:$ 1^{st} order system without added mass: $B_s = (i\omega C + K)$
- $R2:$ 2^{nd} order system: $B_s = -\omega^2 M + i\omega C + K$
- $R3:$ 3^{th} order system with higher order damping term: $B_s = -\omega^2 M + i\omega(C - \omega^2 C_3) + K$
- $R4:$ Directly extracted complex dynamic stiffness from 3D model: $B_s = K_{direct}$

Case R4 represents the non-local method that was applied in the work of Versteijlen [7] and is the most direct approach. The complex-valued global soil reactions are extracted from the 3D model and inserted the 1D model. This method yields an exact representation of the 3D soil reaction. This is a more direct approach because no polynomial approximation is applied to extract frequency-independent mass, damping and stiffness coefficient matrices. R4 is thus frequency dependent. It is expected that the direct approach yields the highest accuracy in fit between the complex-valued 3D and 1D SSI response. The difference in SSI response of R4 and the 3D is related to the different models used for the pile: the 1D beam versus the solid elements of the 3D model [7].

In R1 – R3, the coefficient matrices M,C & K contain all four matrices for added mass, damping and stiffness in the form: $X = [X^{u,u}\ X^{u,\phi}\ ;\ X^{\phi,u}\ X^{\phi,\phi}]$ for $X = M, C, K$. C_3 has not been mentioned before. This matrix is included in R3 to assess whether an additional damping term yields a higher accuracy in the frequency-domain computations. It is calculated by means of calculating the third degree polynomial over the residual of the imaginary part of the dynamic stiffness. The residual is calculated by:

$$\text{residual} = \text{Im}\left(K^{ii,jj}_{dyn}(\omega)\right) - \omega C^{ii,jj} \qquad \text{for: } ii = u,\phi \text{ and } jj = u,\phi$$

Figure 5.2 shows the calculated dynamic pile-soil responses. The real and imaginary displacements and rotations are shown against depth (Z) for case HS1, no bedrock. A dynamic force and moment of 1 N and 45 Nm are applied at the pile head. Figures 5.2a and 5.2b show the SSI response at the excitation frequencies 0.3 Hz (1.88 rad/s) and 0.9 Hz (5.65 rad/s).

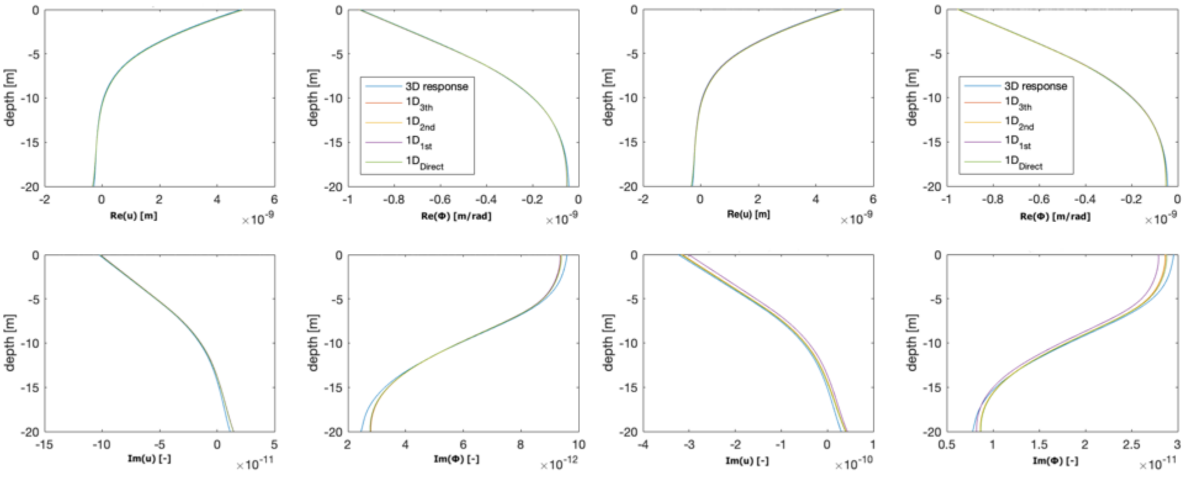

(a) Frequency response at 0.3 Hz (1.88 rad·s^{-1})

(b) Frequency response at 0.9 Hz (5.65 rad·s^{-1})

Figure 5.2: Dynamic frequency response of pile-soil system for the frequencies of 0.3 and 0.9 Hz. R1, R2, R3 and R4 are shown as $1D_{1th}$, $1D_{2nd}$, $1D_{3th}$ and $1D_{direct}$, respectively

At first sight, the match between the 1D SSI response and the 3D SSI response seems very accurate at frequencies. The 1D approximation shows a small under-prediction of the imaginary rotational stiffness at the head of the pile and a small over-prediction at the bottom of the pile at 0.3 Hz. The imaginary displacement is also slightly over-predicted at the tip of the pile. At 0.9 Hz, the first order (R1) approximation shows larger deviations from the 3D response. It is difficult to distinguish the lines in the figures. Therefore, an error function is developed to calculate the misfit between the 3D SSI response and the 1D SSI response. The total misfit is calculated by equation (5.29). The misfits that correspond to the real and imaginary response is calculated by equations (5.30) and (5.31).

$$C_{u,\phi}^{total} = \frac{\sum_{i=0}^{i=N}\left|u_{i,1D} - u_{i,3D}\right|}{2\sum_{i=0}^{i=N}\left|u_{i,3D}\right|} + \frac{\sum_{i=0}^{i=N}\left|\phi_{i,1D} - \phi_{i,3D}\right|}{2\sum_{i=0}^{i=N}\left|\phi_{i,3D}\right|} \tag{5.29}$$

$$C_{u,\phi}^{real} = \frac{\sum_{i=0}^{i=N}\left|\mathrm{Re}(u_{i,1D}) - \mathrm{Re}(u_{i,3D})\right|}{2\sum_{i=0}^{i=N}\left|\mathrm{Re}(u_{i,3D})\right|} + \frac{\sum_{i=0}^{i=N}\left|\mathrm{Re}(\phi_{i,1D}) - \mathrm{Re}(\phi_{i,3D}\mathrm{Re}\right|}{2\sum_{i=0}^{i=N}\left|\mathrm{Re}(\phi_{i,3D})\right|} \tag{5.30}$$

$$C_{u,\phi}^{imag} = \frac{\sum_{i=0}^{i=N}\left|\mathrm{Im}(u_{i,1D}) - \mathrm{Im}(u_{i,3D})\right|}{2\sum_{i=0}^{i=N}\left|\mathrm{Im}(u_{i,3D})\right|} + \frac{\sum_{i=0}^{i=N}\left|\mathrm{Im}(\phi_{i,1D}) - \mathrm{Im}(\phi_{i,3D})\right|}{2\sum_{i=0}^{i=N}\left|\mathrm{Im}(\phi_{i,3D})\right|} \tag{5.31}$$

Please note that the absolute difference between the complex-valued responses is taken in equation (5.29). An example of how the absolute difference between two complex valued numbers is calculated is given below.

$$|(a+bi)-(c+di)| \quad = \quad |(a-c)+(b-d)i| \quad = \quad \sqrt{(a-c)^2+(b-d)^2}$$

The contribution of the misfit of the complex-valued response to the total misfit is under-valued compared to the contribution of the misfit of real-valued response. The reason is that the magnitudes of the real parts (a,c) are much larger than the imaginary parts (b,d). In this work, an assumption is made that the real and imaginary responses are equally important. Therefore, equation (5.29) will not be used to evaluate the perfomance of the 1D model to respresent the 3D SSI response. The total error is calculated by equation (5.32):

$$C_{u,\phi}^{total} = \frac{1}{2}\left(C_{u,\phi}^{real} + C_{u,\phi}^{imag}\right) \tag{5.32}$$

The misfits between the 3D and 1D response for the excitation frequencies 0.3 and 0.9 Hz are presented in tables 5.1 and 5.2 for the models with BC HS1 and HS2 (bedrock at 50m). More results are presented in appendix C for frequencies from 0 and 3 Hz. The real and imaginary misfits are calculated by equations (5.30) and (5.31), respectively. Please note that the misfits C_u and C_ϕ are divided by two so that they can be summed in C_{tot}.

Table 5.1: Case HS1: Real and imaginary misfits between 3D response and approximated response for the frequencies 0.3 and 0.9 Hz.

Error between fit 3D and 1D						
	0.3 Hz			0.9 Hz		
Case	C_{tot}	C_u	C_ϕ	C_{tot}	C_u	C_ϕ
$R4\ \Re$	0.0192	0.0152	0.0040	0.0178	0.0140	0.0038
$R4\ \Im$	0.0270	0.0179	0.0091	0.0327	0.0226	0.0101
$R3\ \Re$	0.0223	0.0172	0.0051	0.0221	0.0172	0.0049
$R3\ \Im$	0.0258	0.0162	0.0096	0.0358	0.0245	0.0113
$R2\ \Re$	0.0223	0.0172	0.0051	0.0224	0.0175	0.0049
$R2\ \Im$	0.0269	0.0173	0.0096	0.0452	0.0335	0.0117
$R1\ \Re$	0.0208	0.0159	0.0049	0.0106	0.0066	0.0040
$R1\ \Im$	0.0321	0.0218	0.0102	0.0936	0.0719	0.0217

Table 5.2: Case HS2, bedrock at 50m: Real and imaginary misfits between 3D response and approximated response for the frequencies 0.3 and 0.9 Hz.

Error between fit 3D and 1D						
	0.3 Hz			0.9 Hz		
Case	C_{tot}	C_u	C_ϕ	C_{tot}	C_u	C_ϕ
$R4\ \Re$	0.0198	0.0158	0.0040	0.0179	0.0141	0.0038
$R4\ \Im$	0.0152	0.0065	0.0087	0.0189	0.0093	0.0096
$R3\ \Re$	0.0229	0.0178	0.0051	0.0207	0.0159	0.0048
$R3\ \Im$	0.0172	0.0078	0.0094	0.0337	0.0234	0.0104
$R2\ \Re$	0.0229	0.0177	0.0051	0.0206	0.0158	0.0048
$R2\ \Im$	0.0173	0.0079	0.0094	0.0279	0.0176	0.0103
$R1\ \Re$	0.0216	0.0166	0.0049	0.0105	0.0066	0.0040
$R1\ \Im$	0.0169	0.0070	0.0099	0.0637	0.0460	0.0177

For case HS1, when looking at table 5.1, case R4 yields the highest accuracy with a total misfit of 0.0231 ($C_{tot,\Re}$ = 0.0192 and $C_{tot,\Im}$ = 0.0270) at 0.3 Hz and 0.0253 ($C_{tot,\Re}$ = 0.0178 and $C_{tot,\Im}$ = 0.0327) at 0.9 Hz. This misfit is a direct result of 3D versus 1D modelling and is considered very good. In this work, the real and complex valued dynamic stiffness is approximated with frequency-independent coefficient matrices that can directly be incorporated in a time-domain model. R4 is frequency dependent. Therefore, it cannot directly be included in a time-domain model. At 0.3 Hz, the misfit between the 3D response and R1–R3 is only slightly higher than the misfit related to R4. This indicates that the largest error is a result of modelling differences between 3D and 1D model, rather than the frequency-independent mass, stiffness and damping approximation. R1 – the first order system – is slightly more accurate than R2 and R3. At 0.9 Hz, the total misfits for R1, R2 and R3 are respectively 0.0521, 0.0338 and 0.0290. It is worth mentioning that the misfit in the imaginary response increases drastically for R1.

In case of HS2 (bedrock at 50m), R4 also yields the highest accuracy in predicting the 3D response. The total misfits are 0.0175 ($C_{tot,\Re}$ = 0.0198 and $C_{tot,\Im}$ = 0.0152) at 0.3 Hz and 0.0184 ($C_{tot,\Re}$ = 0.0179 and $C_{tot,\Im}$ = 0.0189) at 0.9 Hz. Again, R4 cannot be used in the time domain, hence a choice needs to be made between R1, R2 or R3. The total misfit of R1–R3 at 0.3 Hz are respectively 0.0193, 0.0201 and 0.0201. R1 shows slightly better results than R2 and R3. The excitation frequency of 0.9 Hz is well below the first resonance frequency of 1.5 Hz for the presence of bedrock at 50m. At 0.9 Hz, the total misfits for R1, R2 and R3 are respectively 0.371, 0.0243 and 0.0272. R2 – the second order system – yields the best fit between the 3D and 1D response. The misfit corresponding to the imaginary response of R1 yields the strongest growth. R2 yields a higher accuracy than R3 over a wider frequency range, R2 seems to be the appropriate method to proceed in this thesis.

For low frequencies, the 1D approximation of the 3D response with the presence of bedrock yields higher accuracy than BC HS1. At a depth of 50m the approximation is valid for frequencies up to the first resonance frequency of 1.5 Hz. If a bedrock is present at 200m depth, the frequency range in which the frequency independent dynamic stiffness can be approximated is 0–0.375 Hz. For higher frequencies, high misfits between 3D and 1D occur. The above is only assessed for two frequencies. To get a better understanding in the performance of the 1D approximation to mimic the 3D response, the misfits are plotted against excitation frequencies in figures 5.3a to 5.3d. These figures are also used to assess the most appropriate method (R1–R3) to proceed this thesis.

The figures illustrate that case R4 yields the highest accuracy overall. This is no surprise considering it is the most direct approach. The misfit of R4 is caused by the modelling differences between 3D and 1D modelling. For BC HS2, at all depths, the most accurate method is R2 – the second order system with added mass of the soil. When considering BC HS1, R3 shows a slightly higher accuracy. However, in an attempt to perform time-domain computations with a third order damping matrix, the system became unstable. Given the marginal improvement in fit between 3D and 1D in the frequency domain and the instability in the time domain, the third order method (R3) is no longer considered.

It is interesting to mention that including soil mass yields a higher misfit of the real lateral response and a significant lower misfit in both the imaginary lateral and rotational response. This remark holds for both boundary conditions HS1 and HS2 (at all considered depths). Figure 5.4 presents the misfit of the real-valued SSI response(Re $C_{u,\phi}$) and the misfits of the imaginary-valued SSI response (Im $C_{u,\phi}$). A trade-off is observed between the accuracy of the real and imaginary response. At frequencies exceeding 0.5 Hz, including soil mass (R2) yields far better fits in terms of complex-valued response, whereas excluding soil mass yields slightly better results in the fit of real-valued response. For low frequencies (<0.3 Hz), the contribution of the added mass of the soil to the total system response is marginal as the misfits for R1 and R2 are very similar. This was expected because the relative contribution of the mass to the total real part of dynamic stiffness is small, compared to the static stiffness. The mass becomes important at higher frequencies. A strong improvement in fit between the imaginary 3D response and approximated 1D response is observed, with a small trade-off in terms of the fits of the real response. When applying equation (5.32), R2 yields an overall improvement in fit compared to the 1st order system. Other interesting phenomena are the regions of strong increase in the misfits that are present in figure 5.3d. When the excitation comes close to the soil cut-off (resonance) frequency of 0.365 Hz, the misfit drastically increases. The imaginary lateral response is very frequency dependent and more sensitive to resonances in the soil. The mass is, as explained in section 4.4, approximated with a 2nd degree polynomial (parabolic) and can not deal with sudden increases/decreases in dynamic soil stiffness. In addition, as shown in section 4.3.3, the non-local imaginary part of the lateral dynamic stiffness is less monotonic linear frequency dependent and more sensitive to resonances, causing a higher misfit in the linear assumption.

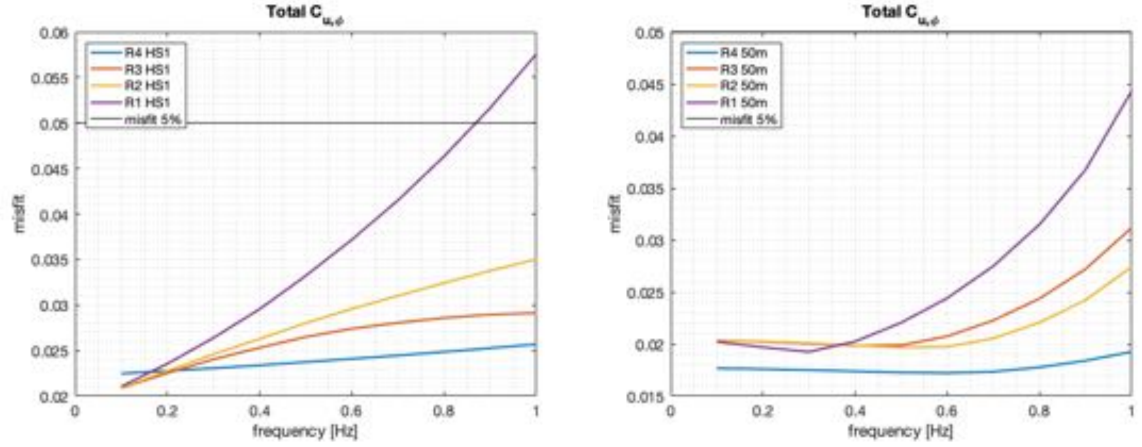

(a) misfits for R1–R4 for case HS1, no bedrock

(b) misfits for R1–R4 for case HS2, bedrock at 50m

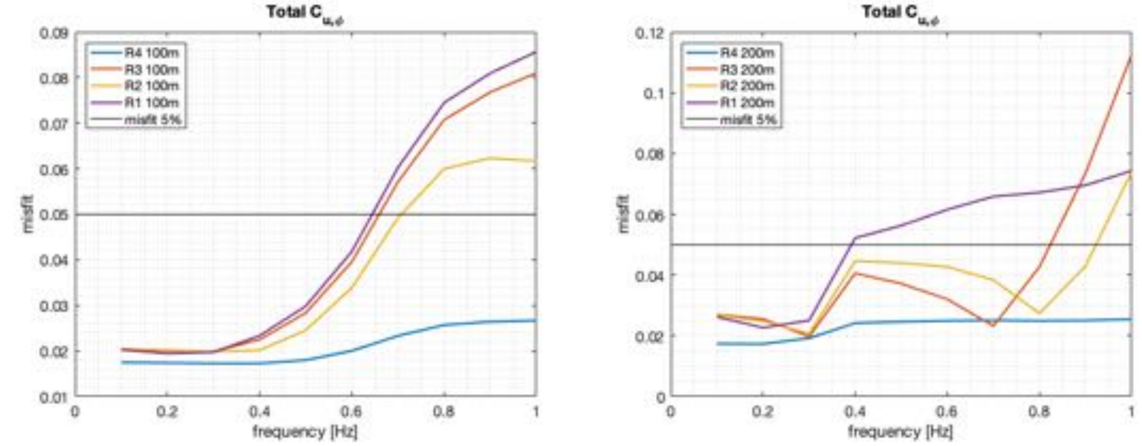

(c) misfits for R1–R4 for case HS2, bedrock at 100m

(d) misfits for R1–R4 for case HS2, bedrock at 200m

Figure 5.3: subfigures (a) – (b) show the misfits of R1–R4 for respectively HS1, HS2$_{50m}$, HS2$_{100m}$ and HS2$_{200m}$. The black line represents the 5% error limit

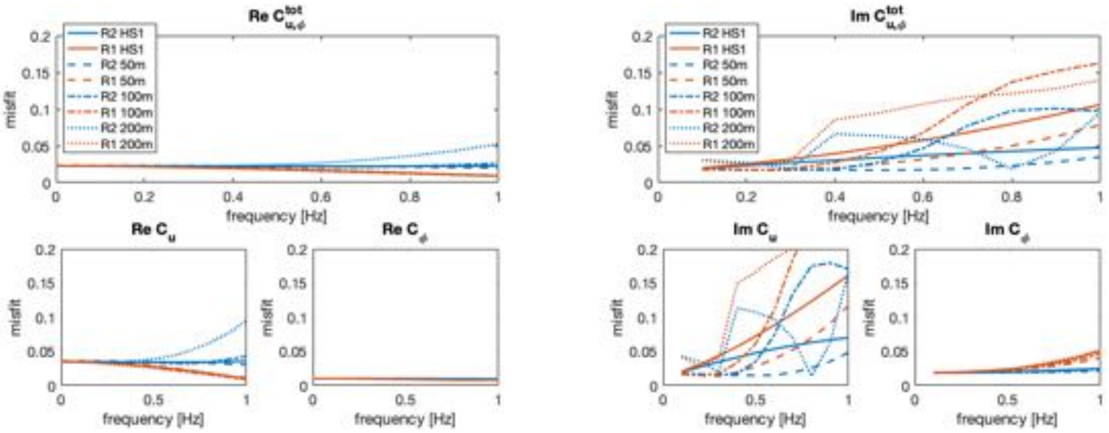

(a) Total real misfit and decomposition in lateral and rotational misfit.

(b) Total imaginary misfit and decomposition in imaginary lateral and rotational misfit.

Figure 5.4: Comparison case R2 and R1 for boundary conditions HS1 and HS2 (50, 100 & 200m).

5.3.1. CONCLUDING REMARKS

The 1D SSI response with approximated stiffness, mass and damping coefficient matrices is compared with the 3D SSI response over a wide range of excitation frequencies. The 1D model with approximated mass, stiffness and damping matrices is very accurate in terms of predicting the 3D SSI response of a pile embedded in soil. Directly extracting the 3D dynamic stiffness and implementing this in a 1D model, just like was done in the work of Versteijlen [7], yields the highest accuracy with a misfit between 3D and 1D SS1 response of approximately 2% for the frequency range 0 to 0.5 Hz. The misfits for case R1–R3 is slightly higher. This is considered no surprise as, besides the differences between 3D and 1D modelling, the dynamic stiffness is approximated by frequency-independent coefficients. Case R4 is frequency dependent, which means that it cannot directly be applied in the time domain. Therefore, a decision has to be made for case R1 to R3. Boundary condition HS2 yields slightly higher accuracy in prediction the 3D response than HS1. In section 4.5.1 is concluded that there might be some errors calculating the dynamic soil stiffness of a soil continuum overlaying a soft half-space. The errors are expected to be a result of the PML formulation. However, this is not further examined in this thesis because of limited available time. The misfits related to the SSI response of a pile in a soil continuum overlaying a bedrock are slightly lower. However, the misfit increases rapidly at frequencies above the first depth dependent resonance (cut-off) frequency. The second degree system (R2), with inclusion of added mass of the soil, yields the highest accuracy overall. For the frequency range 0 – 0.3 Hz, the misfit of R2 is approximately 2.5%. Including soil mass yields much higher accuracy in predicting the imaginary-valued 3D response with a small trade-off in the prediction of the real-valued SSI response. The method is shown to be valid as the fit between the 3D response and the 1D approximation, with coefficient matrices, is very accurate. The approximated coefficient matrices will be included in the time-domain model and boundary condition HS1 will be applied. The effect of including soil mass in the time domain computations will be analysed further.

5.4. TIME DOMAIN PILE-SOIL

In chapter 5.3 is investigated to what extent the frequency-independent coefficient matrices are able to predict the 3D response in an accurate manner. The results are very promising. This section focuses on time-domain computations for a monopile embedded in soil (without tower). Some modifications are applied to translate the frequency-domain equations of the Timoshenko beam (eq: (5.28)) and the dynamic soil stiffness to the time domain. If the mass, damping and stiffness coefficient matrices are assumed to be frequency independent, they can be directly implemented in the time-domain equation (eq: (5.33)).

$$\begin{aligned}&\underbrace{\left(\underbrace{\begin{bmatrix}\rho A\cdot\mathbf{I}_n & \mathbf{0}_n\\ \mathbf{0}_n & \rho I\cdot\mathbf{I}_n\end{bmatrix}}_{M_p}+\underbrace{\begin{bmatrix}\widetilde{M}^{u,u} & \widetilde{M}^{u,\phi}\\ \widetilde{M}^{\phi,u} & \widetilde{M}^{\phi,\phi}\end{bmatrix}}_{M_s}\right)}_{M}\begin{bmatrix}\ddot{u}\\ \ddot{\phi}\end{bmatrix} + \underbrace{\begin{bmatrix}\tilde{C}^{u,u} & \tilde{C}^{u,\phi}\\ \tilde{C}^{\phi,u} & \tilde{C}^{\phi,\phi}\end{bmatrix}}_{C_s(=C)}\begin{bmatrix}\dot{u}\\ \dot{\phi}\end{bmatrix} + \\ &\qquad\underbrace{\left(-\underbrace{\begin{bmatrix}FDM_{U1} & FDM_{\phi 1}\\ FDM_{U2} & FDM_{\phi 2}\end{bmatrix}}_{K_p}+\underbrace{\begin{bmatrix}\tilde{K}^{u,u} & \tilde{K}^{u,\phi}\\ \tilde{K}^{\phi,u} & \tilde{K}^{\phi,\phi}\end{bmatrix}}_{K_s}\right)}_{K}\begin{bmatrix}u\\ \phi\end{bmatrix} = F\end{aligned}\tag{5.33}$$

Herein:

- ρ is the material density of the pile.
- A is the area of the pile.
- n is the number of nodes describing the length of the pile (= 41).
- F is the force vector.
- $[\ddot{u} \quad \ddot{\phi}]^T$ is the acceleration vector of u and ϕ.
- $[\dot{u} \quad \dot{\phi}]^T$ is the velocity vector of u and ϕ.
- $[u \quad \phi]^T$ is the displacement vector of u and ϕ.
- $\mathbf{I}_n$ is an identity matrix of n by n.
- $\mathbf{0}_n$ is an zero matrix of n by n.
- FDM_{ii} is defined in equations (5.22) – (5.25) for $ii = U1, U2, \phi 1, \phi 2$, respectively.

Please note that the contribution of the mass and stiffness associated with the soil is much larger than the mass and stiffness associated with the pile. Furthermore, a simplification is made so that the pile itself does not contribute to the total system damping (no structural damping). Given the number of elements in the matrices, not all values of the elements are presented in this thesis. For sake of brevity, the interested reader is referred to appendix D for a visual representation of the matrices.

A Matlab solver for ordinary differential equations (ODE solver) will be used to solve the equations. This function implements a integration function, such as Runge-Kutta method, with variable time steps. The system of equations needs to be reduced from a second order system to a series of first order equations. To simplify the explanation of the method of reducing the order, equation (5.33) is rewritten as:

$$M\ddot{y} + C\dot{y} + Ky = F \tag{5.34}$$

A vector x is created:

$$x1 = y = \begin{bmatrix} u \\ \phi \end{bmatrix} \tag{5.35}$$

$$x2 = \dot{y} = \begin{bmatrix} \dot{u} \\ \dot{\phi} \end{bmatrix}$$

Differentiating yields:

$$\frac{d}{dt}x_1 = \dot{y} = x2 \tag{5.36}$$

$$\frac{d}{dt}x_2 = \ddot{y} = M^{-1}(F - Cx_2 - Kx_1) \tag{5.37}$$

This leaves a system of first order equations which can be integrated using Matlab's ODE solver. Besides the matrices, the solver requires an initial displacement and velocity vector (y_0). It requires a discrete time span for step-wise integration of the system. The discrete time steps are determined by the ODE solver. If a time vector is defined with a fixed step size, the output is generated for at discrete time steps of the vector. Defining the step size only affects the output. The internal step size of the solver is not bound to that vector. Please note the appropriate ODE solver for time-domain computations for an offshore wind turbineis selected in section

5.4.1. FREE VIBRATIONS PILE-SOIL

The numerical stability of 1D time-domain model for the pile-soil system is analysed before adding a superstructure and external loading scenario's. A straight forward approach to check numerical stability in the time domain is computing free vibrations. Free vibrations are oscillations where the total energy stays the same over time if there is no damping present. This means that the amplitude of the vibration stays the same. For a system with damping, the energy is dissipated and the amplitude of displacement should decay and approach zero over time. In case of an unstable system, the amplitude of displacements increase and approach infinity over time. The latter is undesirable and physically incorrect. It would mean that energy is created, which is impossible if there is no energy source.

This section presents results of a free vibration analysis for the pile-soil system. The monopile is given an initial displacement and rotation and, in the absence of external loading, is left to vibrate freely. The initial displacement vector (y_0) is set to the 3D SSI response of the 3D model at 0.3 Hz and BC HS1. This yields a realistic displacement and rotation profile for a pile vibrating in the first mode. The initial velocities are set to zero. The response is calculated for the time range 0 to 2 seconds with interval steps of 0.001 seconds.

Figure 5.5a presents the displacement of the pile head over time and the associated frequency response magnitude spectrum for two systems. The blue line represents the head displacement for a system without soil mass Ms and the red line for a system with soil mass. Figure 5.5b presents that half-power bandwidth method for the system with soil mass. When soil mass is excluded from the computations, the response is overdamped and no vibrations occur. When soil mass is included, the system is heavily damped and the amplitude of displacement decays to zero. For a structure vibrating at a high frequency, the approximated soil mass becomes important. Two methods are applied to find the associated damping ratio:

1. The half-power bandwidth method [40]
2. The method of logarithmic decrement

A rule-of-thumb for the half-power method is that the frequency resolution of the frequency response function should have at least five points within the Δf bandwidth [40]. The following equations are applied:

$$Q = \frac{1}{2\xi} \qquad \xi = \text{damping ratio} \qquad Q = \text{Amplification factor} \tag{5.38}$$

$$Q = \frac{f_n}{\Delta f} \qquad f_n = \text{peak frequency response} \qquad \Delta f = \text{half-power bandwidth}$$

f_n is 4.68 Hz and Δf is 7.66 Hz. Solving the equations yields a damping ratio of 0.81 (= 81%), which is very high. It is likely that the peak and corresponding half-power bandwidth are not well defined, resulting in an overestimation of the damping ratio.

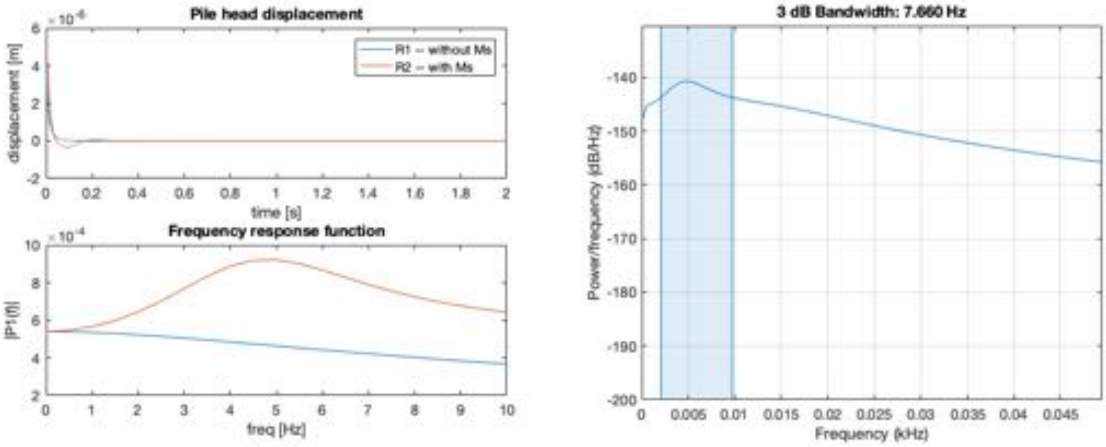

(a)

(b)

Figure 5.5: (a) The top figure presents the displacement of pile head for case HS1, no bedrock. The corresponding frequency magnitude spectrum is shown in the bottom figure. The blue line shows the displacement of the monopile head when soil mass is included. The orange line shows the displacement when soil mass is excluded. Figure (b) presents the half-power bandwidth method for pile head response with soil mass.

Another widely applied method to estimate the damping ratio is called the method of logarithmic decrement δ. The decrement relates the exponential decay between the maxima x_0 and x_n over n periods (see figure 5.6. The logarithmic decrement should be constant for a system. The damping ratio is calculated using equations (5.39).

$$\delta = \frac{1}{n}\ln\left(\frac{x_0}{x_n}\right) \qquad \frac{2\pi\xi n}{\sqrt{1-\xi^2}} = \ln\left(\frac{x_0}{x_n}\right) \qquad \xi = \frac{1}{\sqrt{1+(\frac{2\pi}{\delta})^2}} \tag{5.39}$$

Where n is the number of peaks, ξ is the damping ratio, x_1 is the amplitude of the first peak and x_n is the amplitude of the nth peak. As the decrement should constant for free vibrations, a small modification is proposed to the equations (5.39). Instead of calculating the decrement between the first peak and the nth successive peak, the decrement is calculated for every peak i and the first successive peak $i+1$, resulting in $\delta = \ln\left(\frac{x_i}{x_{i+1}}\right)$

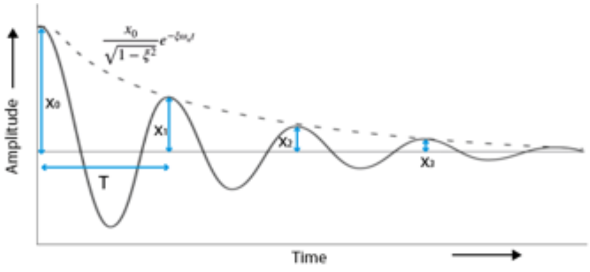

Figure 5.6: Damped free motion starting from rest at an initial displacement x_0

.

Solving equations (5.39) yields figure 5.7. For the first five peaks the damping ratio is constant at 0.51(=51%). After the fifth peak the damping ratio decreases. This is caused by numerical errors as the amplitude becomes smaller $1.5 \cdot 10^{-16}$, while the absolute and relative tolerance limits are respectively set to 10^{-13} and 10^{-14}. Given the constant decrement, this damping ratio seems more plausible than the damping ratio obtained by the half-power bandwidth method.

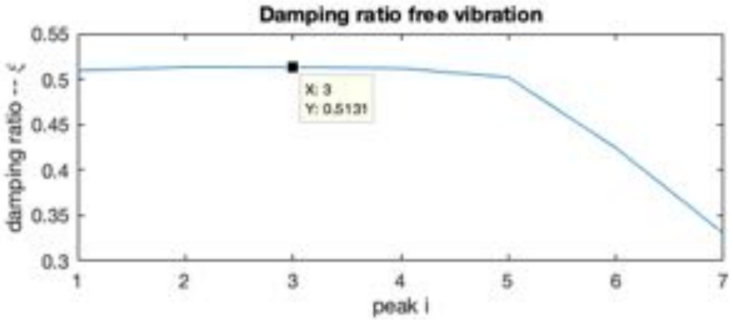

Figure 5.7: Damping ratio of monopile embedded in soil for case HS1 according to the method of logarithmic decrement

The frequency-independent added mass, stiffness and damping coefficient matrices approximation is the most accurate in the low frequency regime. Consequently, the approximation is less accurate at high frequencies. The main purpose of this analysis is to assess the numerical stability of the model. Two conclusions can be drawn. The model is numerically stable and added soil mass becomes important for monopiles embedded in soil.

6

1D APPROXIMATION OF SUPERSTRUCTURE - PILE - SOIL SYSTEM

In this chapter, the time-domain model for the complete system will be developed and time-domain computations are performed for various loading scenarios. A superstructure with turbine is added to the model for a monopile embedded in soil. The procedure is discussed in section 6.1. Section 6.2 describes the hydrodynamic and aerodynamic loading scenarios. Section 6.3 presents the frequency-domain results for a simplified loading scenario. Section 6.4.1 covers free vibrations of the model for a system with, and without, soil mass. This section will mainly be used to estimate the damping ratio related to the soil and to evaluate the numerical stability of model. Section 6.4.2 presents the time response of the time-domain model for the complete system when excited with simplified harmonic loading. This section will be used to analyze whether the system shows realistic behaviour for various harmonic loads. Finally, the time-domain response of the model is presented for realistic hydrodynamic and aerodynamic loading scenarios in section 6.4.3.

6.1. SUPERSTRUCTURE/TURBINE MODELLING

A superstructure with a length of 106 meter is added to the monopile of 20 meter. The total length of the OWT beam is 126 meter. For simplicity, the superstructure is given the same properties in terms of diameter, wall thickness, Young's Modulus, Poisson's ratio, Timoshenko shear constant and material density as the monopile (support structure). The values are listed in table 3.1 and a schematic drawing of the complete structure is shown in figure 6.1. The discretization scheme, as presented in section 5.2.1, is applied to the structure as a whole (monopile and superstructure) with free ends at the tip of the monopile and the head of the superstructure. The entire structure is discretized in uniform discretization steps of 0.5m. A point mass of 350 tons, representing the turbine components (rotor, hub, blades and nacelle), is added at the top of the tower. The tower and the turbine are based on an upwind 3-bladed NREL 5-MW wind turbine [41].

Table 6.1: Used properties of upwind 3-bladed NREL 5-MW wind turbine [41]

Property	Value
Rating	5 MW
Rotor Orientation, Configuration	Upwind, 3 Blades
Control	Variable Speed, Collective Pitch
Rotor, Hub Diameter	126 m, 3 m
Hub Height	90 m
Cut-In, Rated, Cut-Out Wind Speed	3 m/s, 11.4 m/s, 25 m/s
Cut-In, Rated Rotor Speed	6.9 rpm, 12.1 rpm
Rated Tip Speed	80 m/s
Rotor Mass	110,000 kg
Nacelle Mass	240,000 kg
Tower Mass	347,460 kg

Assembling the mass, stiffness and damping matrices and adding the soil coefficient matrices yields figures 6.2a – 6.2c in matrix form. The frequency-domain model from chapter 5 is used to determine the resonance frequency (or, equivalently, the natural frequency) of the model for complete OWT. The mass, stiffness and damping matrices (figure 6.2) are included in the frequency-domain model. A dynamic load of $F(\omega)$ =530 kN is applied to the head of the OWT for increasing frequencies. The resulting OWT head displacement against the excitation frequency is drawn in figure 6.3. The resonance frequency (or, equivalently, the natural frequency) f_n is 0.273 Hz ($\omega_n = 2\pi f_n$=1.71 rad/s).

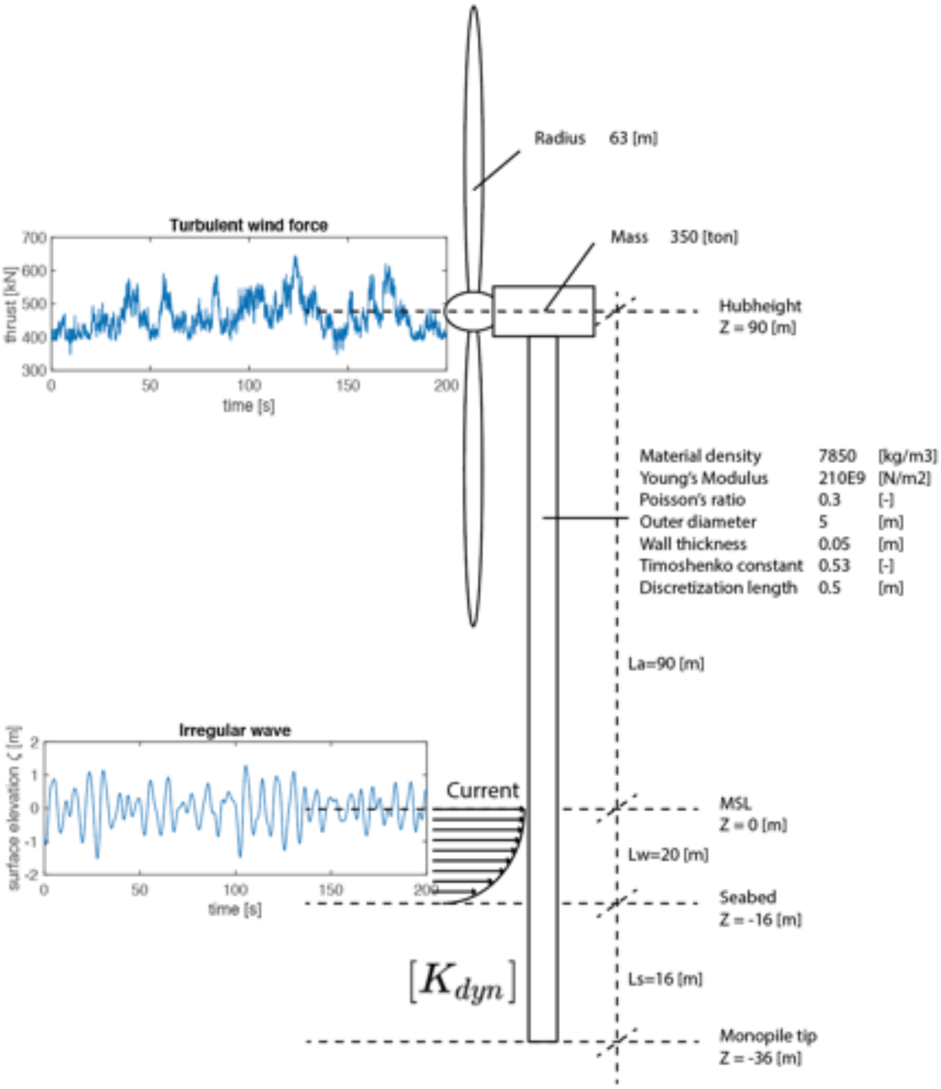
Radius 63 [m]
Mass 350 [ton]
Turbulent wind force
thrust [kN]
700
600
500
400
300
0
50
100
150
200
time [s]
Hubheight
Z = 90 [m]
Material density 7850 [kg/m3]
Young's Modulus 210E9 [N/m2]
Poisson's ratio 0.3 [-]
Outer diameter 5 [m]
Wall thickness 0.05 [m]
Timoshenko constant 0.53 [-]
Discretization length 0.5 [m]
La=90 [m]
Irregular wave
surface elevation ζ [m]
2
1
0
-1
-2
0
50
100
150
200
time [s]
Current
MSL
Z = 0 [m]
Lw=20 [m]
Seabed
Z = -16 [m]
$[K_{dyn}]$
Ls=16 [m]
Monopile tip
Z = -36 [m]

Figure 6.1: Schematic representation of the complete offshore wind turbine model that is subjected to dynamic loading.

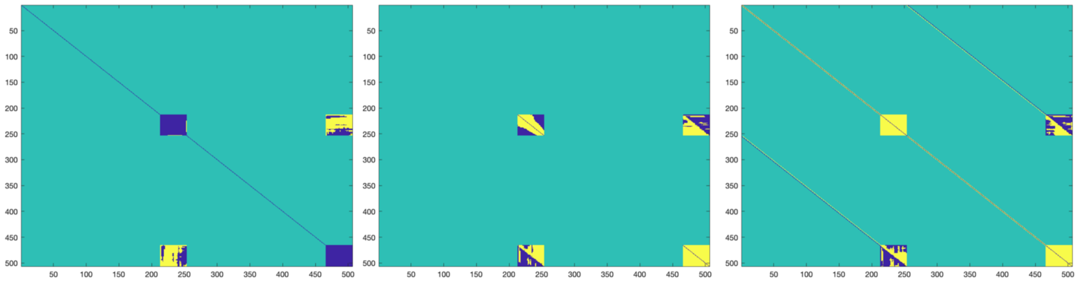

(a) Mass matrix (b) Damping matrix (c) Stiffness matrix

Figure 6.2: Assembled OWT mass, damping and stiffness matrices. The green colour indicates elements with value zero. Positive values are indicated in blue and negative values in yellow. The diagonals in figure a) and c) are positive sign definite.

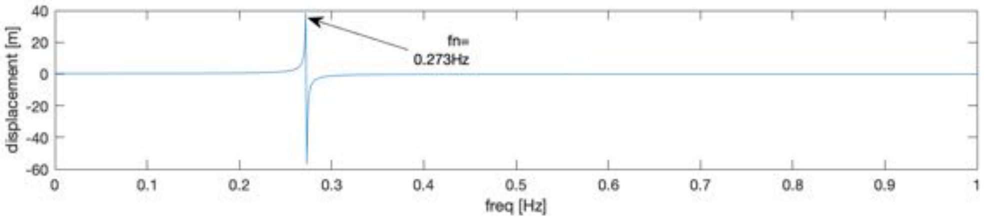

Figure 6.3: full offshore wind turbine head displacement over frequency. The resonance frequency is 0.273 Hz.

6.2. DYNAMIC LOADING ON OWT

6.2.1. TYPES OF LOADS

In this thesis, two types of loads are taken into account – permanent loads and environmental loads.

PERMANENT LOADS

Permanent loads are loads that will not vary in terms of magnitude, direction and position over time. In the simplified model, the considered permanent loads are the mass of the turbine, superstructure and monopile. Hydrostatic pressure is neglected in this thesis.

ENVIRONMENTAL LOADS

Environmental loads are caused by environmental conditions. These loads vary over time. The three most important environmental loads for offshore wind turbines are:

- Wind
- Waves
- Current

Other environmental phenomena that influence the response of an OWT, are earthquakes, temperature, tides, marine growth and snow/ice. The purpose of this thesis is to assess if the non-local method, as proposed by Versteijlen [7], can be applied in the time domain and be subjected to realistic loads. Therefore, only the most important environmental loads (wind, waves and current) are included in the loading scenarios.

6.2.2. HYDRODYNAMIC LOADING

WAVES

A modified Pierson-Moskowitz wave spectrum is developed using an open source Matlab toolbox developed by Fossen and Perez [42]. This toolbox simulates uni-directional waves aligned with the main wind direction for a sea state with significant wave height $H_s = 2$[m] and average wave period $T_0 = 9$ [s]. The derived surface elevation spectrum is shown in figure 6.4a and the corresponding single sided amplitude response spectrum is shown in figure 6.4b .

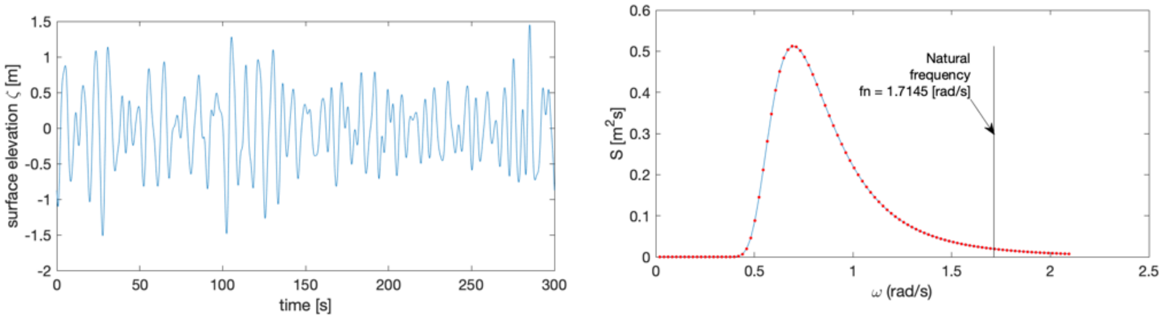

(a) Surface elevation spectrum

(b) Long-crested wave spectrum with 67 harmonic components as red dots

Figure 6.4: Modified Pierson-Moskowitz wave spectrum for $H_s = 2$m and $T_0 = 9$s

The Airy Wave Theory (often referred to as linear wave theory) is the most widely used method to calculate water particle velocities and accelerations due to waves [4]. First needs to be identified whether the water depth can be classified as deep, intermediate or shallow water. This affects which equations can be used to determine the velocities and accelerations. The water particles move in closed orbits that are elliptical for waves in intermediate water depths and circular in deep water, as is shown in figure 6.5.

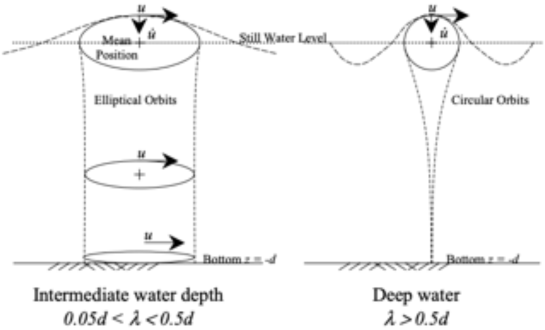

Figure 6.5: particle orbits according to the Airy Wave Theory [4].

The ratio between water depth and wavelength determines, whether the depth is classified as deep or intermediate. The depth is intermediate water depth if:

$$0.05d < \lambda < 0.5d$$

$$0.05 < \frac{d}{\lambda} < 0.5$$

The wavelength (λ) is iteratively calculated by:

$$\lambda = \frac{g}{2\pi} T_0^2 \tanh\left(\frac{2\pi d}{\lambda}\right) \approx 98 \quad [m] \tag{6.1}$$

Where g (= 9.81 m/s^2) is the gravitational constant. The depth over wavelength ratio is 0.16. The offshore wind turbine is placed in intermediate water depth.

Next is determined whether the Airy Wave Theory is valid to calculate the wave particle kinematics. Figure 6.6 shows which wave theorem are applicable for wave steepness and relative depth ratios. The water depth, average wave period and significant wave height are respectively 16m, 9s and 2m. The relative steepness and relative depth are 0.0025 and 0.0201, respectively. This indicates that Stokes' 5^{th} or stream function 3 theories are most applicable. However, for simplicity, the Airy Wave Theory will be applied.

According to the Airy Wave Theory, the horizontal particle velocity and acceleration are calculated by equations (6.2) – (6.3) at an intermediate water depth [43].

$$u_w = \zeta_a \omega \frac{cosh(k(z+d))}{sinh(kd)} sin(\omega t - kx) \tag{6.2}$$

$$\dot{u}_w = -\zeta_a \omega^2 \frac{cosh(k(z+d))}{sinh(kd)} cos(\omega t - kx) \tag{6.3}$$

with:

- ζ_a = wave amplitude [m]
- ω = circular wave frequency [rad/s]
- k = wave number [-]
- d = water depth = 16 [m]
- z = vertical coordinate from still water level, positive upwards [m]
- $\omega t - kx$ = phase angle [rad]

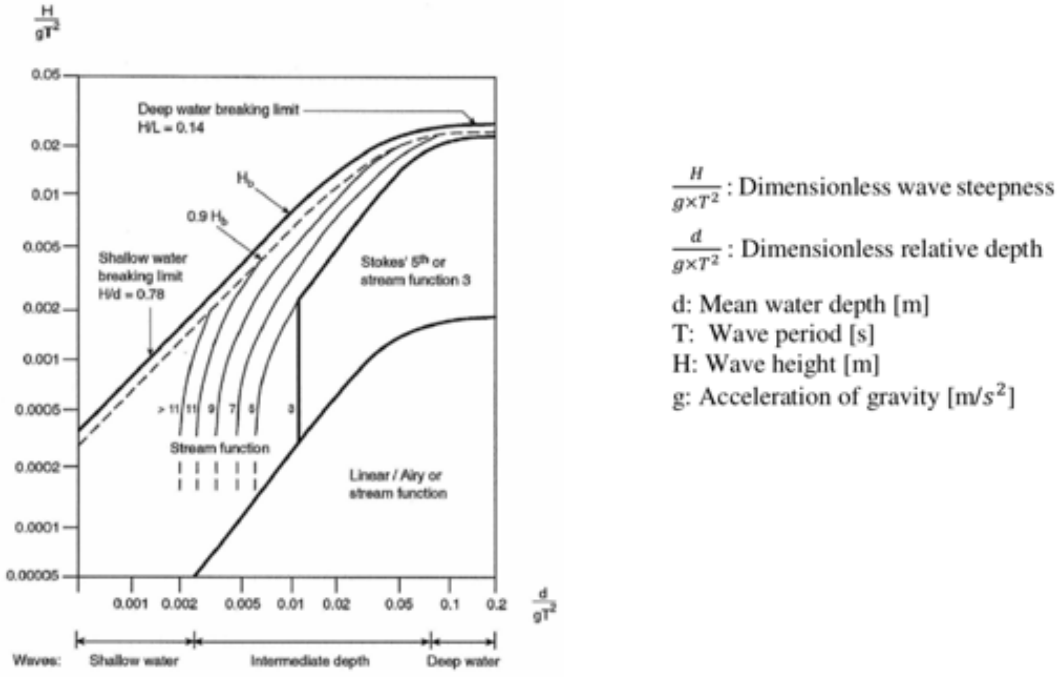

Figure 6.6: Regions of applicability of wave theories [5].

CURRENT

A simplification is made that the current only consists of tidal current. A constant tital current velocity (u_{c0}) of 0.5 m/s at still water level is assumed. The current velocity over the depth profile of the pile is calculated based on the DNV design codes [5] yielding equation (6.4).

$$u_c(z) = u_{c0}\left(\frac{d+z}{d}\right)^{\frac{1}{7}} \tag{6.4}$$

Where u_{c0} is the constant current velocity at still water level.

HYDRODYNAMIC LOADS

The hydrodynamic loads on the structure are calculated with the Morison equation (6.5). The first part of the equation defines the hydrodynamic inertia force and the second part defines the hydrodynamic drag force. The equation takes the relative velocities and accelerations between the pile and wave/current into account and can be included in the time-domain solver.

$$q_W(z,t) = \begin{cases} \frac{1}{4}\pi\rho_w C_M D_o^2(\dot{u}_W(z,t) - \ddot{u}(z,t)) & \text{for } -L_w \leq z \leq 0, \\ \qquad +\frac{1}{2}\rho C_D D_o|u_W(z,t) + u_c(z) - \dot{u}|(u_W(z,t) + u_c(z) - \dot{u}(z,t)) & \\ 0 & \text{for } -L_s - L_w \leq z \leq L_w, \\ 0 & \text{for } 0 \leq z < L_a. \end{cases} \tag{6.5}$$

with:

- ρ_w = water density [kg/m^3]
- D_o = pile outer diameter [m]
- C_M = 2.0 = hydrodynamic inertia coefficient [-][4]
- C_D (=1.0) = hydrodynamic drag coefficient [-][4]
- $\ddot{u}(z,t)$ and $\dot{u}(z,t)$ are depth and time dependent accelerations [m/s^2] and velocities [m/s] of the pile
- $u_c(z)$ = current velocity [m/s]
- L_a = 20 = length of OWT section in soil [m]

- $L_w = 16$ = length of OWT section in water [m]
- $L_a = 90$ = length of OWT section in air [m]

Possibly, a simplification can be made for the hydrodynamic loads. Keulegan and Carpenter [44] determined the dimensionless Keulegan Carpenter number:

$$KC = \frac{u_m T}{d} \tag{6.6}$$

where u_m is the maximum flow velocity in m/s.

This number is commonly used to determine whether drag or inertia loading is dominant. Based on equation (6.2), the maximum flow velocity is 1.37 [m/s]. Filling in the KC equation yields a value of KC = 2.36. For KC<3, the force is inertia dominated, meaning that flow does not travel far enough relative to the pile diameter to generate a significant load [45]. The predominant wave loading is due to inertia loading for OWT support structures. The drag load may be ignored for initial design purposes [4].

6.2.3. AERODYNAMIC LOADING

Wind is one of the most important environmental loads for offshore wind turbines and varies in both direction and speed. The blades in offshore wind turbines translate wind loads in drag and lift forces, where lift forces cause the rotor to rotate and generate energy [46]. The wind loads can be separated in two parts – aerodynamic loads acting on the blades and aerodynamic drag forces acting on the tower (and transition piece). For sake of simplicity, only the aerodynamic loads acting on the blades are taken into account. "Due to the stochastic nature of of the loading environment of offshore wind turbines, currently about 120,000 10-min time-domain (for capturing the nonlinear aeroelastic interaction) simulations are performed for an average design case"[7]. The turbulent and nonlinear properties of wind loading are one of the key reasons for translating the non-local method to the time domain.

Not all kinetic energy from the wind can be translated to mechanical energy. The power coefficient C_p tells how efficiently a turbine converts the wind energy to electricity. The Betz theorem [47] defines that the maximum energy that can be converted by an offshore wind turbine is $C_{p,\text{Betz}} = \frac{16}{27} = 59.26\%$. The maximum power is independent of the wind turbine design in open flow [15].
The mechanical power that the turbine can extract from the wind is a function of wind speed u_{wind} [m/s], rotor speed Ω [rad/s], blade radius R [m] and blade pitch angle β [rad] and can be approximated as:

$$P_w = C_p(\lambda,\beta)\frac{1}{2}\rho_{air}\pi R^2 u_{wind}^3 \qquad [\frac{kg\cdot m^2}{s^3} = W] \tag{6.7}$$

The power curve $C_p(\lambda,\beta)$ is a function of the tip speed ratio λ and the pitch angle β of the blades. The curve is approximated as follows [46]:

$$C_p = 0.73\left(\frac{151}{\lambda_i} - 0.58\beta - 0.002\beta^{2.14} - 13.2)\right)e^{\frac{-18.4}{\lambda_i}} \qquad [-] \tag{6.8}$$

$$\text{with: } \lambda_i = \frac{1}{\frac{1}{\lambda-0.02\theta_p} - \frac{0.0035}{\beta^3+1}}, \qquad \lambda = \frac{\Omega R}{u_{wind}} \tag{6.9}$$

Considering a pitch angle of zero degrees, the maximum power coefficient $C_{p,max} = 0.4412$ at an optimal tip speed ratio of $\lambda_{opt} = 6.9$. A variable pitch controller can be included to optimize the power output of the OWT.

The time-varying aerodynamic loading at the top of the tower due to the operating wind turbine is described by the following equation:

$$T(t) = C_t(t)\left(\frac{1}{2}\rho_{air}\pi R^2|u_{wind}(t) - \dot{u}(z = L_a,t))|\cdot(u_{wind} - \dot{u}(z = L_a,t)\right) \qquad [N] \tag{6.10}$$

Where C_t is the dimensionless thrust coefficient. This coefficient is also a function of the tip speed ratio λ and the collective pitch angle β. The thrust coefficient curve is calculated by a Matlab script made available by keijdener and Arquin Laguna [48] and is presented in appendix E.

A time series of the mean wind speed at hub height is also made available by keijdener and Arquin Laguna [48]. The time series, and corresponding amplitude spectrum, is presented in figure 6.7. The average wind speed for the whole time series is 8 m/s and most energy is concentrated in the low frequency regime.

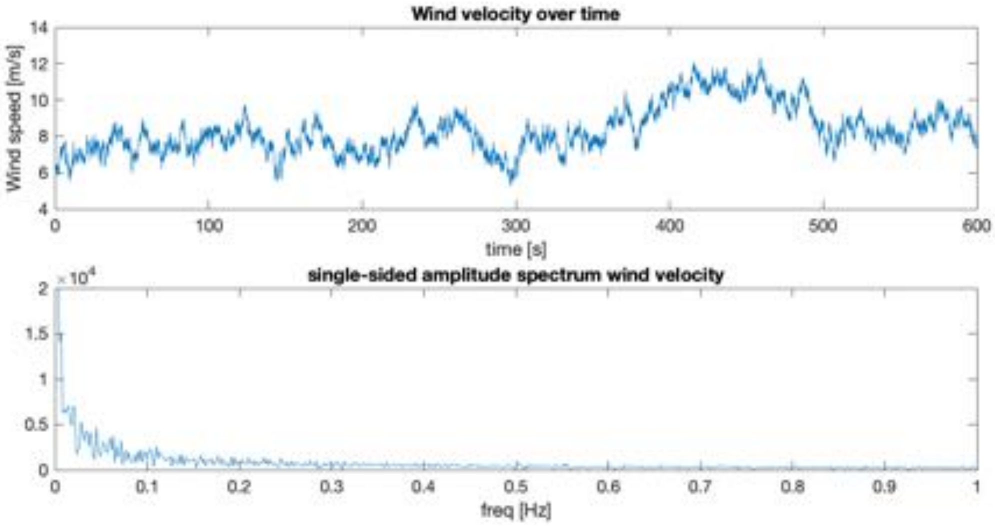

Figure 6.7: Time series of mean wind speed at hub height and corresponding single-sided amplitude spectrum

The power and thrust curves are obtained by means of substituting the mean wind speed time series in equations (6.8), (6.9) and the earlier mentioned Matlab script to determine the thrust coefficient. Figure 6.8 presents the C_p and C_t curves.

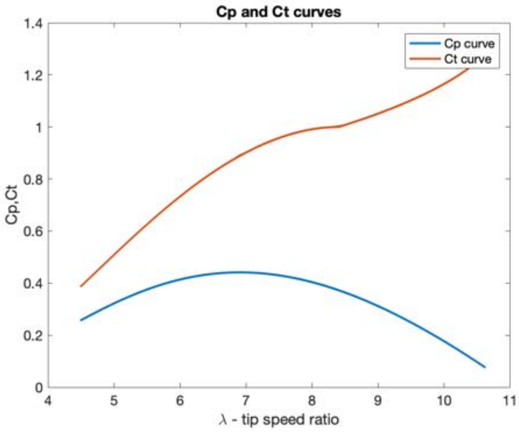

Figure 6.8: Relation between the power coefficient ($C_p[-]$) and thrust coefficient ($C_t[-]$) as a function of the tip speed ratio (λ).

The aerodynamic power and thrust are calculated by substituting C_p and C_t in equations (6.7) and (6.10). The results are presented in figure 6.9. Note that the absolute wind velocity is used to derive the figures. In the time-domain computation the relative velocities between the turbine and wind are taken into account.

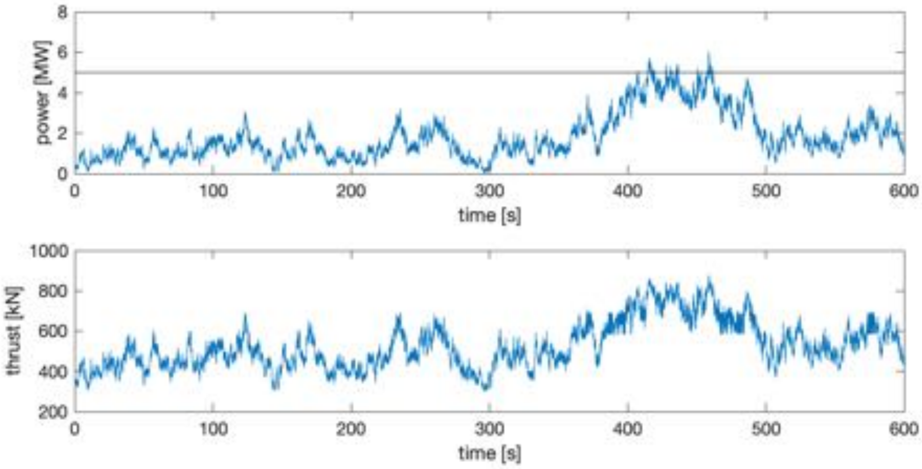

Figure 6.9: Aerodynamic power and thrust as a function of time

6.3. FREQ DOMAIN TOTAL OWT

This section briefly presents the frequency-domain results of the 1D frequency-domain model for the complete OWT. The real and imaginary displacements and rotations are shown f = 0.1, 0.2, 0.3 and 0.4 Hz (ω = 0.63, 1.26, 1.88 and 2.51 rad/s). A dynamic load of$F(\omega)$ = 530kN is applied to the head of the OWT at different excitation frequencies. This load represents the mean wind force acting on the blades at hub-height. The results are presented in figure 6.10.

The response of the OWT is in-phase with the force at frequencies below the resonance frequency of 0.273 Hz and in anti-phase after the resonance frequency is passed. The displacement and rotation profiles at frequencies below resonance frequency represent first mode shapes. The static displacement at the top of the structure for the given load is 0.263 meter. To check if this is realistic a quick semi-analytic check is performed. Two pile sections are considered, the part above the soil and the part below the soil. The part above the soil has an equivalent length L_1 of 106m and the part below of 20m. The displacement of the top section is calculated by equation (6.11). The rotation and displacement at the top of the second section is calculated by applying the force F and a moment of $M_2 = (L_a + L_w)F$ at the head of the monopile embedded in soil (no tower). The rotation and displacement at the top of the section is calculated by equation (6.12). $u_{st} = 0.259 \approx 0.263[m]$, confirming that the static displacement is realistic for this load.

$$u_1 = \frac{FL_1^3}{3EI} = 0.421[m] \tag{6.11}$$

$$u_2, \phi_2 = K^{-1}F \qquad u_2 = 0.0162[m], \quad \phi_2 = -1.67 \cdot 10^{-3}[rad] \tag{6.12}$$

$$u_{st} = u_1 + u_2 + \phi_2 L_1 = 0.259[m] \tag{6.13}$$

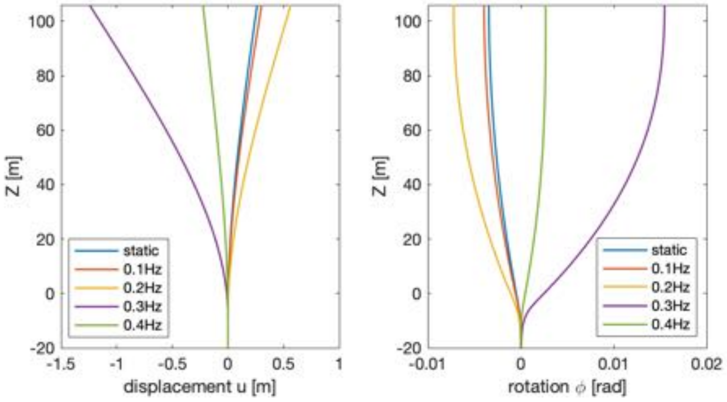

Figure 6.10: Frequency response results for OWT structure when subjected to 530 kN loading at the top of the tower at the frequencies 0, 0.1, 0.2, 0.3 and 0.4 Hz.

6.4. TIME DOMAIN TOTAL OWT

This section presents various results of time-domain computations with the total OWT (soil-monopile-superstructure). Subsection 6.4.1 presents the free vibration results of the OWT. This is used to estimate the damping ratio contribution of the soil and to check the numerical stability of the model for the complete OWT. Subsection 6.4.2 presents the time response of the OWT when subjected to harmonic loads for different frequencies. Finally, in subsection 6.4.3 the time-domain response for the OWT when subjected to realistic aerodynamic and hydrodynamic loads is presented.

6.4.1. FREE VIBRATIONS OWT

This section presents free vibration results of the time-domain model for the OWT. The initial displacement and rotation vector is calculated by approximating the static displacements and rotations of the OWT structure at a force of 530 [kN] applied at the head of the OWT.

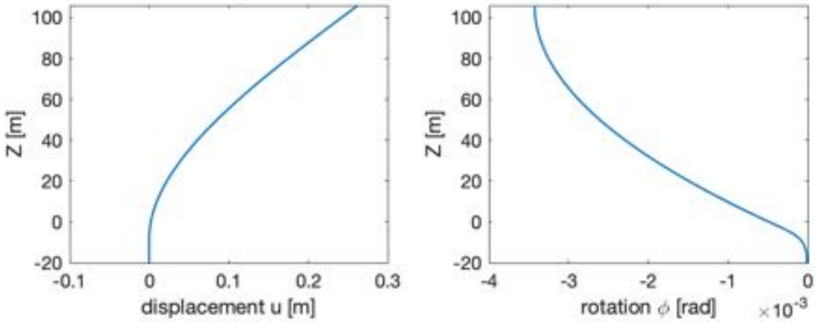

Figure 6.11: Initial displacement (left figure) and rotation (right figure) profile for the OWT at a static excitation of of 530 [kN] applied at the top of the OWT.

It is concluded before that including added mass of the soil in the system of general equations is unlikely to yield a significant contribution to the global system response. To finalize this statement, the free vibration analysis is performed for two cases: with (R2), and without (R1), the soil mass coefficient matrix.
An initial attempt to solve the system using Matlab's most commonly used $ode45$ solver, showed to be to computationally heavy. For systems with very low damping, stiff systems, other solvers are available: $ode15s$, $ode23s$, $ode23t$ or $ode23tb$. Large deviations are are observed in the damping ratio of the OWT when different solvers are applied. A probable cause is that some solvers add numerical damping to the system. Given the low damping of the system, a small addition in damping can have a large effect.

There are two available solvers that can solve stiff systems without adding numerical damping: $ode23t$ and $ode23tb$. Both solvers produce the same results and show convergence for decreasing time steps. This confirms that they operate as expected. Figure 6.12 presents the resulting free vibration for the fully assembled offshore wind turbine for two cases – without (R1), and with (R2), added mass of the soil. The corresponding single sided amplitude spectrum is presented in figure 6.13 and has been computed by a Fast Fourier Transform (FFT).

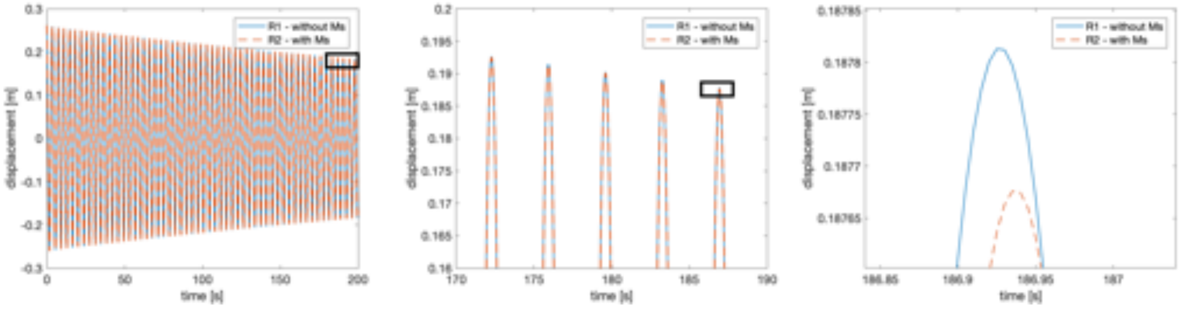

Figure 6.12: Free vibrations for full OWT structure for case R1 and R2. The pile head displacement over time is shown in the three figures, from which the most right figure shows a single peak in high detail. The initial displacement and rotation profile is shown in figure 6.11 and the velocities are set to zero. The initial conditions are applied to R1 and R2.

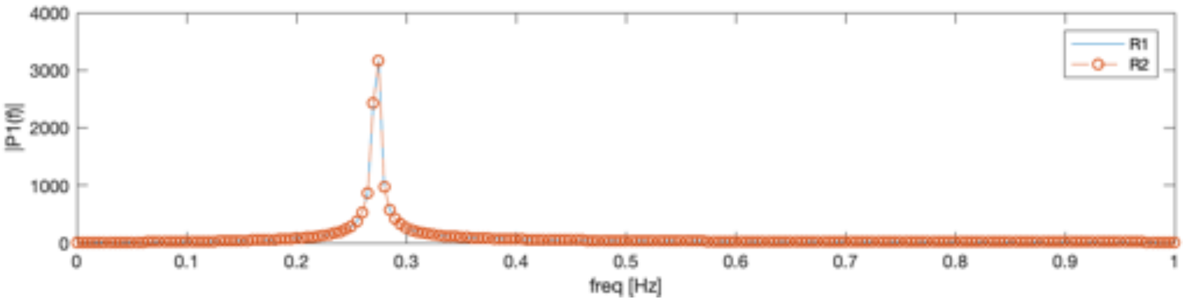

Figure 6.13: Single sided amplitude spectrum.

Figures 6.12 and 6.13 make clear that including the added soil mass matrix does not have a significant effect on the free vibrations of the OWT. Both responses are almost exactly the same and vibrate at 0.273 Hz (1.714 rad/s). A difference is only recognized after magnifying a single peak. The right figure of figure 6.12 shows that R1 damps out slightly slower than R2. This may be caused by numerical inaccuracy of the solver. For offshore wind applications can be concluded that the real part of the dynamic stiffness may be assumed to be frequency independent, and equal to the static value.

The damping ratio of the model of the OWT is estimated next. The total system damping consists only of soil damping in absence of structural damping, aerodynamic damping, hydrodynamic damping and numerical damping. The half-power bandwidth can be applied if the bandwidth of the peak in the frequency response can be described by at least 5 nodes [40]. Given the frequency discretization used in this analysis, this condition is not met as the peak is very steep and is only defined by a couple nodes. The method of logarithmic decrement δ can be applied. The procedure is described in section 5.4.1. The damping ratio is calculated by equations (5.39). Solving the decrement equations for 50 successive peaks yields figure 6.14.

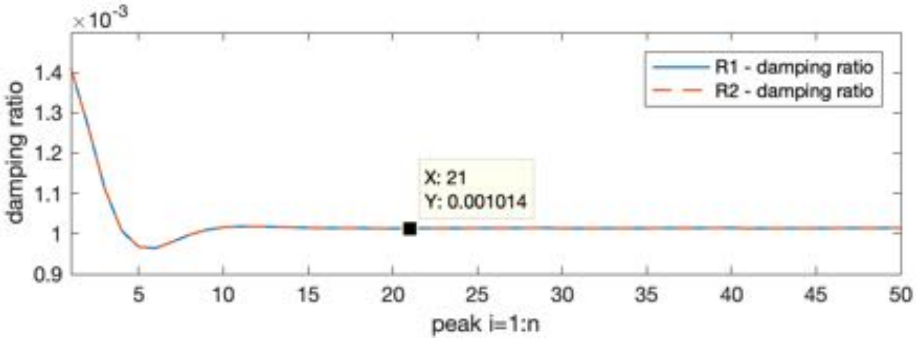

Figure 6.14: Damping ratio's as derived using the method of logarithmic decrement for case R1 and R2

Some oscillations are required to reach convergence in the damping ratio. This is caused by higher frequency content that is dissipated more rapidly until the point that the structure starts oscillating at its first mode and damps out monotonically. After ten oscillations the system vibrates at the natural frequency and the damping ratio becomes constant. The damping ratio is 0.001 (=0.1%) for both R1 and R2. This ratio seems to be on the low side, as according to Arany *et al.* [3], the damping ratio of the soil should be found in the range 0.44–1.0% for offshore wind applications. However, Versteijlen [7] used a similar soil stratigraphy and yields a similar damping ratio. The low damping ratio can be caused by the stiff nature of the soil profile limiting displacements and therefore energy dissipation [7]. Additionally yields the low natural frequency of the system a low damping ratio, as the damping is linear dependent on the frequency of vibration. Moreover, the decision to assign 2% material damping to each soil layer seems to be on the conservative side. Literature indicates that damping ratio's of 3-4 % are not uncommon. A material damping ratio (assigned to the soil layers) of a factor two larger can potentially drastically increase the damping of the numerical model. Finally, nonlinear soil properties, such as gap forming, age hardening or installation effects can also affect the damping ratio of the the model for the complete OWT. The sensitivity of the damping ratio to a higher material damping ratio, a softer soil stratigraphy and a higher natural frequency (shorter tower) requires further assessment. The stiffness, mass and damping matrices are calculated by the 3D model for three scenarios:

1. Material damping ratio (η) = 0.04 (=4%).
2. The depth dependent Young's Modulus ($E(z)$) is divided by a factor two.
3. The tower length is reduced to set the natural frequency to approximately 0.3 Hz.

The results of these modifications are presented in figures:

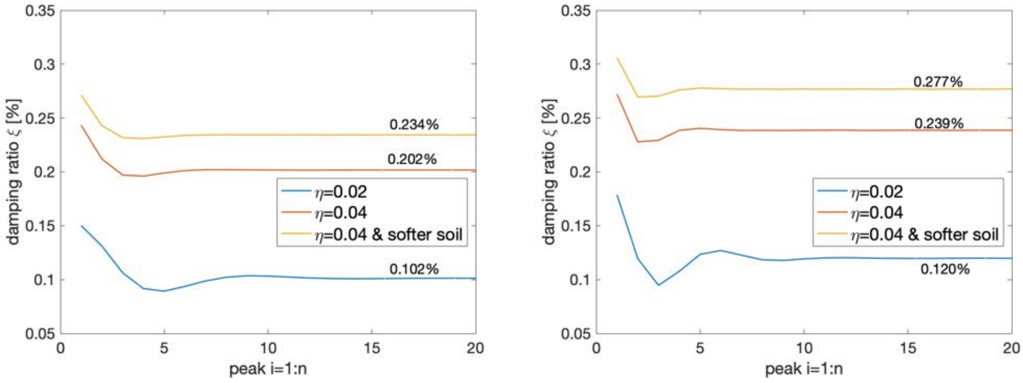

(a) Damping ratios of the OWT for f_n=0.27 hz (b) Damping ratios of the OWT for f_n=0.30 hz

Figure 6.15: Effect of material damping ratio, soil stiffness and natural frequency to OWT damping ratio related to the soil. The stiffness and damping matrix are calculated for BC HS1.

Figure 6.15a presents the resulting damping ratio's for an OWT vibrating at $f_n = 0.27[Hz]$ in percentages. The blue line in figure 6.15a represents the damping ratio of the OWT as presented in figure 6.14, i.e. the base case. The red line represents the damping ratio of the OWT when 4% material damping ($\eta = 0.04$) is assigned to the soil layers. Multiplying the material damping ratio by a factor two yields almost a doubling of the OWT damping ratio ξ from 0.102% to 0.0202%. The yellow line shows the damping ratio of the OWT for $\eta = 0.04$ and a softer soil stratigraphy (Young's Modulus: $E(z) = E(z)/2$). The softer soil increases the damping ratio by 15%. Figure 6.15b presents the resulting damping ratio's for an OWT vibrating at $f_n = 0.30[Hz]$. The damping ratio is very sensitive to the natural frequency of the OWT. Increasing the natural frequency by 10% yields an increase of approximately 20% in the damping ratio. The soil damping ratio is very sensitive to the natural frequency of the OWT and the material damping ratio. The damping ratio of the soil associated with a softer soil stratigraphy and a material damping ratio of 4% is more in line with damping ratio's found in literature.

6.4.2. HARMONICALLY FORCED VIBRATIONS – OWT

This section presents time-domain results for the OWT when subjected to a step load ($F(t) = F_0$ for: $t > 0$) and harmonic loading ($F(t) = F_0\sin(\omega t)$ with a magnitude (F_0) of 528.6 kN applied at the OWT head at different excitation frequencies. This load is estimated by substituting the mean wind speed of 8.34 m/s, which is equal to the mean wind speed over the first 600 seconds from the spectrum presented in figure 6.7, in equation (6.10). The initial conditions are set to zero – the structure starts at rest. The force vector is presented below:

$$\underline{F} = [528.6 \cdot 10^5 \sin(\omega t) \quad 0 \quad 0 \quad 0 \quad \dots \quad 0]^T$$

The resulting OWT head displacements are presented for a step load and harmonic loads at 0.1, 0.2, 0.3, 0.4 and 0.5 Hz (or 0.628, 1.257, 1.885, 2.513 and 3.142 rad/s) in figure 6.16. An initial observation is that the responses look logical and that the vibration patterns are a result of both excitation frequencies and the natural frequency of the system. All responses are stable and there are no outliers present. The magnitude of displacements are within the range of expectations. The response to the step load converges smoothly from two times the static equilibrium to the equilibrium (u_{static} = 0.262m) over time. The static equilibrium is computed by the frequency-domain model from chapter 5.

Excitation frequencies close to the natural frequency cause amplification of the system. At 0.3 Hz a phenomenon called $beating$ is present. The vibrations beat with a long period that is inverse proportional to the difference between the loading frequency ω in rad/s and natural frequency ω_n in rad/s, i.e. $T = 1/|0.3 - 0.273| = 37[s]$. The middle graph in figure 6.16 shows the response for harmonic loading at 0.1 Hz. In the work of Akin [49], an offshore wind turbine, with a natural frequency of 0.28 Hz, was modelled and excited with harmonic wave loading at 0.1 Hertz using $FLEX5$. The shape of his results correlate strongly with the results as presented in the top figure.

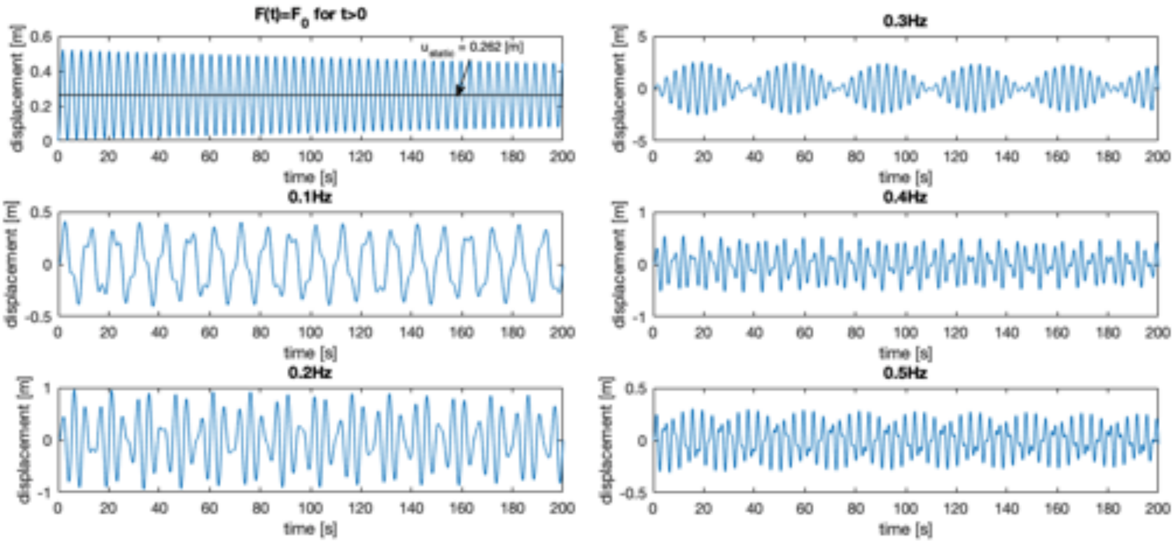

Figure 6.16: OWT head response for a realistic step load ($F(t) = F_0$ for: $t > 0$) in the top left hand side figure and harmonic loads of $F(t) = F_0\sin(\omega t)$ in the other figures. $F_0 = 526.8[kN]$. The excitation frequencies are indicated above each figure. The mass starts at the equilibrium ($u(0) = 0$ and $\dot{u}(0) = 0$). The time series is 150 seconds. The structure starts at rest in $t = 0$ (i.e. initial conditions are set to zero).

To gain more confidence that the responses are correctly modelled, the responses are compared with a single degree of freedom system (SDOF) without damping. Given the low damping ratio of the OWT with only soil damping, this assumption is acceptable. The mass is initially at rest in the equilibrium position of the system (i.e. $u(t=0) = 0$ and $u(\dot{t} = 0) = 0$). The following procedure is followed to determine the total solution:

$$F = F_0\sin(\omega t) \qquad [N] \qquad (6.14)$$

$$k = F_0/u_{static} = 526.8/0.262 = 201 \qquad [kN/m] \qquad (6.15)$$

$$\omega_n = \sqrt{k/m} = 1.7142 \qquad [rad/s] \qquad (6.16)$$

$$m = k/\omega_n^2 = 6.843 \cdot 10^5 \qquad [kg] \qquad (6.17)$$

$$u(t) = \frac{F_0}{k}\frac{1}{1-\omega^2/\omega_n^2}(\sin(\omega t) - \frac{\omega}{\omega_n}\sin(\omega_n t)) \qquad [m] \qquad (6.18)$$

Equation (6.18) is used to calculate the SDOF response to harmonic loading. The results are presented in figure 6.17. Herein, both the OWT head responses and SDOF approximations are shown a step load and harmonic loading scenarios.

The results in figure 6.17 indicate that the OWT head response and the SDOF approximation are almost identical. Only for step loading is a small deviation present for large t-values. This is caused by the absence of damping in the SDOF approach. It is concluded that, assuming that the input parameters are correctly determined, the solution of the numerical analysis with the OWT is correctly calculated in the time domain. The model is verified by the SDOF results.

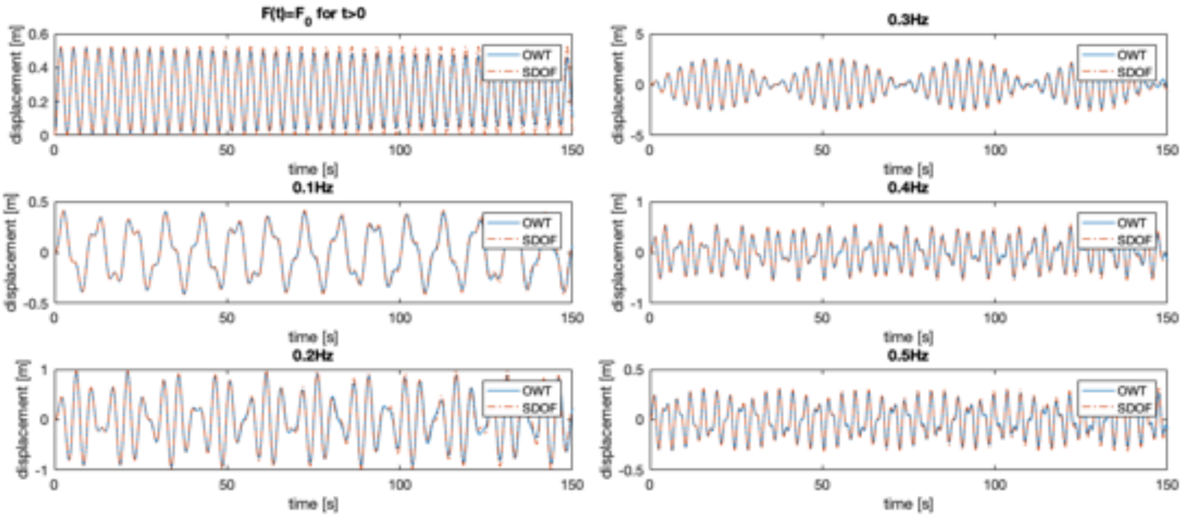

Figure 6.17: Comparison OWT head displacement and SDOF approximation for realistic step load ($F(t) = F_0$ for: $t > 0$) and harmonic loads of $F(t) = F_0\sin(\omega t)$. The excitation frequency is indicated above each figure. The mass starts at the equilibrium ($u(0) = 0$ and $\dot{u}(0) = 0$). The time series is 150 seconds.

6.4.3. FORCED VIBRATIONS – OWT

This section presents the results for the hydrodynamic and aerodynamic loading scenario's. Four cases are considered:

- C1 - OWT response due to hydrodynamic loading (waves and current).
- C2 - OWT response due to Aerodynamic loading.
- C3 - OWT response due to combined hydrodynamic and aerodynamic loading.
- C4 - Summed response due to hydrodynamic and aerodynamic loading.

The static equilibrium of the OWT for the mean loading over the first 300 seconds is 0.227m. This equilibrium is lower than the value that was presented in the previous section. The reason is that the wind velocity increases after 300 seconds as indicated in figure 6.7. It is expected that the response to aerodynamic and combined loading is concentrated around this equilibrium. Figure 6.18 presents the time-domain results for the OWT when subjected the different loading scenarios and the corresponding single sided amplitude spectra.

If the system is excited without slowly increasing the load, the maximum displacement is about two times the static equilibrium. In reality there will not be an instant force from the wind. To get a more realistic response of an OWT in operating conditions, the initial displacement and rotations of the OWT are set to the static equilibrium for C1 and C3 loading. The initial velocity and rotational velocity vectors are set to zero. In case of hydrodynamic loading (C2), all initial conditions are set to zero.

The aerodynamic force acting on the blades is the dominant force with a maximum displacement of the OWT head of 0.41 meters (figure 6.18a). This is considered no surprise as the area on which the wind acts on is large compared to the surface area on which the waves act on (i.e. $F(t)_{wind} >> F(t)_{waves+current}$). The mean displacement of the OWT head is 0.2333m, which is approximately equal to the static equilibrium u_{static}. The relative velocity between the wind and OWT head are taken to calculate the wind force. This means that aerodynamic damping is included in the computation. Most energy is stored around the first natural frequency and near zero hertz (static).

Figure 6.18b presents the OWT head displacement over time for the hydrodynamic loading scenario (current and waves) with $H_s = 2[m]$ and $T_0 = 9[s]$. Some amplification is present as the natural frequency of the model for the OWT is close to the frequency spectrum of waves (figure 6.4b). However, most of the frequency content of the wave loading is concentrated around 0.1 Hz and causes no amplification. The maximum OWT head displacement is 0.157m. The effect of current ($u_c = 0.5[m/s]$) is negligible as the static equilibrium of hydrodynamic loading is situated at zero displacement. Most energy is stored around the first natural frequency which is indicated by the sharp peak in the frequency spectrum (right hand side figure).

Figure 6.18c presents the OWT head response due to combined wave, current and wind loading. Clearly the largest contribution to the response comes from the aerodynamic loads, which is the dominant force. The response is approximately the same as 6.18a. This justifies the conclusion that the contribution of wave loads to the OWT head response is small. The mean head displacement of 0.2335m is equal to the mean displacement caused by only wind loading. The single sided amplitude spectrum of combined loading is also almost exactly the same as 6.18a. This confirms again that the contribution of hydrodynamic loading to the total system response is limited.

It is interesting to compare the OWT head response of combined loading versus the summed response of aerodynamic and hydrodynamic loading. Both responses are shown in figure 6.18d. Aerodynamic damping reduces the amplitude of displacement of the combined loading scenario, where in the summed response it only dampens the response to aerodynamic loading. The joint action of aerodynamic and hydrodynamic loading is beneficial in terms of OWT head response over time. When the separate responses to aerodynamic and hydrodynamic loading are summed, the amplitude of displacement is much larger than the response to combined loading. This is also confirmed by the single sided amplitude spectrum for both cases. The summed response shows a much sharper peak at the natural frequency of the system, indicating that amplification at the natural frequency is present.

A great achievement in this thesis is that the computational time of the time-domain computations is very low. It only takes two minutes to simulate the OWT response subjected to hydrodynamic and turbulent aerodynamic loading for 200 seconds. The computational effort can be reduced by increasing the discretization length and thus reducing the dimensions of the model.

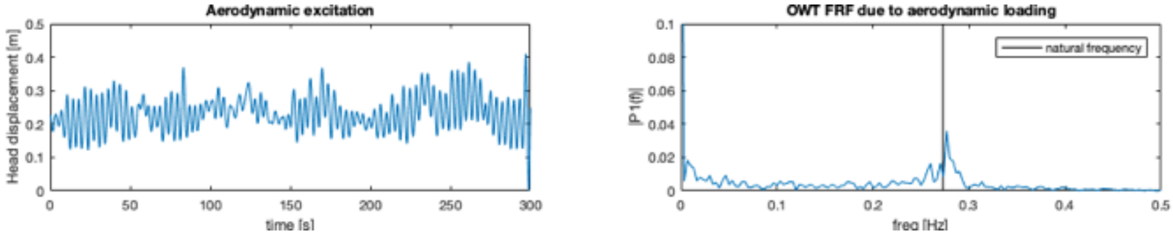

(a) Response to turbulent aerodynamic loading

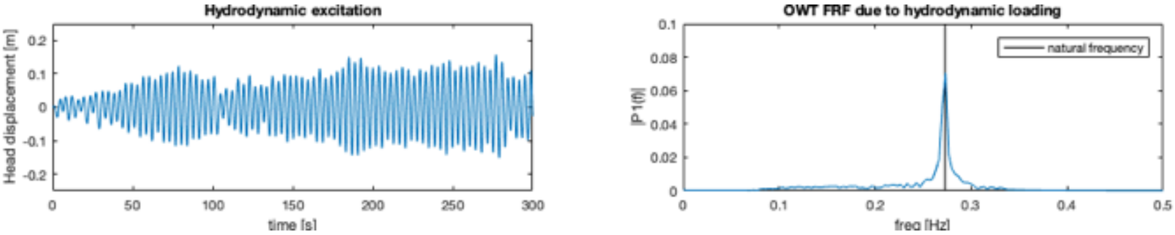

(b) Response to hydrodynamic (waves and current) loading

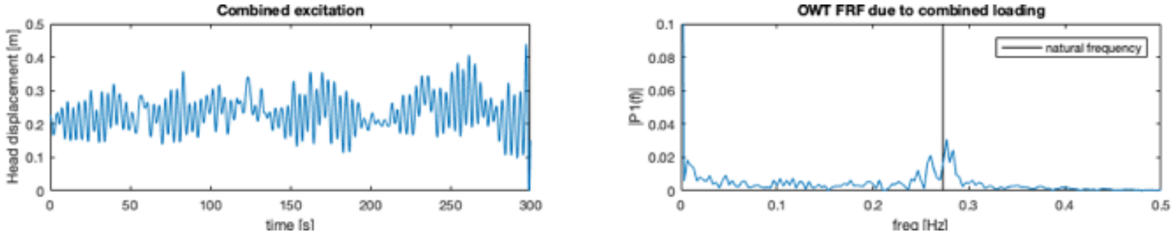

(c) Response to combined aerodynamic and hydrodynamic loading

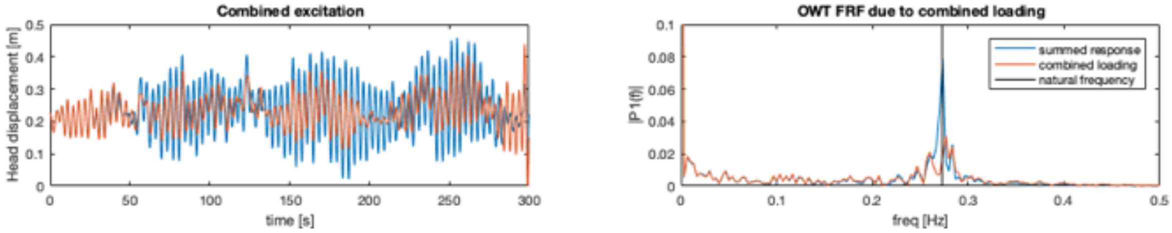

(d) Summed response of aerodynamic and hydrodynamic loading (6.18a+6.18b)

Figure 6.18: Time-domain results for OWT when subjected to different loading scenarios over a time series of 300 seconds. From (a) to (d) the left figures show the OWT head displacement over time for C1, C2, C3 and C4, respectively. The right hand size figures show the corresponding single sided amplitude spectra. The spectrum is derived translating the OWT head response to the frequency domain by means of Fast Fourier Transform (FFT). The spectra are normalized with the sampling number. The natural frequency of the OWT is indicated with the vertical black line at 0.27 Hz

7

CONCLUSIONS & RECOMMENDATIONS

7.1. CONCLUSIONS

This thesis endeavoured to develop a computationally efficient 1D time-domain model to calculate the soil-structure interaction (SSI) response an offshore wind turbine (OWT) on a non-local Winkler foundation. A novel method is applied to extract 3D frequency-dependent dynamic stiffness kernels from a 3D linear-elastic finite elements model. An incentive for this research is found in discrepancies between measured natural frequencies and natural frequencies calculated in initial design of installed offshore wind turbines. A literature review identified that uncertainties in SSI modelling between rigidly behaving large diameter piles and soil is a probable cause.

In the offshore wind industry, SSI is commonly modelled as a 1D local Winkler foundation with local non-linear elastic springs to represent the lateral soil stiffness. The stiffness is often based on the $p-y$ curve methods, considering semi-empirical relations between the lateral displacement of the pile and the soil pressure. This method is developed for flexible piles and is based on a limited number of tests. This method does not capture all reaction mechanisms related to large diameter rigidly behaving piles in soil. These piles experience a more global (non-local) reaction of the soil, where flexible piles experience a local reaction of the soil.

A 3D linear-elastic (LE) finite element model is used to compute 1D frequency-dependent global (non-local) complex-valued dynamic soil stiffness, which captures the coupled 3D reactions of soil to the pile. The frequency dependence of the dynamic soil stiffness is analysed for two sets of boundary conditions in an heterogeneous soil stratigraphy. The boundary conditions consist of soft half-space and stiff half-space, representing bedrock. The real part of the dynamic stiffness behaves near statically in the low frequency regime. A near parabolic frequency-dependent part is identified. The extent of this frequency dependence is very low. The imaginary part of the dynamic stiffness is linear frequency dependent and is governed by material damping in the soil. Small depth-dependent resonances are observed in the real and imaginary part of the dynamic soil stiffness if the soil stratigraphy overlays a stiff layer (bedrock). These resonances are present at frequencies above the cut-off frequency.

The complex-valued frequency-dependent dynamic soil stiffness kernels are approximated by frequency-independent coefficient matrices for added mass, damping and stiffness, which can be included in a 1D time-domain model. The transformation into the time domain is important since it allows the user to incorporate irregular wave, turbulent nonlinear wind loading and air-turbine interaction effects that are considered to have a major impact on the resulting dynamic system response. It is concluded that the accuracy of the approximation in representing the dynamic soil stiffness is very good in the frequency range of interest for offshore wind. The approximation of added mass is valid for frequencies below the cut-off frequency if a stiff layer is present in the soil domain. The contribution of added mass to the real part of the dynamic stiffness is very low. The approximation is more accurate in representing dynamic stiffness of a soil continuum with a stiff half-space (until the first resonance frequency) than a soil continuum with a soft half-space. It is expected that this is caused by small numerical errors in the absorbing layers in the soft half-space.

A pile-soil system is modelled as a 1D Timoshenko beam model on a non-local Winkler foundation in the frequency domain. This model is based on the non-local method of Versteijlen [7]. Misfit functions are used to compare the SSI response of the 1D model with the 3D SSI response to dynamic loading scenarios. The overall match between the SSI responses is very good with misfits in the region of 2%. Including added mass in the equations of motion yields a significant improvement in the misfit of the imaginary-valued response for a small trade-off in the misfit of the real-valued response. However, in the frequency range of interest for offshore wind, the effect of added mass to the SSI response can be neglected.

The model is translated to the time domain and the equations of motion are solved by an ordinary differential equation solver (ODE solver) in Matlab. It is concluded that the model is numerically stable and that added mass becomes important for the stiff pile-soil system vibrating at high frequencies.

As a last step, a superstructure and a turbine, with realistic dimension of a NREL 5-MW wind turbine, are integrated with the monopile in the 1D SSI time-domain model. This results in a 1D time-domain model for a fully integrated offshore wind turbine. Time-domain computations are performed for free vibrations, harmonic loading and realistic aero-/hydrodynamic loading scenarios. Special care needs to be taken in selecting the proper ODE solver. A solver is selected that specialized in solving stiff (low damping) systems without adding numerical damping to the model. The free vibration analysis justifies the conclusion that the real part of the dynamic stiffness can be assumed frequency independent and equal to the static value for offshore wind applications. A damping ratio of 0.1% is calculated by the method of logarithmic decrement. This is on the low side considering literature. A sensitivity analysis concludes that the damping ratio is very sensitive to the natural frequency of the model, the material damping ratio assigned to the soil layers and the stiffness of the soil stratigraphy. The SSI response to harmonic loading is verified with a single degree of freedom system. An almost exact match is observed, which justifies the conclusion that model structure is correctly modelled. When considering the SSI response to environmental loading, the dominant force acting on the OWT is aerodynamic loading. The response of the OWT to combined aerodynamic and hydrodynamic loading is beneficial, when compared to the summed response to separate aerodynamic and hydrodynamic loading. The maximal OWT head displacement and vibration amplitudes are lower when combined loading is considered. The effect of air-turbine interaction generates damping, which is more pronounced in the combined loading scenario.

The time-domain model is computationally very efficient in predicting the time-domain SSI response of an offshore wind turbine for varying loading scenarios, while incorporating the coupled 3D reactions of the soil to the pile. The model can be used by the offshore wind industry for initial design purposes.

7.2. LIMITATIONS

Though this thesis has demonstrated the potential of using time-domain representations of dynamic soil stiffness to capture soil-structure interaction, they do possess some limitations.

A linear-elastic finite elements model is used to calculate the complex-valued dynamic soil stiffness. In reality the soil reacts in a nonlinear way when loaded. Pile installation effects, gap-separation and hardening/softening of the soil for cyclic loading are neglected in this thesis. The assumption that soil behaves like a linear-elastic material holds for small-strain displacements. However, for larger displacement, and more extensive design purposes, these effects need to be taken into account.

Frequency dependent soil materail damping is assumed to match the damping mechanisms between the 3D and 1D models. Alternative damping mechanisms are not explored in this thesis.

The frequency dependence of dynamic soil stiffness is, for the largest part, assessed for a single heterogeneous soil stratigraphy. The effect of differences in soil stratigraphies is not well captured in this thesis.

The misfit between the dynamic stiffness and approximated added mass, stiffness and damping coefficient matrices is larger for BC HS1 than for BC HS2. This is unexpected because no resonances are present if BC HS1 is applied. In addition, the estimation of added mass by the 3D model for this boundary condition showed unexpected behaviour. It is expected that this is caused by small numerical errors related to the formulation

of the PMLs.
The performance of the 1D model is assessed by means of comparing the 1D SSI response with the 3D SSI response. It is assumed that the 3D model produces realistic results. However, the validity of the 3D model is not analysed. Consequently, the 3D model could have be errors in the 3D model, these errors are included in the dynamic soil stiffness and can affect the results of the analysis for frequency dependence.

The time-domain SSI response is only computed for the 1D model on a non-local Winkler foundation. Consequently, no remarks can be made about the differences in terms of stiffness and natural frequencies between the non-local Winkler foundation and other foundation models (such as the $p-y$ curve method).

Finally, a model is always a simplification of the system that is represented by it. Assumptions and simplifications are made to reduce the complexity of the model. Consequently, a distinction must be made between the true behaviour and the modelled behaviour. For example, resonances are observed in the real part of the dynamic stiffness when the soil continuum overlays a stiff layer at a finite depth. It is most likely that these resonances are a direct consequence of the modelling method, rather than physical phenomena.

7.3. RECOMMENDATIONS

Considering the 3D model, it is recommended to validate the 3D model with alternative linear-elastic finite element models. The PML formulation needs to be re-evaluated, because it seems to under-estimate the frequency dependent part of the dynamic soil stiffness. Furthermore, it is recommended to examine the effect of nonlinear behaviour (gap-forming, cyclic hardening and installation effects) in soil to the dynamic stiffness.

It is advised to examine the performance of the non-local method with frequency-independent coefficient matrices for difference soil stratigraphies, with, amongst others, different material damping ratio's. In addition, it is recommended to compare the SSI model response with other models that are based on, amongst others, $p-y$ curves.

The SSI response for an offshore wind turbine on a non-local Winkler foudnation is only calculated for The simplistic loading scenarios. It is interesting to include other types of loading, such as ice-loading and earthquake excitations.

A

SOIL STRATIGRAPHY

Table A.1: Soil stratigraphies

			S1 (heterogeneous soil)			S2 (homogeneous soil)			2-Layered soil		
Layer [-]	Z_{in} [m]	Z_{out} [m]	ρ_s [kg/m^3]	E [MPa]	ν [-]	ρ_s [kg/m^3]	E [MPa]	ν [-]	ρ_s [kg/m^3]	E [MPa]	ν [-]
1	0	-1	1937	45	0.25	1984	316	0.25	1984	50	0.25
2	-1	-2	1937	20	0.25	1984	316	0.25	1984	50	0.25
3	-2	-3	1295	10	0.412	1984	316	0.25	1984	50	0.25
4	-3	-4	1733	30	0.304	1984	316	0.25	1984	50	0.25
5	-4	-5	2039	90	0.25	1984	316	0.25	1984	50	0.25
6	-5	-6	2039	240	0.25	1984	316	0.25	1984	316	0.25
7	-6	-7	2039	402	0.25	1984	316	0.25	1984	316	0.25
8	-7	-8	2039	505	0.25	1984	316	0.25	1984	316	0.25
9	-8	-9	2039	400	0.25	1984	316	0.25	1984	316	0.25
10	-9	-10	2039	430	0.25	1984	316	0.25	1984	316	0.25
11	-10	-11	2039	300	0.25	1984	316	0.25	1984	316	0.25
12	-11	-12	2039	530	0.25	1984	316	0.25	1984	316	0.25
13	-12	-13	2039	545	0.25	1984	316	0.25	1984	316	0.25
14	-13	-14	2039	640	0.25	1984	316	0.25	1984	316	0.25
15	-14	-15	2039	295	0.25	1984	316	0.25	1984	316	0.25
16	-15	-16	2039	360	0.25	1984	316	0.25	1984	316	0.25
17	-16	-17	2039	405	0.25	1984	316	0.25	1984	316	0.25
18	-17	-18	2039	330	0.25	1984	316	0.25	1984	316	0.25
19	-18	-19	2039	332	0.25	1984	316	0.25	1984	316	0.25
20	-19	-20	1916	335	0.34	1984	316	0.25	1984	316	0.25
21	-20	-21	1774	280	0.346	1984	316	0.25	1984	316	0.25
22	-21	-22	2039	415	0.25	1984	316	0.25	1984	316	0.25
23	-22	-23	2039	377	0.25	1984	316	0.25	1984	316	0.25
24	-23	-24	2039	377	0.25	1984	316	0.25	1984	316	0.25
25	-24	-25	2039	337	0.25	1984	316	0.25	1984	316	0.25
26	-25	-26	2039	610	0.25	1984	316	0.25	1984	316	0.25
27	-26	-27	2039	337	0.25	1984	316	0.25	1984	316	0.25
28	-27	-28	2039	372	0.25	1984	316	0.25	1984	316	0.25
29	-28	-29	2039	420	0.25	1984	316	0.25	1984	316	0.25
30	-29	-30	2039	537	0.25	1984	316	0.25	1984	316	0.25
31	-30	-80	2039	460	0.25	1984	316	0.25	1984	316	0.25

B

FIT BETWEEN 3D STIFFNESS AND APPROXIMATED COEFFICIENTS

B.1. FIT BETWEEN ELEMENTS

Figure B.1 and B.1 presents the polynomial estimation cost functions in matrix from as presented in chapter 4.5. The diameter is varied. Figure B.1 presents the results for $D_o = 3[m]$ and B.2 for $D_o = 7[m]$. The magnitude of the frequency dependent parts of the dynamic stiffness summed over the frequency range 0–0.5 Hz is presented in the left column. The second column shows the local contribution of misfit to the total matrix misfit (eq. (4.12) – (4.13)). Finally, the third column presents the local misfit ratio as calculated by equations (4.10) – (4.11).

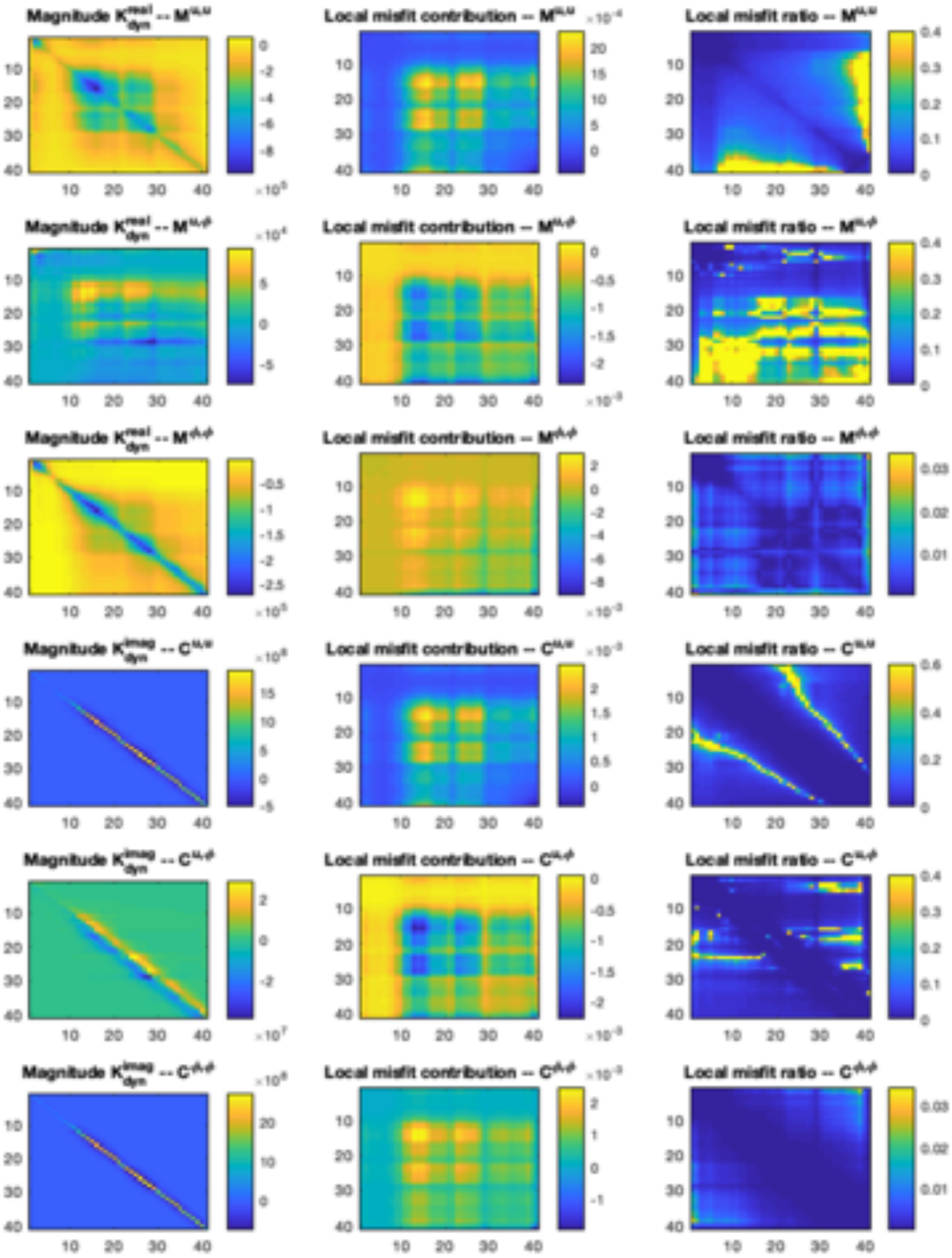

Figure B.1: For case HS1 and diameter of 3 meter. Visual representation of misfits for mass and damping matrices. The left column shows the summed magnitude over frequency for the elements in the dynamic stiffness matrices. The middle column presents the contribution of local misfit to the total misfit (eq: (4.10)–(4.11)). In the last column the local ratio is presented as calculated by eq. (4.10)–(4.11)

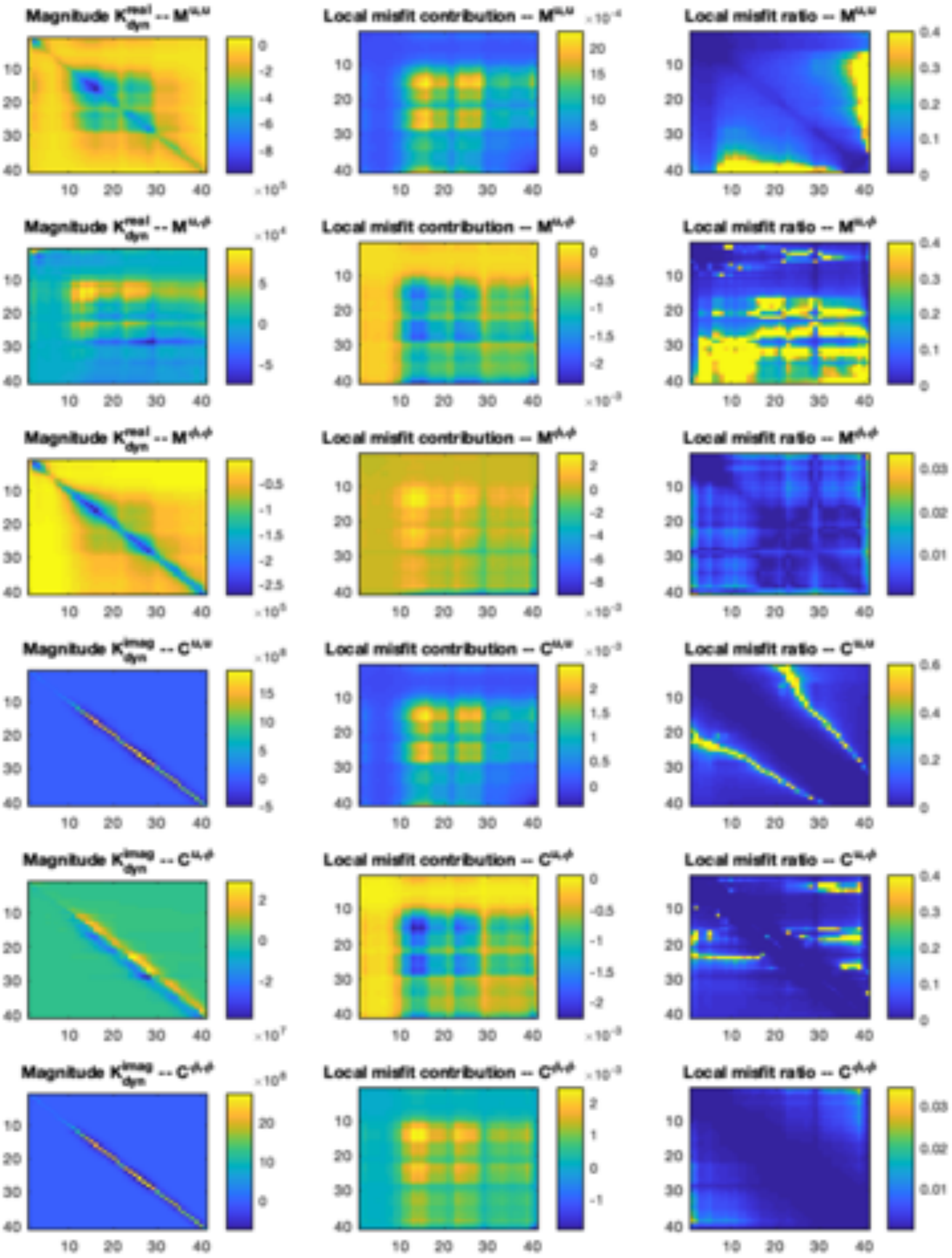

Figure B.2: For case HS1 and diameter of 7 meter. Visual representation of misfits for mass and damping matrices. The left column shows the summed magnitude over frequency for the elements in the dynamic stiffness matrices. The middle column presents the contribution of local misfit to the total misfit (eq: (4.10)–(4.11)). In the last column the local ratio is presented as calculated by eq. (4.10)–(4.11)

C

MISFIT 3D–1D SSI RESPONSE

C.1. GENERAL EQUATIONS

$$-\rho A\omega^2\mathbf{I}_n \begin{bmatrix} u_1 \\ u_2 \\ \vdots \\ u_{n-1} \\ u_n \end{bmatrix} + FDM_{U1} \begin{bmatrix} u_1 \\ u_2 \\ \vdots \\ u_{n-1} \\ u_n \end{bmatrix} - \widetilde{K}^{u,u}_{i,j} \begin{bmatrix} u_1 \\ u_2 \\ \vdots \\ u_{n-1} \\ u_n \end{bmatrix} + FDM_{\phi1} \begin{bmatrix} \phi_1 \\ \phi_2 \\ \vdots \\ \phi_{n-1} \\ \phi_n \end{bmatrix} - \widetilde{K}^{u,\phi}_{i,j} \begin{bmatrix} \phi_1 \\ \phi_2 \\ \vdots \\ \phi_{n-1} \\ \phi_n \end{bmatrix} = \begin{bmatrix} -\frac{2F}{h} + \frac{GA\kappa M}{EI} \\ 0 \\ \vdots \\ 0 \\ 0 \end{bmatrix} = F1 \tag{C.1}$$

$$-\rho I\omega^2\mathbf{I}_n \begin{bmatrix} \phi_1 \\ \phi_2 \\ \vdots \\ \phi_{n-1} \\ \phi_n \end{bmatrix} + FDM_{U2} \begin{bmatrix} u_1 \\ u_2 \\ \vdots \\ u_{n-1} \\ u_n \end{bmatrix} - \widetilde{K}^{\phi,u}_{i,j} \begin{bmatrix} u_1 \\ u_2 \\ \vdots \\ u_{n-1} \\ u_n \end{bmatrix} + FDM_{\phi2} \begin{bmatrix} \phi_1 \\ \phi_2 \\ \vdots \\ \phi_{n-1} \\ \phi_n \end{bmatrix} - \widetilde{K}^{\phi,\phi}_{i,j} \begin{bmatrix} \phi_1 \\ \phi_2 \\ \vdots \\ \phi_{n-1} \\ \phi_n \end{bmatrix} = \begin{bmatrix} F + \frac{2M}{h} \\ 0 \\ \vdots \\ 0 \\ 0 \end{bmatrix} = F2 \tag{C.2}$$

Herein: $\widetilde{K}^{ii,jj}_{i,j} = -\omega^2 M^{ii,jj}_{i,j} + i\omega C^{ii,jj}_{i,j} + K^{ii,jj}_{i,j}$ for $ii = u,\phi \quad , \quad jj = u,\phi \quad , \quad i = 1:N$ and $j = 1:N$.

$$\underbrace{\left(\underbrace{\begin{bmatrix} -\rho A\omega^2\mathbf{I}_n + FDM_{U1} & FDM_{\phi1} \\ FDM_{U2} & -\rho I\omega^2\mathbf{I}_n + FDM_{\phi2} \end{bmatrix}}_{B_p} - \underbrace{\begin{bmatrix} \widetilde{K}^{u,u}_{i,j} & \widetilde{K}^{u,\phi}_{i,j} \\ \widetilde{K}^{\phi,u}_{i,j} & \widetilde{K}^{\phi,\phi}_{i,j} \end{bmatrix}}_{B_s} \right)}_{B} \begin{bmatrix} u \\ \phi \end{bmatrix} = \begin{bmatrix} F1 \\ F2 \end{bmatrix} \tag{C.3}$$

C.2. CASES

- $R1:$ 1^{st} order system without added mass: $B_s = (i\omega C + K)$
- $R2:$ 2^{nd} order system: $B_s = -\omega^2 M + i\omega C + K$
- $R3:$ 3^{th} order system with higher order damping term : $B_s = -\omega^2 M + i\omega(C - \omega^2 C_3) + K$
- $R4:$ Directly extracted complex dynamic stiffness from 3D model: $B_s = K_{direct3D}$

C.3. RESULTS – TABLES

	Error between fit 3D and 1D											
	0 Hz			0.3 Hz			0.6 Hz			0.9 Hz		
Case	C_{tot}	C_u	C_ϕ	C_{tot}	C_u	C_ϕ	C_{tot}	C_u	C_ϕ	C_{tot}	C_u	C_ϕ
$R4\,\Re$	0.0194	0.0154	0.0040	0.0192	0.0152	0.0040	0.0186	0.0147	0.0039	0.0178	0.0140	0.0038
$R4\,\Im$	NaN	NaN	NaN	0.0270	0.0179	0.0091	0.0296	0.0201	0.0095	0.0327	0.0226	0.0101
$R3\,\Re$	0.0225	0.0174	0.0051	0.0223	0.0172	0.0051	0.0221	0.0171	0.0050	0.0221	0.0172	0.0049
$R3\,\Im$	NaN	NaN	NaN	0.0258	0.0162	0.0096	0.0327	0.0226	0.0102	0.0358	0.0245	0.0113
$R2\,\Re$	0.0225	0.0174	0.0051	0.0223	0.0172	0.0051	0.0221	0.0171	0.0050	0.0224	0.0175	0.0049
$R2\,\Im$	NaN	NaN	NaN	0.0269	0.0173	0.0096	0.0371	0.0268	0.0103	0.0452	0.0335	0.0117
$R1\,\Re$	0.0225	0.0174	0.0051	0.0208	0.0159	0.0049	0.0165	0.0122	0.0043	0.0106	0.0066	0.0040
$R1\,\Im$	NaN	NaN	NaN	0.0218	0.0102	0.0102	0.0446	0.0137	0.0137	0.0719	0.0217	0.0217

Table C.1: Case HS1: Real and imaginary misfits between 3D response and approximated response for the frequencies 0 – 0.3 – 0.6 – 0.9 Hz

	Error between fit 3D and 1D											
	1.5 Hz			2.0 Hz			2.5 Hz			3.0 Hz		
Case	C_{tot}	C_u	C_ϕ	C_{tot}	C_u	C_ϕ	C_{tot}	C_u	C_ϕ	C_{tot}	C_u	C_ϕ
$R4\,\Re$	0.0157	0.0122	0.0035	0.0149	0.0109	0.0040	0.0160	0.0111	0.0049	0.0194	0.0140	0.0053
$R4\,\Im$	0.0405	0.0279	0.0126	0.0484	0.0320	0.0164	0.0570	0.0352	0.0218	0.0642	0.0364	0.0279
$R3\,\Re$	0.0237	0.0191	0.0046	0.0265	0.0221	0.0044	0.0298	0.0251	0.0047	0.0345	0.0276	0.0069
$R3\,\Im$	0.0331	0.0168	0.0164	0.0406	0.0164	0.0241	0.0672	0.0327	0.0345	0.0935	0.0501	0.0434
$R2\,\Re$	0.0264	0.0218	0.0047	0.0369	0.0320	0.0048	0.0565	0.0499	0.0065	0.0841	0.0708	0.0133
$R2\,\Im$	0.0554	0.0370	0.0183	0.0555	0.0277	0.0279	0.0672	0.0303	0.0369	0.0956	0.0573	0.0383
$R1\,\Re$	0.0211	0.0113	0.0098	0.0377	0.0206	0.0171	0.0544	0.0309	0.0235	0.0653	0.0395	0.0258
$R1\,\Im$	0.1903	0.1331	0.0572	0.2784	0.1807	0.0977	0.3558	0.2151	0.1407	0.4070	0.2295	0.1775

Table C.2: Case HS1: Real and imaginary misfits between 3D response and approximated response for the frequencies 1.5 – 2.0 – 2.5 – 3.0 Hz

	Error between fit 3D and 1D											
	0 Hz			0.3 Hz			0.6 Hz			0.9 Hz		
Case	C_{tot}	C_u	C_ϕ	C_{tot}	C_u	C_ϕ	C_{tot}	C_u	C_ϕ	C_{tot}	C_u	C_ϕ
$R4\,\Re$	0.0200	0.0159	0.0040	0.0198	0.0158	0.0040	0.0191	0.0152	0.0039	0.0179	0.0141	0.0038
$R4\,\Im$	NaN	NaN	NaN	0.0152	0.0065	0.0087	0.0153	0.0063	0.0090	0.0189	0.0093	0.0096
$R3\,\Re$	0.0231	0.0179	0.0052	0.0229	0.0178	0.0051	0.0222	0.0171	0.0050	0.0207	0.0159	0.0048
$R3\,\Im$	NaN	NaN	NaN	0.0172	0.0078	0.0094	0.0193	0.0097	0.0097	0.0337	0.0234	0.0104
$R2\,\Re$	0.0231	0.0179	0.0052	0.0229	0.0177	0.0051	0.0222	0.0171	0.0050	0.0206	0.0158	0.0048
$R2\,\Im$	NaN	NaN	NaN	0.0173	0.0079	0.0094	0.0173	0.0077	0.0096	0.0279	0.0176	0.0103
$R1\,\Re$	0.0231	0.0179	0.0052	0.0216	0.0166	0.0049	0.0170	0.0127	0.0044	0.0105	0.0066	0.0040
$R1\,\Im$	NaN	NaN	NaN	0.0169	0.0070	0.0099	0.0321	0.0197	0.0123	0.0637	0.0460	0.0177

Table C.3: Case HS2, bedrock at 50m: Real and imaginary misfits between 3D response and approximated response for the frequencies 0 – 0.3 – 0.6 – 0.9 Hz

	Error between fit 3D and 1D											
	1.5 Hz			2.0 Hz			2.5 Hz			2.8 Hz		
Case	C_{tot}	C_u	C_ϕ	C_{tot}	C_u	C_ϕ	C_{tot}	C_u	C_ϕ	C_{tot}	C_u	C_ϕ
$R4\,\Re$	0.0143	0.0107	0.0036	0.0166	0.0121	0.0045	0.0162	0.0112	0.0050	0.0182	0.0129	0.0052
$R4\,\Im$	0.1252	0.0812	0.0440	0.1080	0.0641	0.0439	0.0582	0.0360	0.0222	0.0621	0.0363	0.0258
$R3\,\Re$	0.0198	0.0156	0.0042	0.0520	0.0479	0.0040	0.1182	0.1128	0.0054	0.1961	0.1841	0.0119
$R3\,\Im$	0.1330	0.1154	0.0176	0.1565	0.1222	0.0344	0.1228	0.0653	0.0574	0.1137	0.0568	0.0569
$R2\,\Re$	0.0186	0.0144	0.0042	0.0438	0.0398	0.0040	0.0812	0.0767	0.0045	0.1025	0.0953	0.0072
$R2\,\Im$	0.1154	0.0984	0.0170	0.1208	0.0886	0.0322	0.0982	0.0442	0.0540	0.1408	0.0849	0.0559
$R1\,\Re$	0.0312	0.0212	0.0100	0.0407	0.0225	0.0182	0.0594	0.0343	0.0251	0.0658	0.0397	0.0261
$R1\,\Im$	0.2225	0.1733	0.0491	0.3170	0.2248	0.0922	0.3898	0.2459	0.1439	0.4165	0.2485	0.1679

Table C.4: Case HS2, bedrock at 50m: Real and imaginary misfits between 3D response and approximated response for the frequencies 1.5 – 2.0 – 2.5 – 2.8 Hz

C.4. RESULTS – FIGURES

	Error between fit 3D and 1D											
	1.5 Hz			2.0 Hz			2.5 Hz			2.8 Hz		
Case	C_{tot}	C_u	C_ϕ	C_{tot}	C_u	C_ϕ	C_{tot}	C_u	C_ϕ	C_{tot}	C_u	C_ϕ
$R4\,\Re$	0.0196	0.0156	0.0040	0.0193	0.0154	0.0040	0.0184	0.0145	0.0039	0.0177	0.0139	0.0038
$R4\,\Im$	NaN	NaN	NaN	0.0152	0.0065	0.0087	0.0217	0.0125	0.0092	0.0352	0.0252	0.0101
$R3\,\Re$	0.0228	0.0176	0.0052	0.0225	0.0174	0.0051	0.0213	0.0163	0.0050	0.0245	0.0197	0.0048
$R3\,\Im$	NaN	NaN	NaN	0.0173	0.0079	0.0094	0.0579	0.0481	0.0097	0.1291	0.1179	0.0112
$R2\,\Re$	0.0228	0.0176	0.0052	0.0225	0.0174	0.0051	0.0212	0.0162	0.0050	0.0239	0.0192	0.0048
$R2\,\Im$	NaN	NaN	NaN	0.0172	0.0078	0.0094	0.0466	0.0369	0.0097	0.1007	0.0897	0.0111
$R1\,\Re$	0.0228	0.0176	0.0052	0.0209	0.0160	0.0049	0.0156	0.0112	0.0044	0.0103	0.0063	0.0040
$R1\,\Im$	NaN	NaN	NaN	0.0186	0.0086	0.0099	0.0681	0.0556	0.0125	0.1516	0.1323	0.0194

Table C.5: Case HS2, bedrock at 100m: Real and imaginary misfits between 3D response and approximated response for the frequencies 0 – 0.3 – 0.6 – 0.9 Hz

	Error between fit 3D and 1D											
	1.5 Hz			2.0 Hz			2.5 Hz			2.8 Hz		
Case	C_{tot}	C_u	C_ϕ	C_{tot}	C_u	C_ϕ	C_{tot}	C_u	C_ϕ	C_{tot}	C_u	C_ϕ
$R4\,\Re$	0.0159	0.0123	0.0036	0.0148	0.0109	0.0039	0.0161	0.0112	0.0049	0.0178	0.0125	0.0053
$R4\,\Im$	0.0409	0.0281	0.0128	0.0483	0.0319	0.0164	0.0570	0.0352	0.0218	0.0615	0.0361	0.0254
$R3\,\Re$	0.0655	0.0608	0.0046	0.1737	0.1667	0.0069	0.0269	0.0208	0.0061	0.0411	0.0330	0.0081
$R3\,\Im$	0.1920	0.1664	0.0256	0.5533	0.5015	0.0517	0.8686	0.7672	0.1015	0.6254	0.5249	0.1006
$R2\,\Re$	0.0531	0.0486	0.0045	0.0898	0.0850	0.0048	0.1126	0.1074	0.0052	0.1750	0.1696	0.0054
$R2\,\Im$	0.0443	0.0226	0.0217	0.2715	0.2503	0.0212	0.4638	0.4368	0.0271	0.1429	0.0802	0.0627
$R1\,\Re$	0.0171	0.0077	0.0094	0.0347	0.0186	0.0162	0.0529	0.0307	0.0222	0.0620	0.0378	0.0242
$R1\,\Im$	0.2365	0.1776	0.0589	0.3050	0.2085	0.0965	0.3715	0.2339	0.1376	0.3996	0.2391	0.1605

Table C.6: Case HS2, bedrock at 100m: Real and imaginary misfits between 3D response and approximated response for the frequencies 1.5 – 2.0 – 2.5 – 2.8 Hz

	Error between fit 3D and 1D											
	1.5 Hz			2.0 Hz			2.5 Hz			2.8 Hz		
Case	C_{tot}	C_u	C_ϕ	C_{tot}	C_u	C_ϕ	C_{tot}	C_u	C_ϕ	C_{tot}	C_u	C_ϕ
$R4\,\Re$	0.0195	0.0155	0.0040	0.0191	0.0151	0.0040	0.0186	0.0147	0.0039	0.0178	0.0140	0.0038
$R4\,\Im$	NaN	NaN	NaN	0.0194	0.0105	0.0089	0.0313	0.0218	0.0095	0.0322	0.0221	0.0101
$R3\,\Re$	0.0226	0.0175	0.0052	0.0222	0.0171	0.0051	0.0263	0.0213	0.0050	0.0384	0.0335	0.0049
$R3\,\Im$	NaN	NaN	NaN	0.0172	0.0077	0.0095	0.0377	0.0273	0.0105	0.1087	0.0969	0.0118
$R2\,\Re$	0.0226	0.0175	0.0052	0.0222	0.0171	0.0051	0.0266	0.0217	0.0050	0.0431	0.0382	0.0049
$R2\,\Im$	NaN	NaN	NaN	0.0192	0.0097	0.0095	0.0588	0.0484	0.0104	0.0428	0.0309	0.0120
$R1\,\Re$	0.0226	0.0175	0.0052	0.0201	0.0151	0.0049	0.0162	0.0118	0.0043	0.0112	0.0072	0.0040
$R1\,\Im$	NaN	NaN	NaN	0.0300	0.0200	0.0100	0.1069	0.0932	0.0137	0.1279	0.1057	0.0222

Table C.7: Case HS2, bedrock at 200m: Real and imaginary misfits between 3D response and approximated response for the frequencies 0 – 0.3 – 0.6 – 0.9 Hz

	Error between fit 3D and 1D											
	1.5 Hz			2.0 Hz			2.5 Hz			2.8 Hz		
Case	C_{tot}	C_u	C_ϕ	C_{tot}	C_u	C_ϕ	C_{tot}	C_u	C_ϕ	C_{tot}	C_u	C_ϕ
$R4\,\Re$	0.0151	0.0116	0.0035	0.0165	0.0122	0.0043	0.0160	0.0111	0.0049	0.0178	0.0125	0.0052
$R4\,\Im$	0.1095	0.0649	0.0446	0.1031	0.0601	0.0430	0.0571	0.0352	0.0218	0.0618	0.0362	0.0255
$R3\,\Re$	0.0457	0.0414	0.0042	0.0786	0.0746	0.0040	0.0543	0.0497	0.0046	0.0359	0.0289	0.0070
$R3\,\Im$	0.4127	0.3990	0.0137	0.0909	0.0536	0.0373	0.2304	0.1696	0.0609	0.2587	0.1883	0.0704
$R2\,\Re$	0.0227	0.0186	0.0042	0.1378	0.1338	0.0040	0.0826	0.0783	0.0043	0.0563	0.0499	0.0064
$R2\,\Im$	1.1143	1.0982	0.0161	0.1378	0.0955	0.0423	0.2910	0.2242	0.0668	0.3111	0.2349	0.0762
$R1\,\Re$	0.0178	0.0084	0.0094	0.0349	0.0186	0.0162	0.0525	0.0302	0.0223	0.0606	0.0366	0.0240
$R1\,\Im$	0.2113	0.1552	0.0561	0.2941	0.1980	0.0962	0.3631	0.2248	0.1383	0.3936	0.2325	0.1611

Table C.8: Case HS2, bedrock at 200m: Real and imaginary misfits between 3D response and approximated response for the frequencies 1.5 – 2.0 – 2.5 – 2.8 Hz

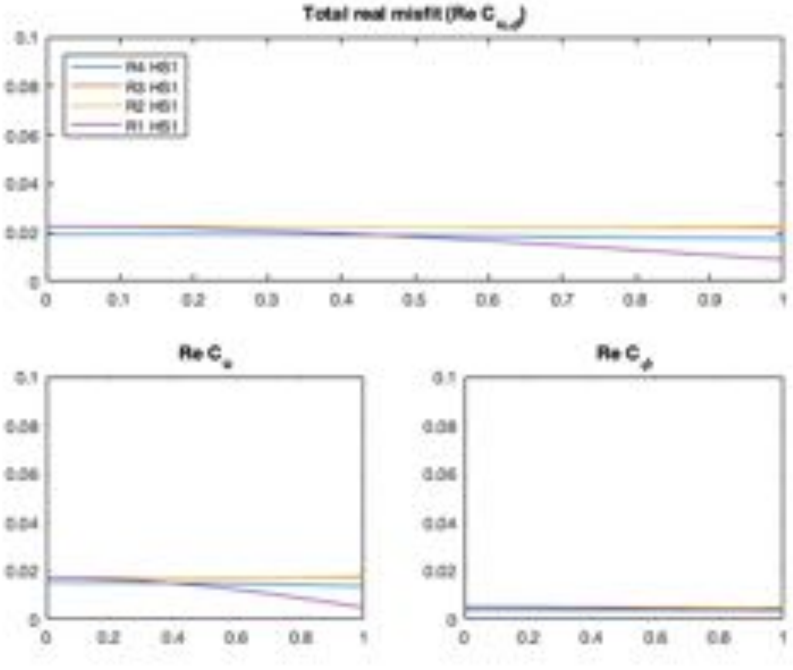

(a) Misfit real parts

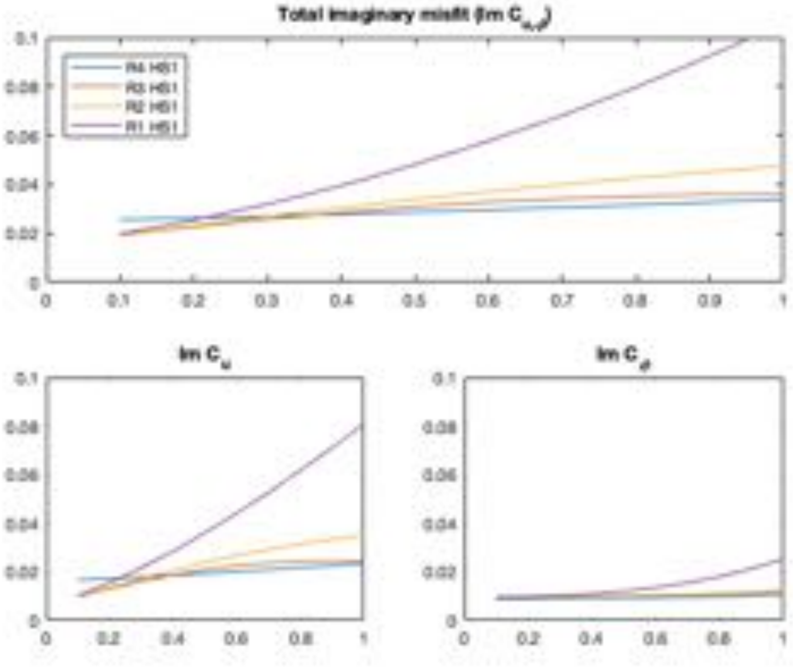

(b) Misfit imaginary parts

Figure C.1: Case HS1: Misfits between 3D and 1D for real & imaginary parts and contributions of displacements & rotations over frequency

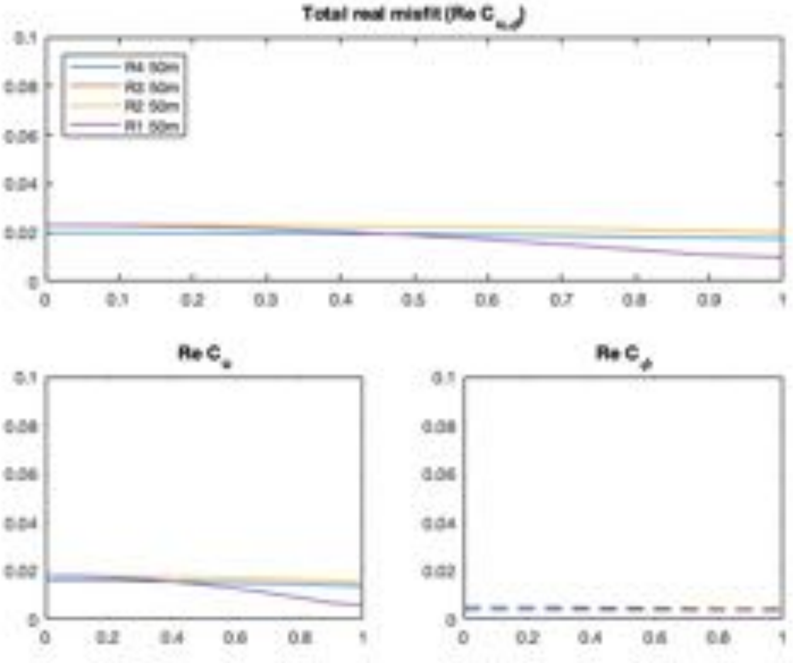

(a) Misfit real parts

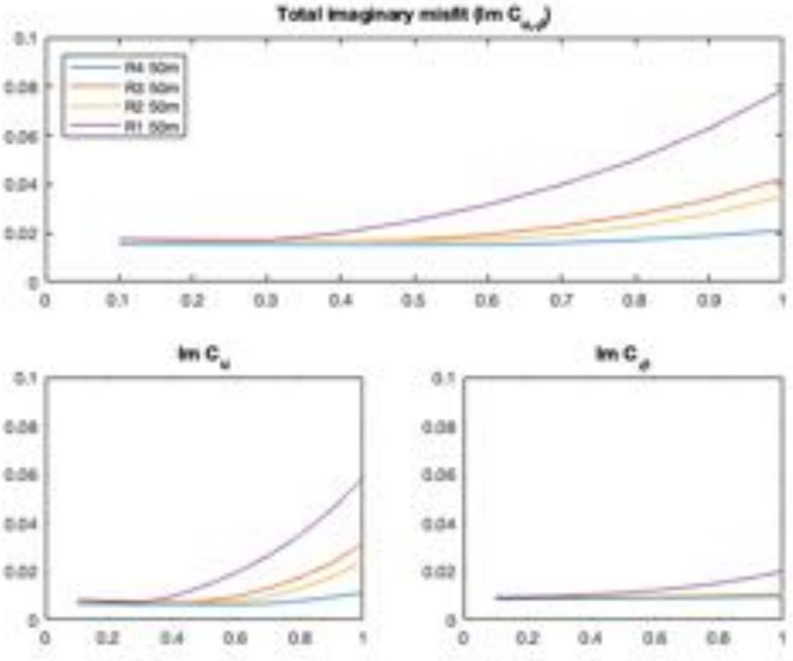

(b) Misfit imaginary parts

Figure C.2: Case HS2, bedrock at 50m: Misfits between 3D and 1D for real & imaginary parts and contributions of displacements & rotations over frequency

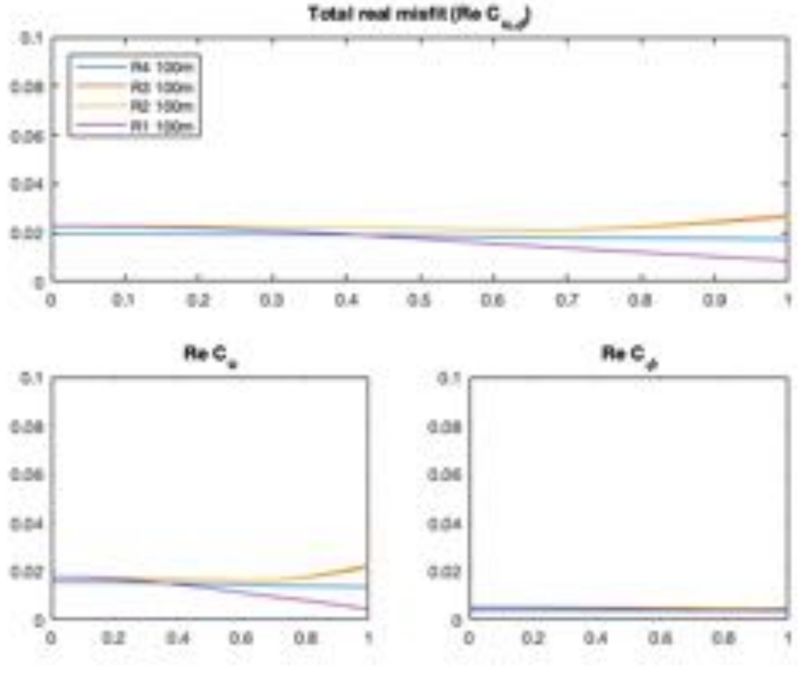

(a) Misfit real parts

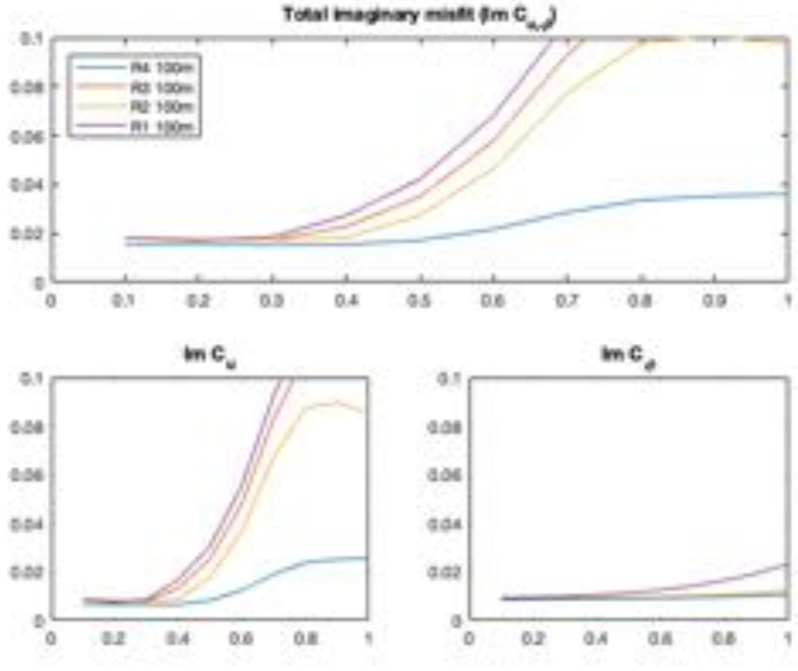

(b) Misfit imaginary parts

Figure C.3: Case HS2, bedrock at 100m: Misfits between 3D and 1D for real & imaginary parts and contributions of displacements & rotations over frequency

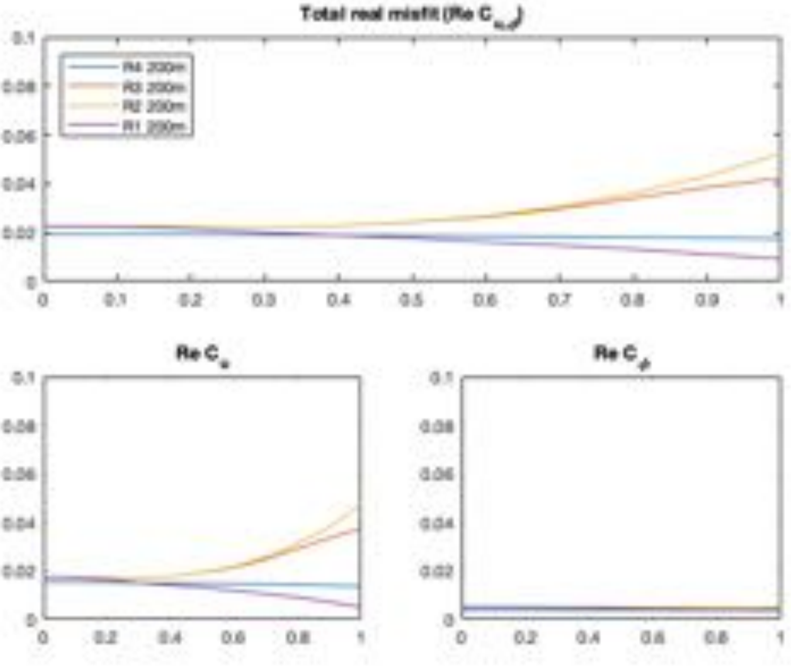

(a) Misfit real parts

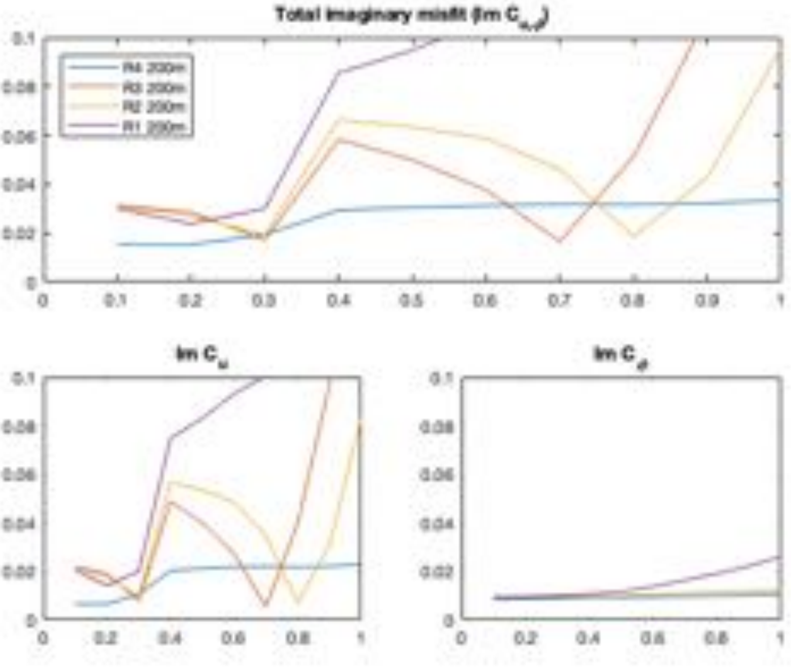

(b) Misfit imaginary parts

Figure C.4: Case HS2, bedrock at 200m: Misfits between 3D and 1D for real & imaginary parts and contributions of displacements & rotations over frequency

D

MATRICES

D.1. MATRICES SOIL-PILE SYSTEM

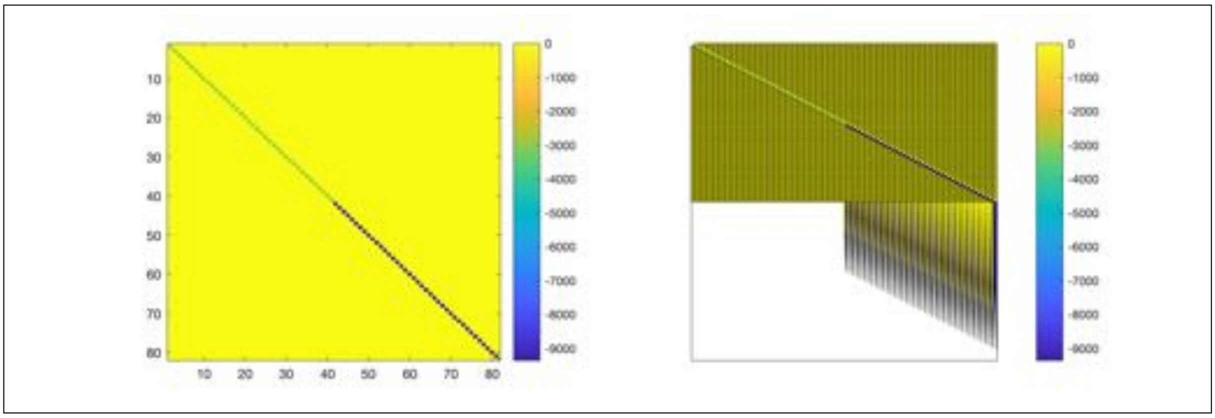

(a) Mass matrix of the pile (Mp), presented as an imagesc and surf plot.

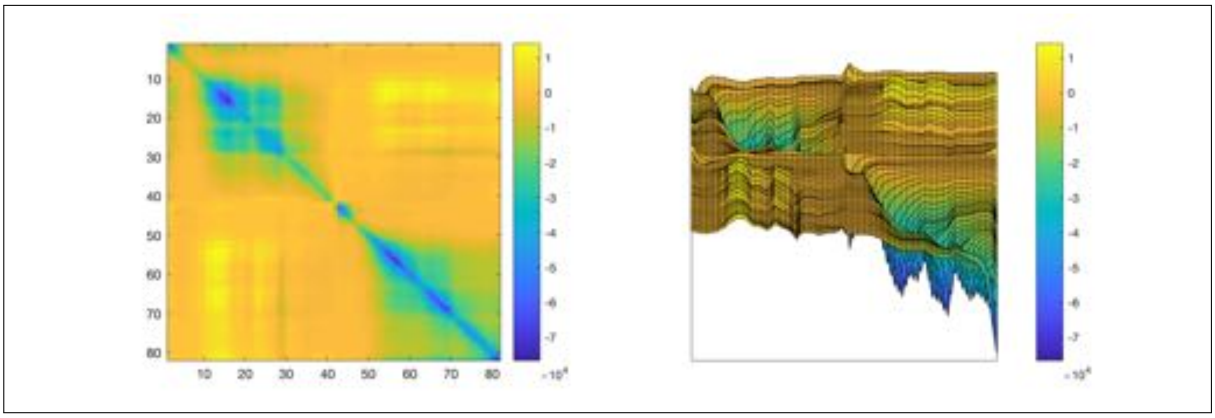

(b) Mass matrix of the soil (Ms), presented as an imagesc and surf plot.

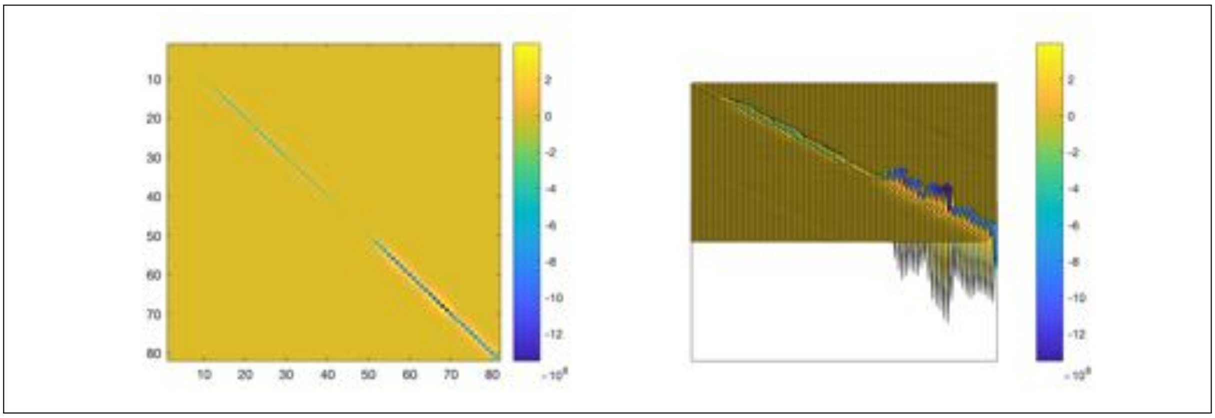

(a) Damping matrix (C), presented as an imagesc and surf plot.

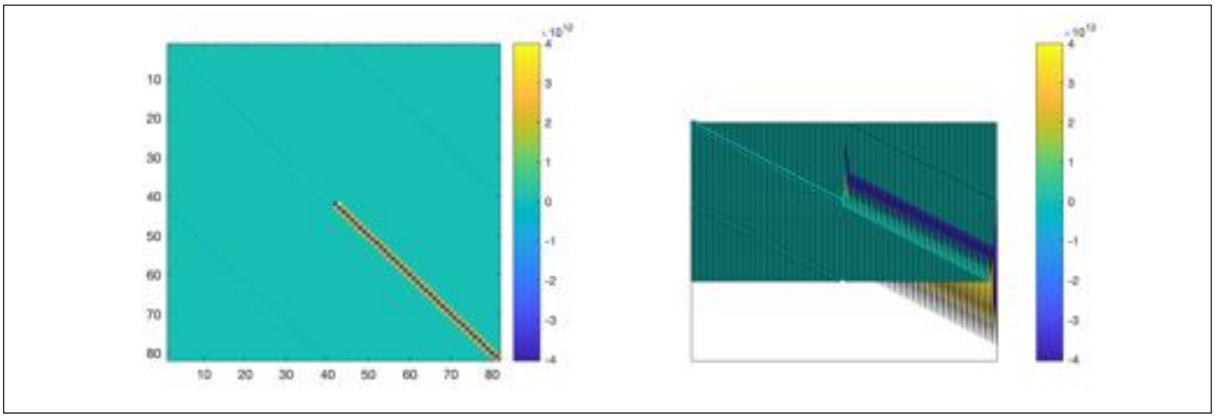

(a) Stiffness matrix of the pile (Kp), presented as an imagesc and surf plot.

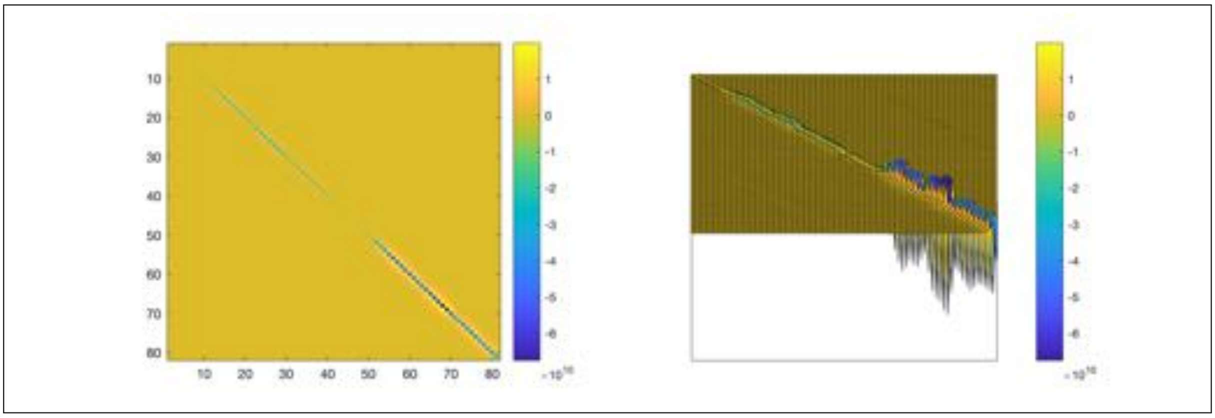

(b) Stiffness matrix of the soil (Ks), presented as an imagesc and surf plot.

E

CODE THRUST COEFFICIENT CALCULATION

```
function [Ct, a] = A4_calc_CthrustB0(Cp,tsr,Cp_opt,tsr_opt)

if tsr <= tsr_opt
    range=[0 1/3];
else
    range=[1/3 1];
end

a=fzero(@(w) 4*w*(1-w)^2-Cp*16/27/Cp_opt,range);

if a < 0.5
    Ct=4*a*(1-a);
else
    Ct=1.49/(1.99-a);
end

end
```

---

where: Cp_{opt} is the optimal power coefficient, tsr_{opt} the optimal tip speed ratio

BIBLIOGRAPHY

[1] Wind Europe, *Offshore wind in Europe; Key trends and statistics 2017*, Tech. Rep. (Wind Europe, Brussles, Belgium, 2018).

[2] Department of Trade and Industry, DTI, *Study of the costs of offshore wind generation. A report to the Renewables Advisory Board (RAB) & DTI.* (2007b).

[3] L. Arany, S. Bhattacharya, J. H G Macdonald, and S. Hogan, *Closed form solution of eigen frequency of monopile supported offshore wind turbines in deeper waters incorporating stiffness of substructure and ssi,* Soil Dynamics and Earthquake Engineering **83** (2016).

[4] J. H. Vugts, J. van der Tempel, and E. A. Schrama, *Hydrodynamic loading on monotower support structures for preliminary design,* Proc. Spec. Top. Conf. Offshore Wind Energy (2001).

[5] DNV, *DNV-OS-J101 Design of Offshore Wind Turbine Structures,* May , pp. 212 to 214 (2014).

[6] United Nations, *Framework convention on climate change - adoption of the paris agreement,* 21st Conference of the Parties (2015).

[7] W. G. Versteijlen, *Identification of effective 1D soil models for large-diameter offshore wind turbine foundations based on in-situ seismic measurements and 3D modelling,* Ph.D. thesis, TU Delft (2018).

[8] M. I. Blanco, *The economics of wind energy,* Eur. J. Oper. Res. **42**, 714 (2009).

[9] J. Jia, *Soil Dynamics and Foundation Modeling* (Springer Nature, Cham, Switzerland, 2018) p. 740.

[10] B. Byrne, R. McAdam, H. Burd, G. Houlsby, C. Martin, L. C, D. Taborda, D. Potts, R. Jardine, M. Sideri, F. Schroeder, K. Gavin, P. Doherty, D. Igoe, A. Wood, D. Kallehave, and J. Gretlund, *New design methods for large diameter piles under lateral loading for offshore wind applications,* Front. Offshore Geotech. III , 705 (2015).

[11] American Petroleum institute, *Recommended Practice for Planning, Designing and Constructing Fixed Offshore Platforms-Working Stress Design (RP2A-WSD)*, Tech. Rep. (API, 2000).

[12] S. Helwany, *Appl. Soil Mech. With ABAQUS Appl.* (Wiley, 2007) arXiv:arXiv:1011.1669v3 .

[13] S. Aasen, A. M. Page, K. Skjolden Skau, and T. A. Nygaard, *Effect of foundation modelling on the fatigue lifetime of a monopile-based offshore wind turbine,* Wind Energy Sci. **2**, 361 (2017).

[14] M. Novak and T. Nogami, *Soil-pile interaction in horizontal vibration,* Earthquake Engineering & Structural Dynamics **5**, 263 (1977).

[15] O. B. Leite, *REVIEW OF DESIGN PROCEDURES FOR MONOPILE OFFSHORE WIND STRUCTURES*, Ph.D. thesis, Universidade do Porto (2015).

[16] Y. He, B. W. Byrne, and H. Burd, *Application of a numerical-based design method for laterally loaded monopiles in layered soils,* 8th Int. SUT/OSIG Conf. Smarter Solut. Futur. Offshore Dev. (2017).

[17] L. Reese, W. Van Impe, and R. Holtz, *Appl. Mech. Rev.*, Vol. 55 (CRC Press, 2002) p. B9.

[18] H. R. Roesen, K. Thomassen, S. P. H. Sorensen, and L. B. Ibsen, *Evaluation of Small-Scale Laterally Loaded Non-Slender Monopiles in Sand,* DCE Tech. Reports No. 91 (2010).

[19] API - American Petroleum Institute, *Recommended Practice for Planning, Designing and Constructing Fixed Offshore Platforms - Working Stress Design,* (2003), arXiv:arXiv:1011.1669v3 .

[20] D. A. Bouzid, *Numerical Investigation of Large-Diameter Monopiles in Sands : Critical Review and Evaluation of Both API and Newly Proposed p-y Curves,* Int. Jounral Geomech. **18** (2018), 10.1061/(ASCE)GM.1943-5622.0001204.

[21] A. H. Augustesen, K. T. Brødbæk, M. Møller, S. P. H. Sørensen, L. Ibsen, T. S. Pedersen, and L. Andersen, *Numerical Modelling of Large-Diameter Steel Piles at Horns Rev,* Proc. 12th Int. Conf. Civil, Struct. Environ. Eng. Comput. , 1 (2009).

[22] S. M. Bayton and J. A. Black, *Evaluating the p-y Curve Method of Analysis for Large-Diameter Monopiles Using Centrifuge Modelling,* Geo-Chicago 2016 , 418 (2016).

[23] S. Malhotra, *Design and Construction Considerations for Offshore Wind Turbine Foundations,* in *Int. Conf. Offshore Mech. Arct. Eng.* (2007) arXiv:0803973233 .

[24] C. Hübler, J. Häfele, C. G. Gebhardt, and R. Rolfes, *Experimentally supported consideration of operating point dependent soil properties in coupled dynamics of offshore wind turbines,* Mar. Struct. **57**, 18 (2018).

[25] D. Kallehave, C. Thilsted, and M. Liingaard, *Modification of the API Py Formulation of Initial Stiffness of Sand,* in *Offshore Site Investig. Geotech. Integr. Technol. - Present Futur.* (2012).

[26] S. P. H. Sørensen, L. B. Ibsen, and A. H. Augustesen, *Effects of diameter on initial stiffness of p - y curves for large-diameter piles in sand,* Numer. Methods Geotech. Eng. , 907 (2010).

[27] S. Sørensen, *Soil-structure interaction for non- slender , large-diameter offshore,* Ph.D. thesis, Aalborg University (2012).

[28] J. M. d. O. Barbosa and E. Kausel, *PMLs: A direct approach Eduardo,* INTERNATIONAL JOURNAL FOR NUMERICAL METHODS IN ENGINEERING Int. **90:343–352**, 333 (2012), arXiv:1010.1724 .

[29] O. C. Zienkiewicz, R. L. Taylor, and D. Fox, *Finite Elem. Method Solid Struct. Mech. Seventh Ed.* (Butterworth-Heinemann, 2013) arXiv:arXiv:1011.1669v3 .

[30] N. Hamdan, *Two-Dimensional Numerical Modelling of Wave Propagation in Soil Media,* Ph.D. thesis, Heriot-Watt University (2013).

[31] M. Drozdz, *Efficient Finite Element Modelling of Ultrasound Waves in Elastic Media* (University of London, 2008).

[32] J. Berenger, *Evanescent waves in PML's: Origin of the numerical reflection in wave-structure interaction problems,* Antennas and Propagation, IEEE Transactions on **47**, pp. 1497 to 1503 (1999).

[33] J. De Moerloose and M. Stuchly, *Microwave and Guided Wave Letters,* Vol. 5 (IEEE, 1995) p. pp. 344 to 346.

[34] S. Jones, *Ground vibration from underground railways: how simplifying assumptions limit prediction accuracy,* Univ. Cambridge (2010), 10.5194/hess-15-2649-2011.

[35] G. Gazetas and R. Dobry, *Horizontal Response of Piles in Layered Soils,* J. Geotech. Eng. **110**, 20 (1984).

[36] T. Nogami and M. Novak, *Resistance of soil to a horizontally vibrating pile: Int J Earthq Engng Struct Dynam, V5, N3, July-Sept 1977, P249-261,* Int. J. Rock Mech. Min. Sci. Geomech. Abstr. TA - TT - **15**, A110 (1977).

[37] KEMA, *Offshore Windturbinepark Tromp Binnen Wbr-vergunningsaanvraag,* (2009).

[38] J. van Kan, A. Segal, and F. Vermolen, *Numerical Methods in Scientific Computing* (Delft Academic Press, 2014).

[39] J. Hoffman and S. Frankel, *Numerical Methods for Engineers and Scientists, Second Edition,* (Taylor & Francis, 2001).

[40] T. Irvine, *The Half Power Bandwidth Method for Damping Calculation, Vibration data,* (2005).

[41] J. JM, S. Butterfield, W. Musial, and G. Scott, *Definition of a 5mw reference wind turbine for offshore system development,* National Renewable Energy Laboratory (NREL) (2009), 10.2172/947422.

[42] T. I. Fossen and T. Perez, *Marine Systems Simulator (MSS),* (2004).

[43] USFOS, *Hydrodynamics, Theory Description of use Verification,* (2010).

[44] G. Keulegan and L. Carpenter, *Forces on cylinders and plates in an oscillating fluid,* J. Res. Natl. Bur. Stand. (1934). (1958), 10.6028/jres.060.043.

[45] J. Journee and W. Massie, *Offshore Hydromechanics,* TU Delft, course OE4630 (2015).

[46] J. G. Slootweg, S. W. H. De Haan, H. Polinder, and W. L. Kling, *General Model for Representing Variable-Speed Wind Turbines in Power System Dynamics Simulations,* IEEE Power Eng. Rev. **22**, 56 (2002).

[47] A. Rauh and W. Seelert, *The Betz optimum efficiency for windmills,* Appl. Energy (1984), 10.1016/0306-2619(84)90037-0.

[48] C. keijdener and A. Arquin Laguna, *Introduction to Computational Dynamic of Offshore Structures,* TU Delft, course OE44090 (2015).

[49] D. Akin, *Response of an off shore wind turbine to simultaneous wind and wave loads*, Msc thesis, Danmarks Tekniske Universitet (2011).

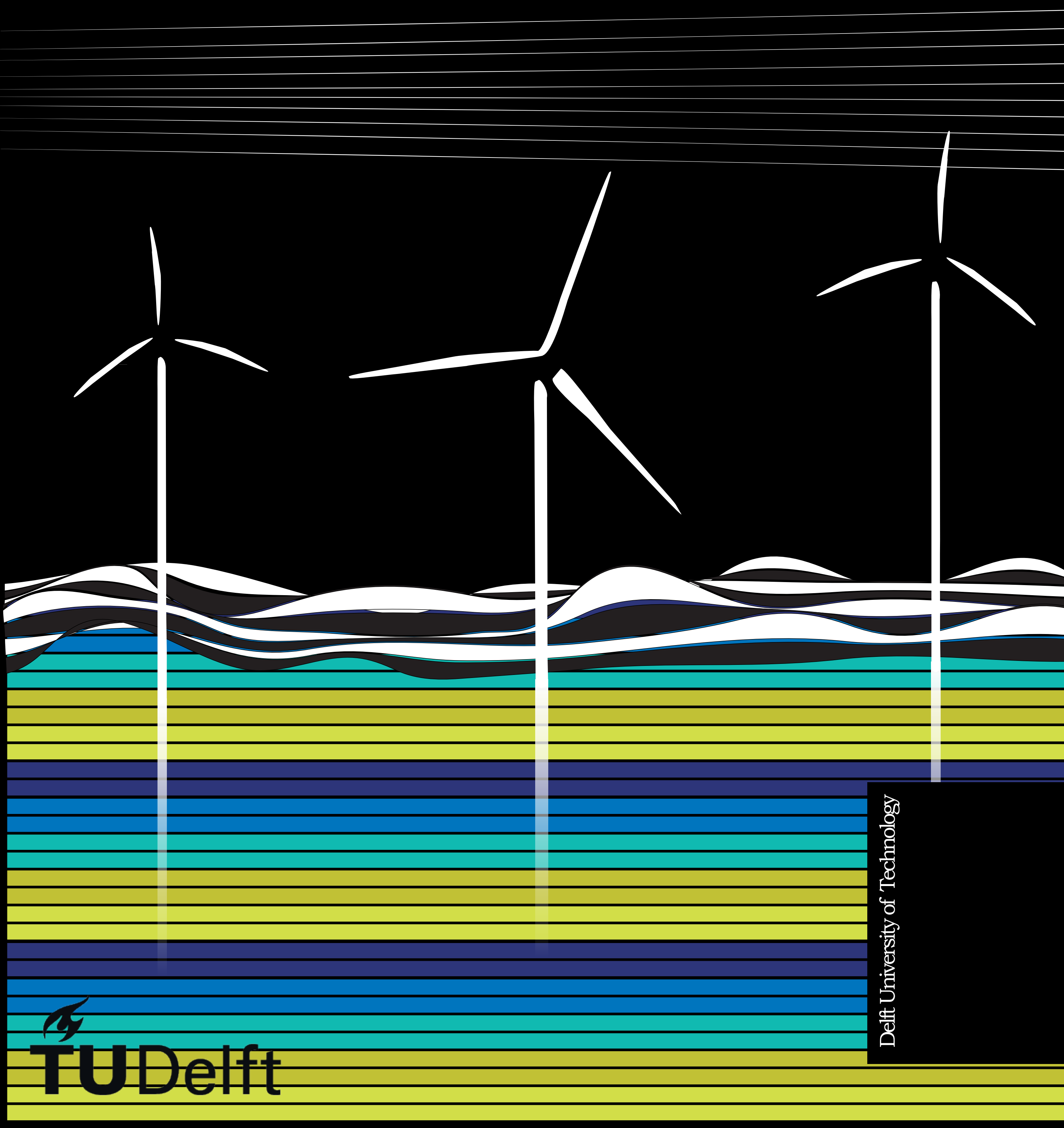

TU Delft

Delft University of Technology